Effect of process, design parameters and post-processing on the Laser powder bed fusion 17-4 PH Stainless Steel

Submitted in partial fulfilment of the requirements

for the award of the degree of

Doctor of Philosophy

by

Ippili Kartikeya sarma

Roll No: 719046

Under the Supervision of

Prof. N. Selvaraj

Professor, MED

&

Prof. Adepu Kumar

Professor, MED

DEPARTMENT OF MECHANICAL ENGINEERING

NATIONAL INSTITUTE OF TECHNOLOGY WARANGAL

WARANGAL– 506 004, TELANGANA, INDIA

January - 2023

THESIS APPROVAL FOR Ph.D.

This thesis entitled **"Effect of process, design parameters and post-processing on Laser powder bed fusion 17-4 PH Stainless Steel"** by **Mr. Ippili Kartikeya sarma** is approved for the degree of Doctor of Philosophy.

_____

_____

_____

Examiner

Prof.N. Selvaraj
Professor, Department of Mechanical Engineering, NIT Warangal
Supervisor

Prof. Adepu Kumar
Professor, Department of Mechanical Engineering, NIT Warangal
Supervisor

Prof. V. Suresh Babu
Head, Department of Mechanical Engineering, NIT Warangal
Chairman

CERTIFICATE

This is to certify the thesis entitled **"Effect of process, design parameters and post-processing on Laser powder bed fusion 17-4 PH Stainless Steel"** submitted by **by Mr. Ippili Kartikeya sarma,** Roll No. 719046, to **National Institute of Technology, Warangal** in partial fulfilment of the requirements for the award of the degree of **Doctor of Philosophy in Mechanical Engineering** is a record of bonafide research work carried out by him under our supervision and guidance. This work has not been submitted elsewhere for the award of any degree.

Place: Warangal.
Date: 09-01-2023.

Prof.N.Selvaraj
Supervisor
Professor,
Department of Mechanical Engineering,
National Institute of Technology,
Warangal, Telangana State.

Prof. Adepu Kumar
Supervisor
Professor,
Department of Mechanical Engineering,
NIT Warangal

NATIONAL INSTITUTE OF TECHNOLOGY

WARANGAL – 506 004, Telangana State, INDIA

DECLARATION

This is to certify that the work presented in the thesis entitled **"Effect of process, design parameters and post-processing on Laser powder bed fusion 17-4 PH Stainless Steel"**, is a bonafide work done by me under the supervision of **Prof.N.Selvaraj**, Professor, Department of Mechanical Engineering, NIT Warangal, India and **Prof.Adepu Kumar**, Professor, Department of Mechanical Engineering, NIT Warangal, India and has not been submitted for the award of any degree to any other University or Institute.

I declare that this written submission represents my ideas in my own words and where ever others ideas or words are included have been adequately cited and referenced with the original sources. I also declare that I have adhered to all principles of academic honesty and integrity and have not misrepresented or fabricated or falsified any idea/data/fact/source in my submission. I understand that any violation of the above will cause for disciplinary action by the institute and can also evoke penal action from the sources which have thus not been properly cited or from whom proper permission has not been taken when needed.

Place: Warangal.
Date: 09-01-2023

Ippili Kartikeya sarma
Roll No. 719046

ACKNOWLEDGEMENTS

I would like to express my sincere gratitude and profound indebtedness to **Prof.N.Selvaraj**, Professor of Mechanical Engineering Department, National Institute of Technology, Warangal and **Prof. Adepu Kumar,** Professor of Mechanical Engineering Department, National Institute of Technology, Warangal for giving me an opportunity to carry out doctoral work under their esteemed supervision. This work is a reflection of their thoughts, ideas and concepts. **Prof.N.Selvaraj and Prof. Adepu Kumar** looks at things in the right perspective, and it has truly been a learning experience working with him. I owe a lot to him for making me a part of the continuity of the profession.

I extend my sincere gratitude to **Prof. N. V. Ramana Rao,** Director, National Institute of Technology Warangal, India for providing the necessary facilities and encouragement throughout my work.

I am thankful to **Prof. Suresh babu**, Head, Department of Mechanical Engineering, NIT Warangal and other faculty members for their encouragement and support extended during this period.

It's my great opportunity to express my deepest gratitude to the Departmental Scrutiny Committee members, **Dr. K.V.Sai Srinadh**, Professor, Department of Mechanical Engineering, and **Dr. Y. Ravi Kumar,** Professor, Department of Metallurgical and Materials Engineering, and **Dr Kishore Babu,** Associate Professor, Department of Mechanical Engineering, for their adeptness and many discussions during this research period.

I am grateful to **Dr. N. Shivraman,** Assistant Professor of Mechanical Engineering Department, National Institute of Technology, Warangal, for his constant support and motivation to carry out my experimentation and research work.

I am thankful to **Dr. Raj Mohan K S**, Assistant Professor of Chemical Engineering Department, National Institute of Technology, Warangal, for providing corrosion testing facility.

I express my sincere thanks to my co-scholars **Kranthi, Satya, Nagu, Sundar, MCT Lab,** NIT Warangal for their support during the entire period.

I am thankful to my co-scholars **Rakesh, Srikanth, AM Lab, NIT** Warangal, for their support in sample deposition.

I would like to extend my heartfelt thanks to **Mr. B. Rangilal, Mr. G. Ilaiah** and **K. Raju** technical staff of Production Engineering Lab and **Mr. M. V. Vijay Kumar** Office staff of Mechanical Engineering Department, NIT Warangal for their constant help and encouragement.

I am thankful to **Mahesh Kumar Talari**, Head, Department of **Metallurgical and Materials Engineering**, NIT Warangal and other faculty members for their support for material characterization during this period.

I am thankful to **Dr. M. Raja Vishwanathan**, Associate professor, Department of Humanities & Social Science for proofreading the manuscript and thesis.

A special debt of deep gratitude to my wife, family members for their unceasing sacrifices, endeavors and encouragement.

Finally, I would also like to acknowledge the help given by all the persons who have directly or indirectly supported the work.

Ippili Kartikeya Sarma

Research Publications

List of publications

Publications (Accepted/published online)

1. **I.Kartikeya Sarma**, N.Selvaraj, Adepu Kumar, Parametric investigation and characterization of 17-4 PH stainless steel parts fabricated by selective laser melting, **Journal of central south university, Springer** (accepted on June 13th 2022) **.(SCI)** (**IF-2.392**)

2. **I.Kartikeya Sarma**, N.Selvaraj, Adepu Kumar, Influence of Scanning Strategies on the microstructure, mechanical properties and Corrosion Properties of the 17-4 PH Stainless Steel fabricated by Selective Laser Melting, **Proc IMechE Part E: J Process Mechanical Engineering** 2022,Doi:10.1177/09544089221106263**.(SCI)** (**IF-1.822**)

3. **I.Kartikeya Sarma**, N.Selvaraj, Adepu Kumar, Influence of hexagonal scanning strategy island size on microstructure, residual stress and corrosion behavior of 17-4 PH SS made by L-PBF" **Journal of Materials: Design and Applications,2022 .(SCI) (IF-2.663**)

4. **I.Kartikeya Sarma**, Selvaraj.N, Adepu Kumar, Influence of design and process parameters on residual stress and microstructural evolution of 17-4 PH SS made by L-PBF, **Journal of Materials: Design and Applications,2022 .(SCI) (IF-2.663**)(minor revision)

5. **I.Kartikeya Sarma**, N.Selvaraj, Adepu Kumar,A Review on L-PBF 17-4PH and 15-5PH SS: Microstructure and Properties, Lecture Notes in Mechanical Engineering, Springer, ICRAM, SVNIT, June 10-12 2021, **(scopus)**

Publications (communicated)

1. **Kartikeya Sarma.I**, Selvaraj.N, Adepu Kumar, V Uday kumar, Impact of heat treatment on the damping behavior of L-PBF 17-4 PH SS, (submitted to manufacturing letters)

2. **Kartikeya Sarma.I**, Selvaraj.N, Adepu Kumar, Impact of heat treatment on the fatigue behavior of L-PBF 17-4 PH SS, (submitted to materials letters)

3. **Kartikeya Sarma.I**, Selvaraj.N, Adepu Kumar, Effect of scan strategies and process parameters on the abrasive wear behavior of 17-4PH SS by selective laser melting, (submitted to welding in the world)

4. **Kartikeya Sarma.I**, Selvaraj.N, Adepu Kumar, Scan Strategies Influence on the Corrosion and Abrasive Wear behavior of SLM 17-4 PH Stainless Steel, (submitted to friction and wear)

Conference papers

1. **Kartikeya Sarma.I**, Selvaraj.N, Adepu Kumar, Effect of process parameters on the L-PBF 17-4 PH Stainless steel microstructure and corrosion behavior, (SICE-2022) December-14-16,2022

2. **Kartikeya Sarma.I**, Selvaraj.N, Adepu Kumar, Effect of process parameters on the L-PBF 17-4 PH Stainless steel microstructure and corrosion behavior, IEI-Thirty Seventh National Convention of Mechanical Engineers, 9^{th} and 10^{th} December, 2022

ABSTRACT

The present study performed parametric investigation and characterizations on 17-4 precipitation hardened stainless steel built by selective laser melting. Cubical samples were deposited by considering process parameters (laser power and scan speed) and scan strategy (design parameter) to investigate relative density and microhardness. Micro hardness were maximum for samples with medium energy density and when hexagonal inside out scan strategy was used. It was minimum for the sample with low energy density and when strip alternate scan strategy was used. Austenite, ferrite, and small molten pools were observed on the side surface of samples from optical and scanning electron microstructure analysis. Higher corrosion resistance (<0.5 mpy) and absence of corrosion cracks were present for all samples with different energy densities.

Morever, the effect of different scan strategies like hexagonal (inside out and outside in), rectangular (horizontal, vertical, alternate and both), strip(horizontal, vertical, alternate, and both) on the microstructure, residual stresses, and corrosion behavior of the 17-4 PH SS samples fabricated by selective laser melting was investigated. The results indicate that SLM samples irrespective of different scan strategies exhibited higher density and hardness than wrought alloy. The hexagonal inside out, rectangular alternate and strip alternate yielded better hardness out of scanning strategies. Small molten pools were observed on the side surface while large molten pools were seen on the front surface of each sample generated using a different scan strategy. The residual stresses were minimum for hexagonal inside-out scan strategy compared to strip alternate and rectangular scan strategies because of lower thermal gradient and small scan tracks. Higher corrosion resistance (<0.5 mpy) was obtained for the hexagonal inside-out scan strategy sample compared to other two because of lower defects.

Subsequently, the effect of hexagonal scan strategy island size on microstructure, micro hardness, residual stresses and corrosion behavior of 17-4 PH SS fabricated by laser-powder bed fusion with a scan rotation angle of 90 degrees was investigated. The results indicate the average time per layer decreases as the island size increases. The hardness varied with island size and higher hardness was exhibited due to fine grain size. The medium islands size microstructure consists of regular molten pools and lower heat accumulation. Small molten pools were observed on the side surface respecctively for samples with different hexagonal island sizes. The austenite phase was detected in all samples with the highest intensity at hexagonal inside out sample with island size of 2.5mm at 43.500 degrees. Both hexagonal

samples with 2.5 mm island size and 10 mm samples almost exhibit ɣ -austenite phase in the finer grain size area, as per EBSD orientation maps. The residual stresses increased as the hexagonal island size increased because when a large island size is used, it produces a long scanning track with a weak pre-heating effect, resulting in a high-temperature gradient and high residual stress. Higher corrosion resistance was obtained for 2.5mm hexagonal scan strategy island size because of finer grain size and lower defects.

Further investigations were made on the damping characteristics heat treated 17-4 PH SS. As built samples were made by laser powder bed fusion and different heat treatments were done to understand the microstructure, hardness, frequency-dependent, and temperature-dependent damping characteristics. The results shown that solution annealing heat treated samples saw an increase in dislocation density, finer grain size, and an increase in grain boundary area, which significantly increased damping capacity for solution annealing sample in both frequency-dependent and temperature-dependent damping characteristics and reduction in micro strain. The fatigue crack growth rate is inhibited after solution annealing heat treatment.

Keywords: Additive Manufacturing, Laser Powder Bed Fusion, 17-4 PH SS, Heat-treatment, Scan Strategy, Characterization

CONTENTS

LIST OF TABLES

LIST OF FIGURES

ABBREVIATIONS

DED	Directed energy deposition
BJ	Binder jetting

SLS	Selective laser sintering
LOM	Laminated object manufacturing
AM	Additive manufacturing
LAM	Laser assisted additive manufacturing
MAM	Metal additive manufacturing
XRD	X-ray diffraction
FWHM	Full width at half maximum
PBF	Powder bed fusion
P-DED	Powder based direct energy deposition
W-DED	Wire based direct energy deposition
17-4 PH SS	17-4 Precipitation hardened stainless steel
SLM	Selective laser melting
AM	Additive Manufacturing
FGM	Functionally graded materials
FCG	Fatigue crack growth
CNC	computer numerical controller
HCF	High cycle fatigue
CT	Compact Tension
MOD H900	Modified H900
OCP	Open Circuit Potential
EBSD	Electron Back Scattered Diffraction
EIS	Electro chemical impedance spectroscopy

NOMENCLATURE

P	Laser power

v	Scanning speed
E	Energy density
λ	Wave length of X-ray
HD	Hatch Disatnce
LT	Layer Thickness
ρ	Density
α	Solid and liquid interface angle
β	Full width half maximum
T	Temperature
C_p	Specific heat capacity
d	Crystallite size
ε	Micro strain
T_0	Room temperature
h	Heat transfer coefficient
C	Scherrer constant
θ	Peak position in radians
E_{corr}	Corrosion potential
I_{corr}	Corrosion current density

CHAPTER I

INTRODUCTION

1.1. Introduction

In contrast to subtractive additive manufacturing, additive manufacturing (AM) involves creating the component layer by layer using data from a three-dimensional model. It is also known as direct digital manufacturing, rapid prototyping, and solid freeform fabrication [1]. Fig. 1.1 depicts the usual AM process cycle.

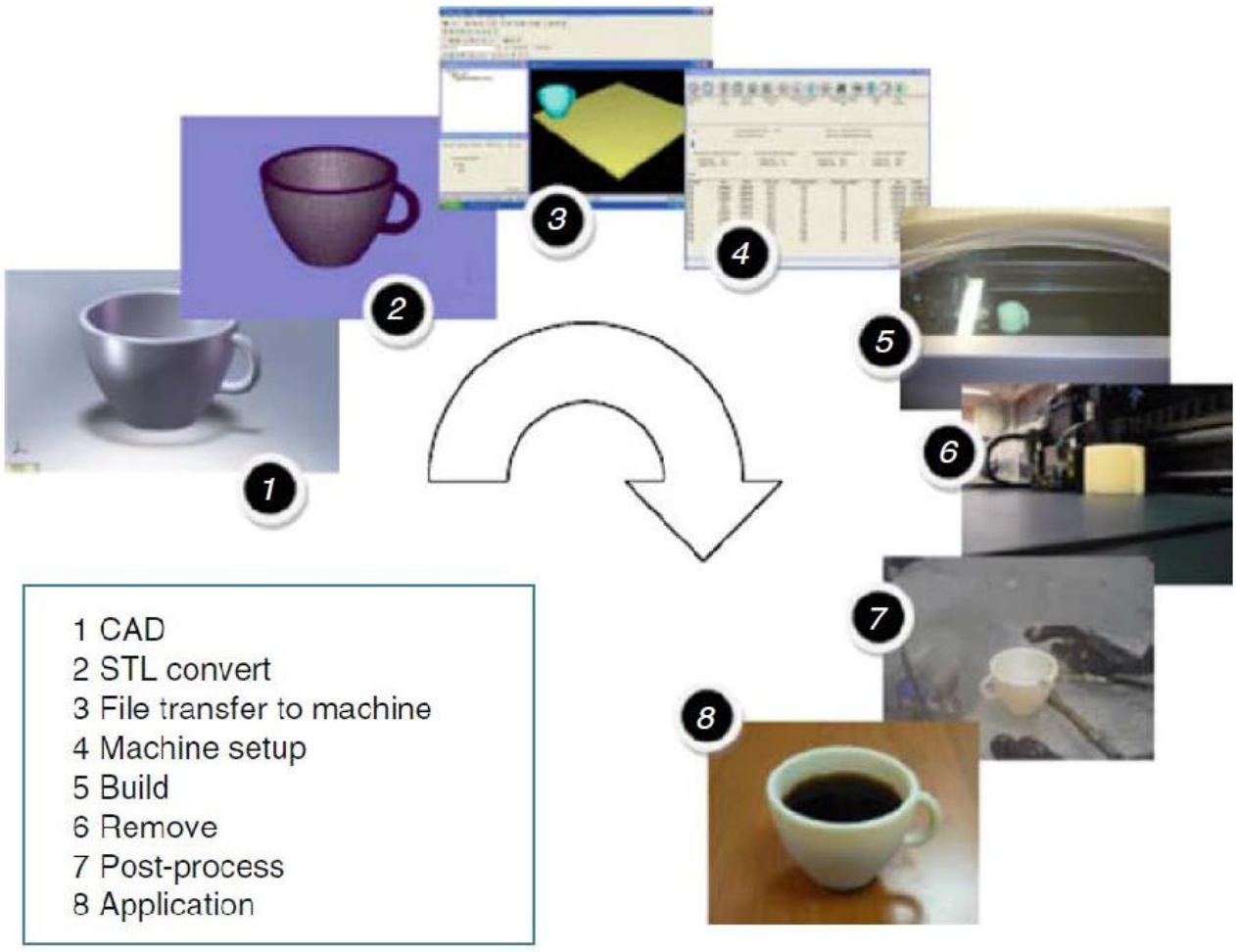

Fig. 1.1. AM process cycle [1]

Without the use of specific fixtures, it is possible to create complex geometries, and it also lowers the quantity of spare parts needed for final assembly. The AM process may produce functional prototypes and parts for commercial products and services.[2] It eliminates the need for

expensive instruments like punches, dies, cutting tools, and casting moulds and can make complex and personalized parts (such as cooling channels and lattice structures) even while lowering the number of stages required in the conventional method. It can also produce parts on demand, which reduces lead times and inventories [3]. For high volume manufacturing, AM cannot, however, take the place of conventional process, and its applicability is further constrained by residual stresses and the component's inherent anisotropy. The AM process makes it simple to construct a component with straight cuts and a circular hole. A minimum of spare parts are needed for assembly for the AM method' ability to directly generate functioning parts, which also cuts down on lead times, production costs, and material waste. Materials used in AM technologies typically include metals, ceramics, polymers, and composites [4]. As a result, AM technologies are used in a variety of industries, including medical, aerospace, marine, automotive, and energy sectors. Although AM cannot totally replace conventional processes, it is one of the toolkits that allows engineers to have more design freedom. Large manufacturing runs are not appropriate, and it can only be used for small to medium complex items. AM reduces the transit cost, time, supply chain, and energy costs [5]. AM technologies are primarily divided into seven types, according to the American Society for Testing of Materials (ASTM), including powder bed fusion (PBF), direct energy deposition (DED), vat-photo polymerization, material jetting (MJ), binder jetting (BJ), material extrusion, and sheet lamination [6]. In the AM process, materials such as polyamide, acrylonitrile-butadiene-styrene (ABS), photo-curable resin, polycarbonate, wax, metal, ceramic, and polymer powders, as well as adhesive-coated sheets, are used.

1.2. Metal additive manufacturing

Revenue from metal printed parts increased by 41.9%, continuing a five-year record of yearly AM growth rates exceeding 40%. In comparison to the conventional method, the parts produced by MAM process have a fine microstructure and a better yield strength. The MAM components are therefore of particular importance to aerospace and automotive industries. Because of this, it is essential to comprehend how material properties, microstructure, and processing methods behave in order to produce high-quality, dependable, and qualified parts for engineering applications[7]

Sheet lamination (SL), binder jetting (BJ), powder bed fusion (PBF), and directed energy deposition (DED) are the four main AM methods for metal processing. Fig. 1.2 displays the MAM process classification. According to the type of melting (partial/full melting) and the heat source

(laser/electron beam), powder bed fusion is further divided into different categories. By utilizing a binder or ultrasonic vibrations to mix metal particles or metal foils, the metal pieces can be created indirectly. After post-processing, the final component with full density is produced. Selective laser sintering (SLS), laminated objective manufacture (LOM), and binder jetting are examples of indirect techniques (BJ). In the SLS process, metal pieces are created by partially melting powder particles or using a binder with a low melting point to keep powder particles together. For full density components, the final item must undergo post-treatment (curing, heat sintering, and infiltration). The LOM technique involves layer-by-layer ultrasonic vibration to combine the sheet foils, and laser cutting to get the necessary geometry. A laser or electron beam sinters the powder layer by layer in line with sliced data, and complete melting is used to accomplish powder particle bonding in SLM/EBM process.[8]

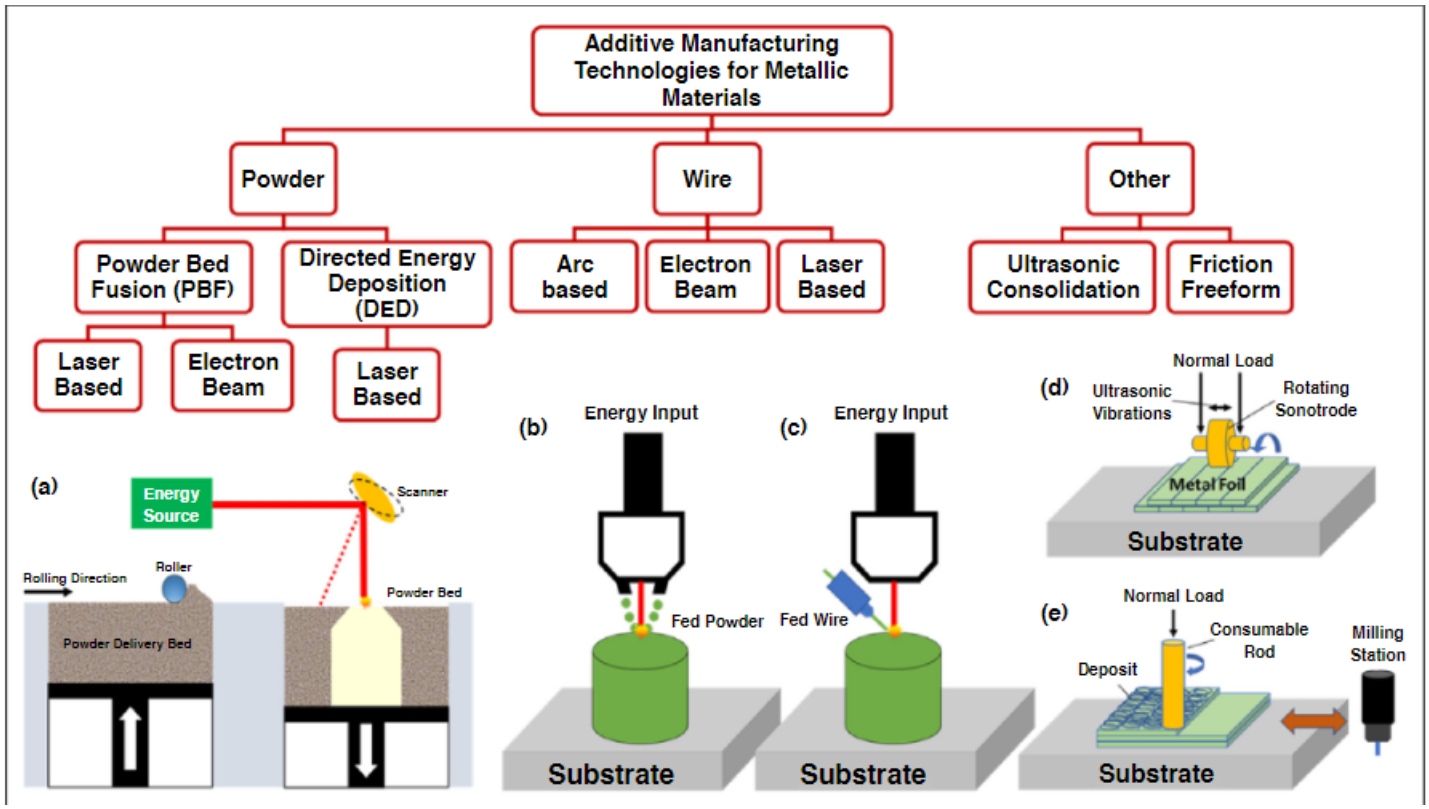

Fig. 1.2 Classification of Metal AM [9]

Material can be fed into Metal AM in the form of wire or powder, but powder is the primary raw material used in most industrial processes. PBF and DED are two examples of metal AM techniques. In the DED process, a laser melts the metal powder or wire that is fed into it and deposits it on the substrate or build plate. With AM direct procedures like SLM, EBM, and DED,

full density components may be produced, and these components' mechanical qualities are on par with those of metals produced using more traditional techniques. By using direct energy deposition and powder bed fusion, the full density parts are directly produced.

Depending on the procedure used for AM, the raw material is utilised in various ways. For instance, wire, sheet, and powder (powder bed fusion, DED) (LOM). Different alloys, such as iron alloys, aluminium alloys, titanium alloys, nickel alloys, and cobalt alloys, are effectively processed by AM technologies like SLS, SLM, EBM, and DED. Table 1.1 provides a summary of some of them.

Table 1.1: Materials processed in additive manufacturing

Alloy	**Grade type**
Stainless steel alloys (SS)	SS 304, 304 L, 316 and 316 L
Precipitation hardening (PH) stainless steel	15-5 PH, 17-4 PH
Nickel base alloys	Invar 36, Inconel 625 and Haynes 230, Inconel 718
Titanium alloys	Ti6Al4V
Aluminum alloys	AlSi10Mg, AlSi10,AlSi7Mg
Cobalt alloys	Co-Cr

Alumina, zirconia, and silica are ceramic materials utilized in the AM process. Due to its outstanding qualities, such as chemical resistance and high-temperature resistance, ceramics are employed in a wide variety of applications. Due to their hardness, complicated ceramic pieces are challenging to produce using traditional techniques. Two or more constituent materials with distinctly different physical or chemical characteristics are combined to form composites. By incorporating fibre and ceramic particles, AM technique can be utilised to create composites made of polymer, ceramic, and metal. AM has successfully produced metal-based composites such as Ti-TiC, Ti-TiN, and IN 625-TiC [10]. Functionally graded materials (FGM), which cannot be deposited using traditional techniques, are successfully deposited using the DED process, making FGM one of the key benefits of AM technology. For the fabrication of FGM parts, the DED method is generally chosen. Examples include SS304 L+ IN 625, SS 316L+ IN 625, Ti-6Al-4V+

AlSi10Mg, etc. [11].The major MAM processes used for different applications are summarized below.

1.2.1 Binder jetting process

Binder jetting (BJ) was established by Massachusetts Institute of Technology (MIT) in 1993, and Z Corporation obtained a licence from MIT for the procedure two years later. Polymers are initially chosen for the BJ process, followed by ceramics. However, starting in the early 2000s, BJ method was used for metals[7]. While the BJ process uses a similar operating concept to PBF, binder droplets (80 m) are used in place of the laser. Fig. 1.3 displays BJ process's schematic diagram.

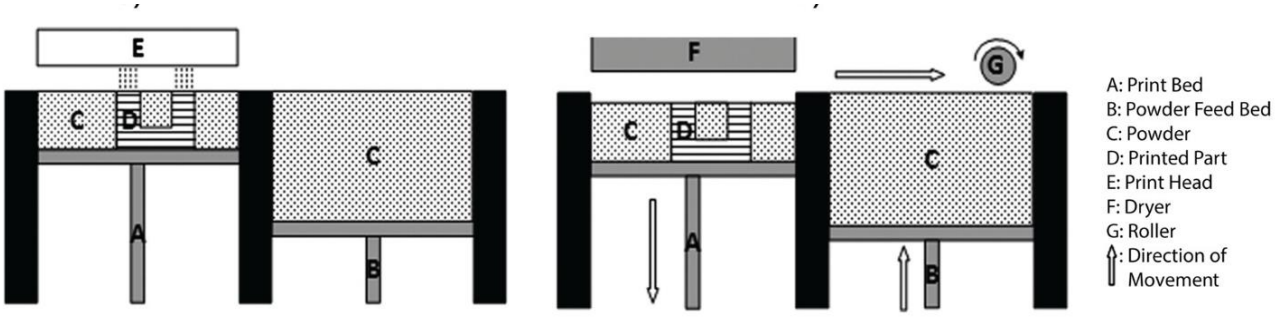

Fig. 1.3. Binder jetting process and its working principle[12]

According to the design data, binder droplets from inkjet nozzles are deposited over the powder and function as a binding substance between powder particles, depositing one layer over the bed. The powder bed is reduced by one layer thickness before the second layer is deposited. The process keeps on in this way to create the ultimate green component. It works best with materials like composites, metals, and plastics. Various post-processing methods, including curing, de-powdering, sintering, infiltration, annealing, and finishing, are applied to the finished green part. When bronze is utilised as an infiltrate, the density of stainless steel increases from 60 to 95%; similarly, cobalt and aluminium are used as infiltrates for tungsten carbide and boron carbide, respectively [12]. In comparison to the PBF technique, the BJ approach can create hollow cooling channels on a greater scale and offers high feature resolution. Design freedom is possible that isn't achievable with more traditional processes like forging, casting, and machining. Large build volumes, fast print speeds, many materials per build, self-supporting, and lack of support structures like powder bed fusion are benefits of the BJ method.

1.2.2 Laminated object manufacturing (LOM) process

Raw material utilised in the LOM process in the shape of a sheet. When the sheet is spread over the substrate for the first layer, the laser cuts the sheet according to the desired contour using three-dimensional data. Moving a hot roller to compress the layer and activate heat-sensitive adhesive paper creates a strong bond between two subsequent layers. Fig. 1.4 displays the LOM process's schematic diagram. Based on the bonding method used between the sheet layers, the LOM process is divided into adhesive or glueing, clamping, thermal bonding, and ultrasonic welding categories. When compared to other AM techniques, the LOM process produces parts with less complexity while eliminating the defects related to distortion, phase transition, and solidification [13]. Depending on the procedure used, glueing and bonding can be carried out in one of two ways: either a) bond-then-form (first bond the sheet to the substrate, then form the necessary cross-section), or b) form-then-bond (First cut the sheet in the required cross-section and sticks to the substrate).

Instead of using thermal and adhesive bonding, the clamping method is used to create metal laminates. For successful sheet lamination of useful tooling and metal components, thermal bonding is one of the techniques used.

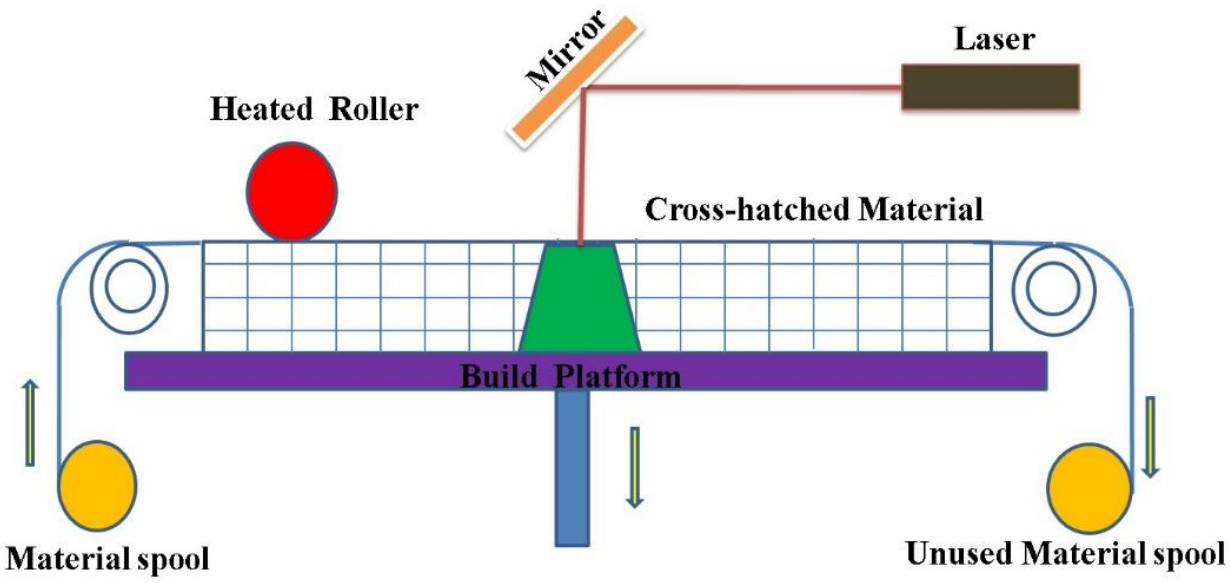

Fig. 1.4 Schematic of laminated object manufacturing process [14]

Sheet foil is positioned over the base plate or previously deposited layer in the ultrasonic additive manufacturing (UAM) procedure. With a frequency of 20 kHz, the sonotrode then oscillates and moves alongside the sheet joint. The oscillations of the sonotrode are consistent with the motion.

Here, computer numerical controller (CNC) milling is used to produce each layer's necessary shape. Each sheet of foil is subjected to this hybrid process until the last step of fabrication. Copper, aluminium, and titanium sheet foils can all be successfully used with it. In the UAM process, the following process variables are used: oscillation amplitude, normal force, sonotrade travel speed, preheat temperature, and foil thickness. Utilizing the UAM technique, aluminium alloy (6061) is successfully manufactured.

1.2.3 Selective laser sintering (SLS) process

It consists of an atmosphere control system, a CO2 laser, a scanner system, a roller mechanism, a part-process chamber, and a controller unit. The chamber is first preheated to a temperature below the melting point of the powder material, and then a layer is deposited using a roller at the desired thickness before being laser-scanned as intended. In the SLS process, binders with low melting points are partially melted or melted to create portions that help metal powder particles adhere to one another. Low melting point metal and polymers are the most typical binders utilised in the SLS process (phenolic polymer).

It can build components using different materials such as polymers (polyvinyl chloride (PVC), Polyethylene (PE), Polypropylene (PP), Polymethyl methacrylate (PMMA), Polystyrene (PS), Polyethylene terephthalate (PET), Polyamide (PA) and Plycarbonate (PC)), metals (cobalt-based, nickel-based, bronze-nickel, pre-alloyed bronze-nickel, 28 Inconel 625, Ti- 6Al-4V, stainless steel, gas-atomized stainless steel 316L, AISI 1018 carbon steel, high-speed steel precoated), ceramics (Al_2O_3, FeO, NiO, ZrO_2 , SiO_2 and CuO), cermets and composite materials, bio-material metals–polymers and metals–ceramics combinations. The post-processing, which includes binder removal, heat sintering, and liquid metal infiltration, is typically necessary to produce components with full densities (if required). The classification of SLS process parameters based on the various modes is shown in Fig. 1.5. The final qualities of the component are greatly influenced by SLS process parameters such as scanning speed, layer thickness, laser power, laser beam density, hatch spacing, and scanning pattern. The surface smoothness, build rate, and mechanical qualities of the finished item are thus greatly influenced by choosing the best possible combination of process parameters. The components created by SLS are employed in engineering and medical applications such as tissue engineering, aerospace, automotive, wind tunnel, investment casting, tooling, and metallic injection moulds.

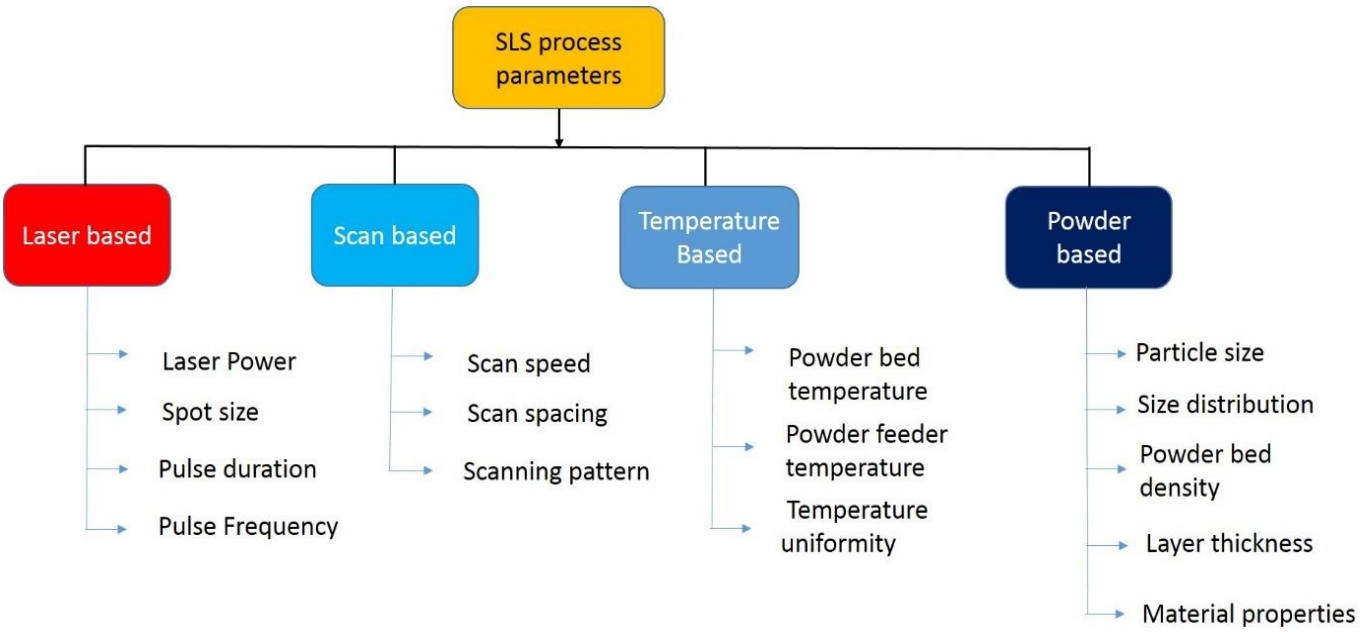

Fig. 1.5 Process parameters of selective laser sintering

1.2.4 Laser Additive Manufacturing (LAM)

Different materials can be processed additively using laser additive manufacturing (LAM), a non-contact process. Layer-by-layer fabrication of components using high-power lasers as the energy source is a common practise in the metal AM technique known as LAM. Aerospace, automotive, electronic, chemical, and biomedical industries are among the ones that use LAM [15]. The main benefit is the ability to fabricate complex shapes without the use of specialised tools, with least amount of manufacturing time and waste. As a result, it does away with the necessity for intricate assemblies when creating complex shapes, and it also offers design flexibility when creating geometries that conventional manufacturing processes cannot produce. One such instance is the production of conformal cooling channels in mould and dies using LAM, which is essential for the cooling effect in casting and injection moulding. Additionally, LAM may construct the entire shape without attaching various components, preventing joint failures and weak structures as a result. Shape design freedom, material design freedom, logistical freedom, and post-processing flexibility are the principal liberties provided by LAM [16]. On the process side, LAM has faster solidification and processing speeds, which results in high cooling rates (105 K/s). In comparison to as-cast samples, this leads to finer microstructure and greater mechanical strength. According to Fig. 1.6, LAM may be broadly divided into two categories: laser-assisted directed energy deposition (L-DED) and laser-assisted powder bed fusion (L-PBF).

The basic difference lies in the methodology deployed for material feeding. L-PBF uses a blade/roller to spread a thin layer on the substrate and uses a laser to melt the powder selectively based on the required shape. L-PBF is further classified based on full melting (selective laser melting) and partial melting (selective laser sintering). But with DED, shapeless material, such wire or powder, are fed directly onto the melt pool produced by a strong laser. For the construction of thin-wall components with intricate characteristics, such as undercuts, overhangs, etc., L-PBF is utilised. But DED can also be used to produce engineering components, repair damaged ones, and remanufacture products. The type of heat source, energy density, scanning speed, scanning strategy, feeding system, and inert gas all have an impact on how productive, capable, and high-quality the AM process is. Most commercially available systems employ high-power lasers, ranging from 200 W to 6 kW. Lasers typically chosen for the LAM process include Nd: YAG, CO2, Fibre, and diode lasers.

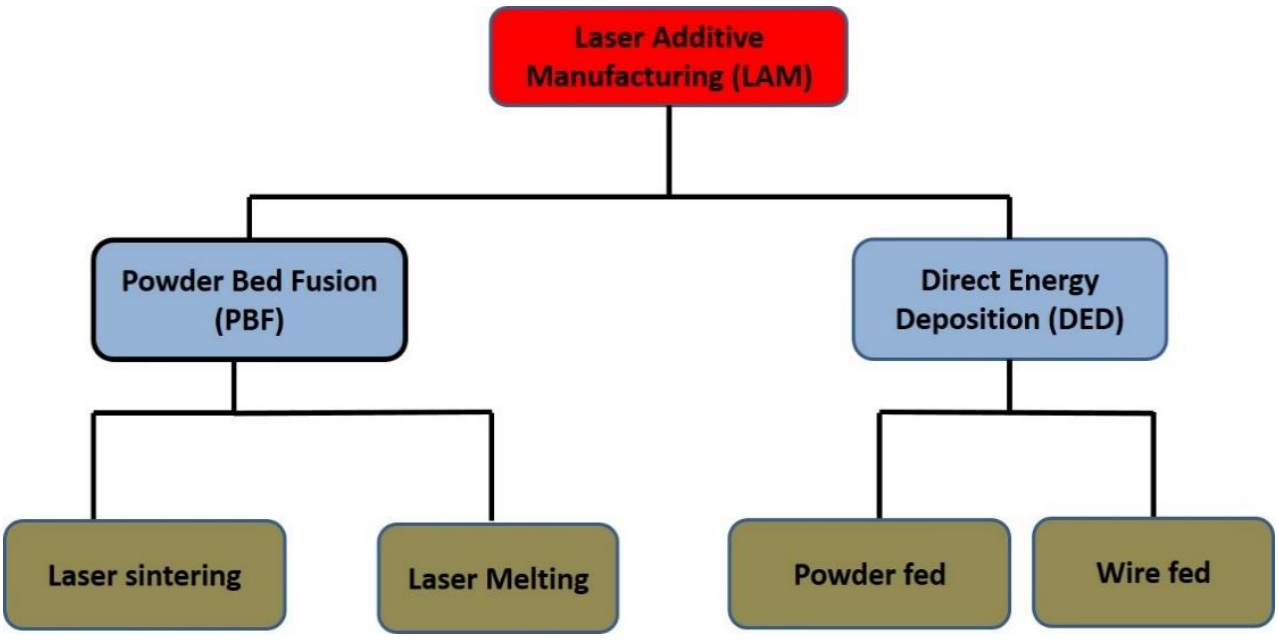

Fig. 1.6 Classification of Laser additive manufacturing process

Laser wavelength affects a metal's absorptivity. Due to their high absorptivity, Nd: YAG, fibre, and diode lasers are frequently chosen for MAM processes. Depending on the process, the spot size can range from 50 to 400 m for PBF and 500 m to 3 mm for DED. The usual process

variables utilised in LAM techniques have a big impact on the component's final composition and mechanical properties.

1.2.4.1 Powder bed fusion process

PBF, a type of additive manufacturing, is utilised to create complicated forms with hollow cooling passages that are extremely high resolution. The two PBF techniques that are most frequently employed are selective laser melting (SLM) and selective laser sintering (SLS). Direct metal laser sintering is another name for SLM (DMLS). Until the desired shape is achieved, the cross-sections are sequentially sintered by the laser using sliced 3D data. Unsintered powder serves as mechanical support during the operation.After post-heat treatment, SLM can produce components with full density. This process is known as "electron beam melting" if an electron beam takes the place of the laser source (EBM). Only a few materials, including Ti6Al4V, Inconel 718, CoCrMo, and Ti grade 2, are treated by EBM because of high operating costs, sluggish processing, constrained processing capacity, and difficulties in tuning process parameters. Contrary to selective laser melting (SLM), it is done in vacuum, which reduces the likelihood of porosity. Brittle materials (intermetallic (TiAl) and entropy alloys (NiCrCoTiVAl)) are challenging to process using SLM due to rapid cooling rates, but effectively treated by EBM technique by maintaining optimal bed temperature of 870 K.

The crucial parts of a PBF are feeding roller, laser, control system, powder bed, inert gas supply system, and powder supply and sintering pistons, as shown in Fig. 1.7. The porosity of the component is significantly influenced by the powder's size distribution, packing, and shape. PBF process uses fine spherical powder with average particle size distribution (10-45 μm). It is suitable for single material processing and unsuitable for multi-material processing. The entire procedure is carried out under an environment of inert gases (argon and nitrogen), which can prevent future unintended interactions between gaseous elements and powdered materials. For instance, when aluminium reacts with atmospheric oxygen, an oxide layer tends to form, which indirectly degrades the component's mechanical qualities. PBF experiences a variety of intricate physics and chemical processes, including as heat and mass transport as well as light energy absorption. Due to the small melt pool size (in microns) and minimal interaction time between the laser beam and powder particles, the PBF process is subjected to high cooling rates (103–108 K/s) (high scanning speeds).

So L-PBF components have not been confined just to prototypes, they have moved towards functional applications. So L-PBF parts are mainly used as functional applications in several sectors. L-PBF has produced many components with different alloys like titanium alloys, cobalt-base alloys, nickel-base alloys, ferrous-based alloys, etc. Among all the ferrous alloys, Precipitation Hardened Stainless Steel has attracted attention because of its wide applications. Among PH steels, 17-4 Precipitation Hardened Stainless Steel have a range of applications and it is one of the widely fabricated materials using selective laser melting because of its applications in aerospace, defense, and medical sectors. This material is also used in marine engineering due to its high corrosion resistance [17]. It has applications as shown in Fig. 1.8

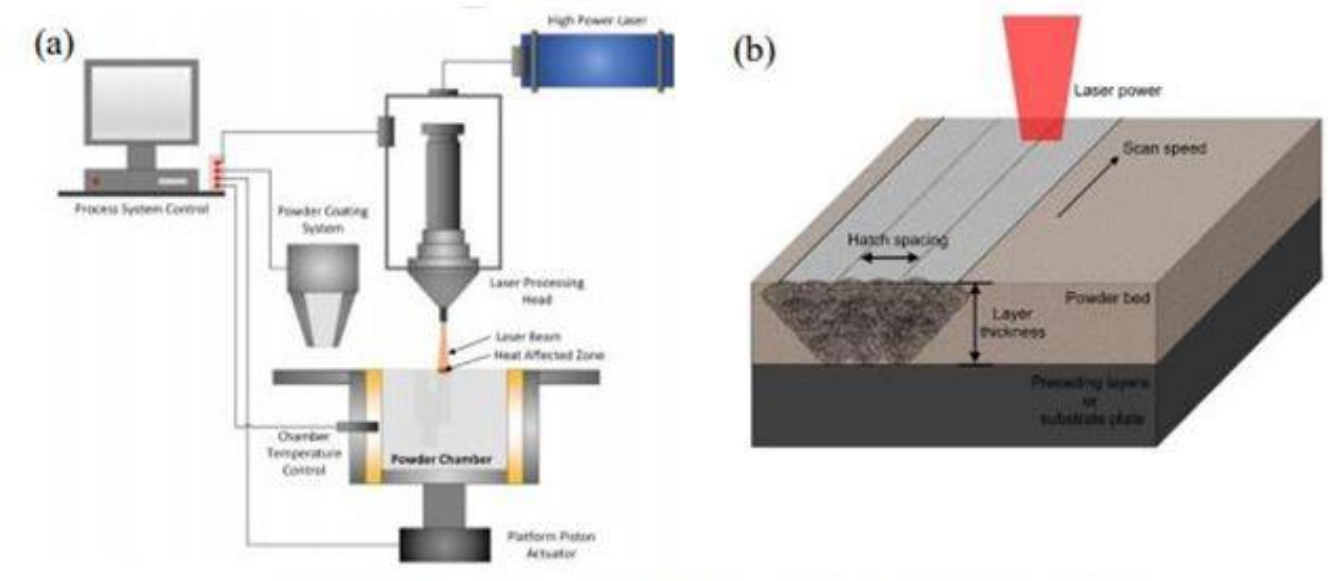

Fig. 1.7. Powder bed fusion (a) process and (b)schematic diagram [18]

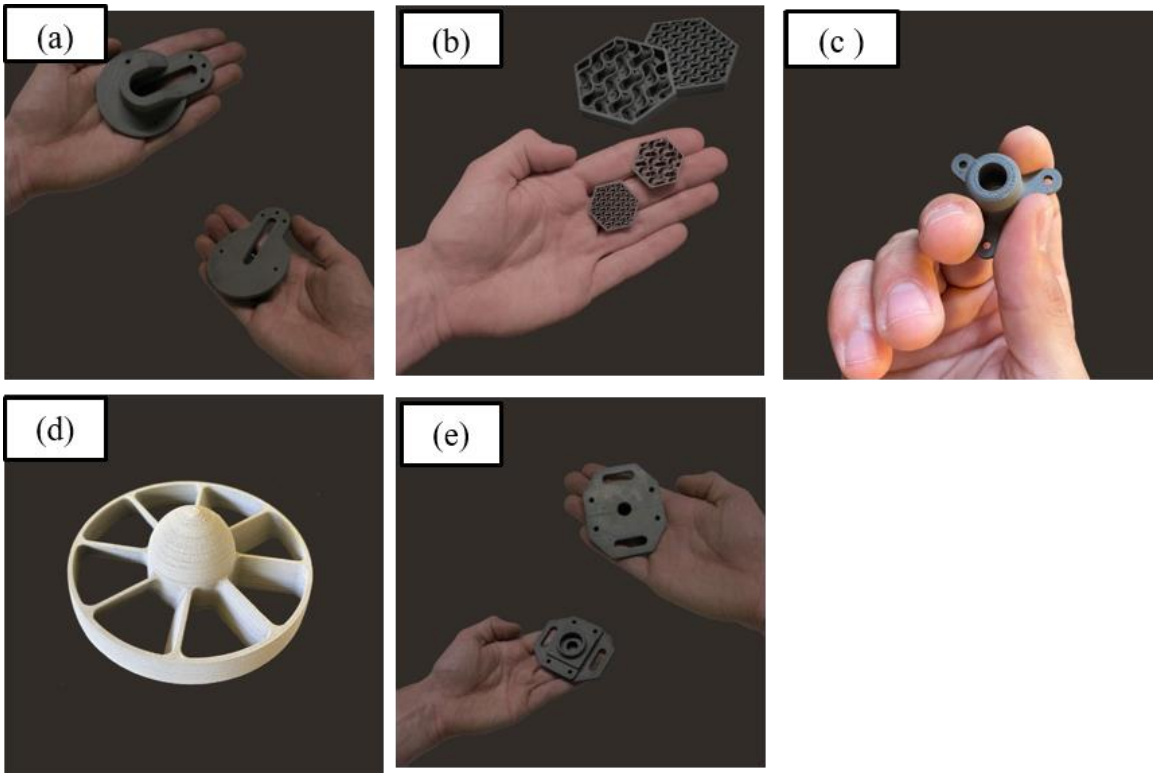

Fig. 1.8. 17-4 PH SS parts (a) Hanger Bracket (b) Gyroids (c) Tripod (d) Turbine (e) Buckle

It is suitable for single material processing and unsuitable for multi-material processing. The entire procedure is carried out under an environment of inert gases (argon and nitrogen), which can prevent future unintended interactions between gaseous elements and powdered materials. For instance, when aluminium reacts with atmospheric oxygen, an oxide layer tends to form, which indirectly degrades the component's mechanical qualities. PBF experiences a variety of intricate physics and chemical processes, including as heat and mass transport as well as light energy absorption.(Fig. 1.9) Due to the small melt pool size (in microns) and minimal interaction time between the laser beam and powder particles, the PBF process is subjected to high cooling rates (103–108 K/s) (high scanning speeds). PBF successfully fabricates titanium, steel, aluminium, copper, and nickel-based alloys and their composites, which performs better than similar alloys made using traditional methods. Further research has focused on promoting additive technology into the various material industries because PBF only works with a limited range of powder materials.

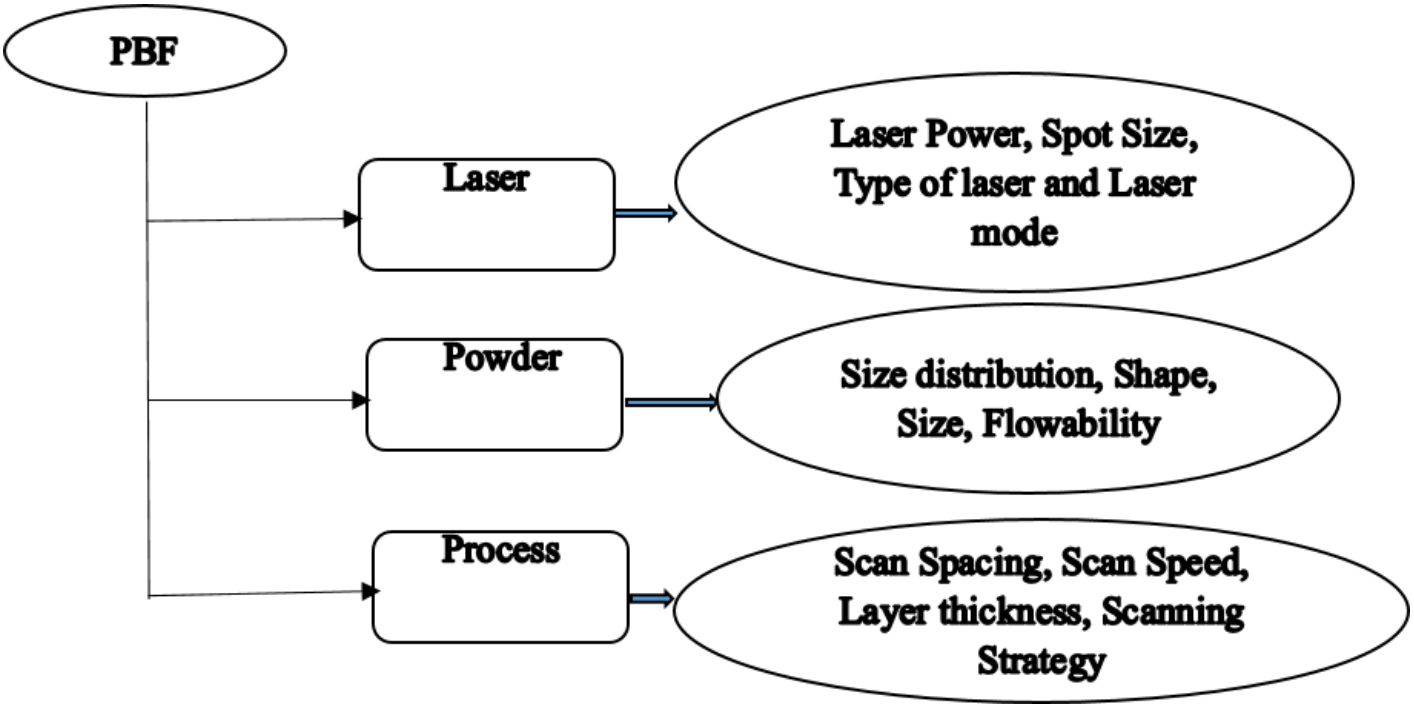

Fig. 1.9 Process parameters involved in SLM process [27]

1.2.4.2 Directed energy deposition

In directed energy deposition (DED), an inert gas is used to prevent the melt pool from oxidising after the laser generates a melt pool on the surface of the substrate or previously deposited layer. A CNC workstation, robotic arm, or other device controls the movement of the laser head or sample. The substrate or sample is typically moved in an XY plane, while the laser head is moved in Z direction. The final 3D engineering component is created by building components layer by layer. Based on the feeding substance, DED is categorized into wire or powder based. Large structures, high deposition rate full density parts, the capacity to repair damaged parts, and the flexibility to use various materials in a single build give DED an edge over other metal AM systems. Depending on the type of material (powder or wire) utilised to construct the component, DED method can be either powder fed deposition (PFD) or wire fed deposition (WFD).

The PFD system consists of a delivery mechanism for powder and gas. Fig. 1.10 shows the usual powder fed DED system .The powder delivery system uses a carrier gas to deliver powder to the point of deposition (Helium and Argon). For reactive materials, argon gas serves as a shield.

It is the most practical and is employed frequently in DED process. The absorptivity of the powder and its numerous internal reflections are key factors in the efficient use of energy. The ultimate deposition rate and mechanical properties of the part depend on the angle at which powder is fed via a coaxial nozzle.

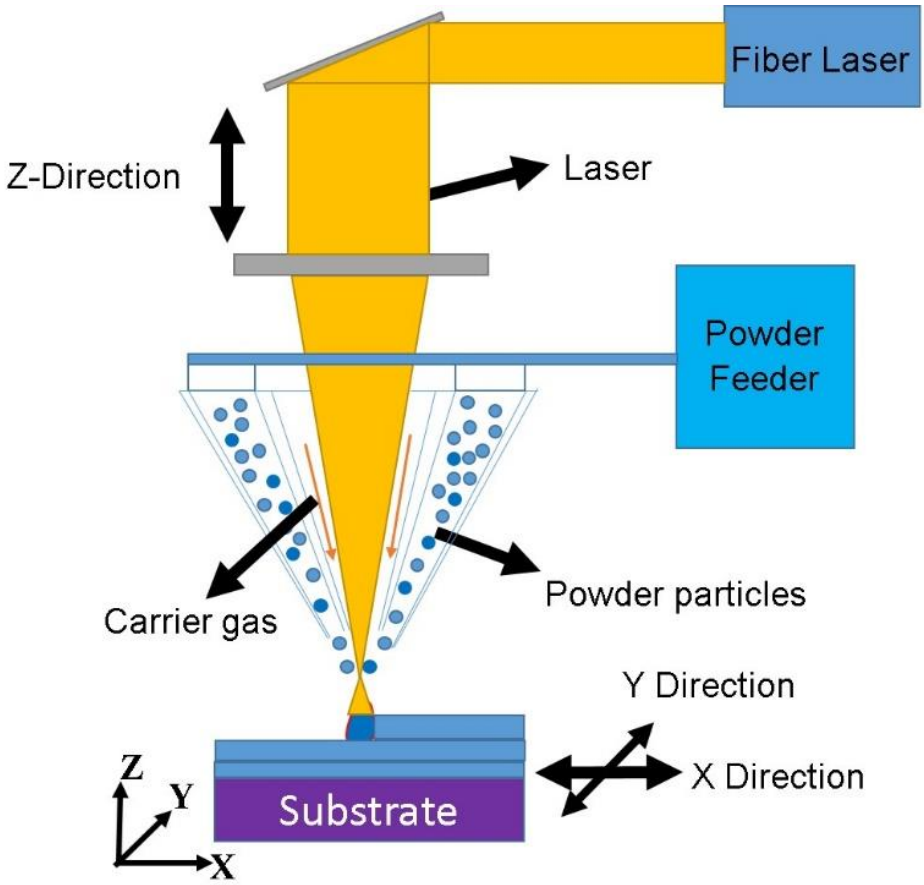

Fig. 1.10 Typical Schematic of PFD system [19]

When laser melts the feeding metal wire from the nozzle in the WFD system, a molten pool is deposited over the substrate or previously deposited layer as depicted in Fig. 1.11. The WFD process rather than PFD process can reach 100% deposition rate. To prevent oxidation, the entire system is sealed off with an inert environment. The characteristics of the material are significantly influenced by WFD process parameters. A steady process depends heavily on the wire feed rate, wire tip position in the molten pool, laser power, laser spot size, traverse speed, feed direction, and feed angle. Changing the angle between the laser beam and wire has an impact

on the wire feed rate and standoff distance. The wire tip's position in relation to the melt pool affects melting efficiency. Uneven deposition is caused by poor wire tip and wire feed rate arrangement, which alters the shape and size of the melt pool. To achieve a smooth surface and a strong metallurgical link between the substrate and the deposited layer, the ideal ratio between beam diameter and wire diameter should be greater than 3. DED is also known as laser engineered net shaping (LENS), direct metal deposition (DMD), 3D laser cladding, direct light fabrication, laser freeform fabrication (LFF), laser-based metal deposition (LBMD), laser consolidation, etc. Based on the type of laser, laser power and spot size, inert gas, powder feed and motion control techniques used, many organisations have given the DED process different names. Fig. 1.12 illustrates the usual process parameters used in DED process. It can construct items in bulk and fix broken components, which can then be used as a substrate or build rate. In comparison to PBF technique, it offers a greater deposition rate, full denser parts, and multi-material in a single build (Functional graded materials) [11]

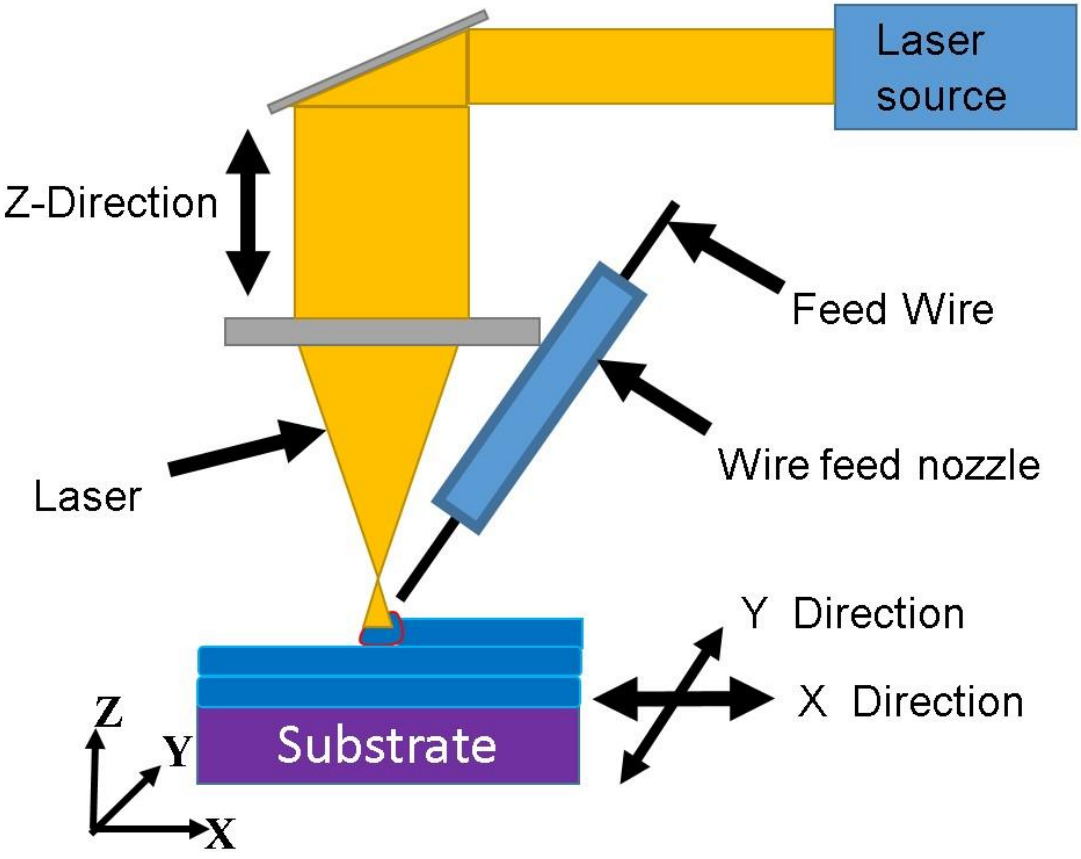

Fig. 1.11 Schematic diagram of WFD system [20]

By regulating the microstructure through chemical composition and heat gradients, one may adjust the mechanical characteristics of a DED deposited part. For a number of engineering applications, DED is effectively utilised to process a wide range of materials, including Fe-based alloys, Ni-based alloys, and Co-based alloys. DED can be used to construct structures that resemble nets without suffering considerable material loss and with less waste of expensive metals like Ni, Cr, and Mo.

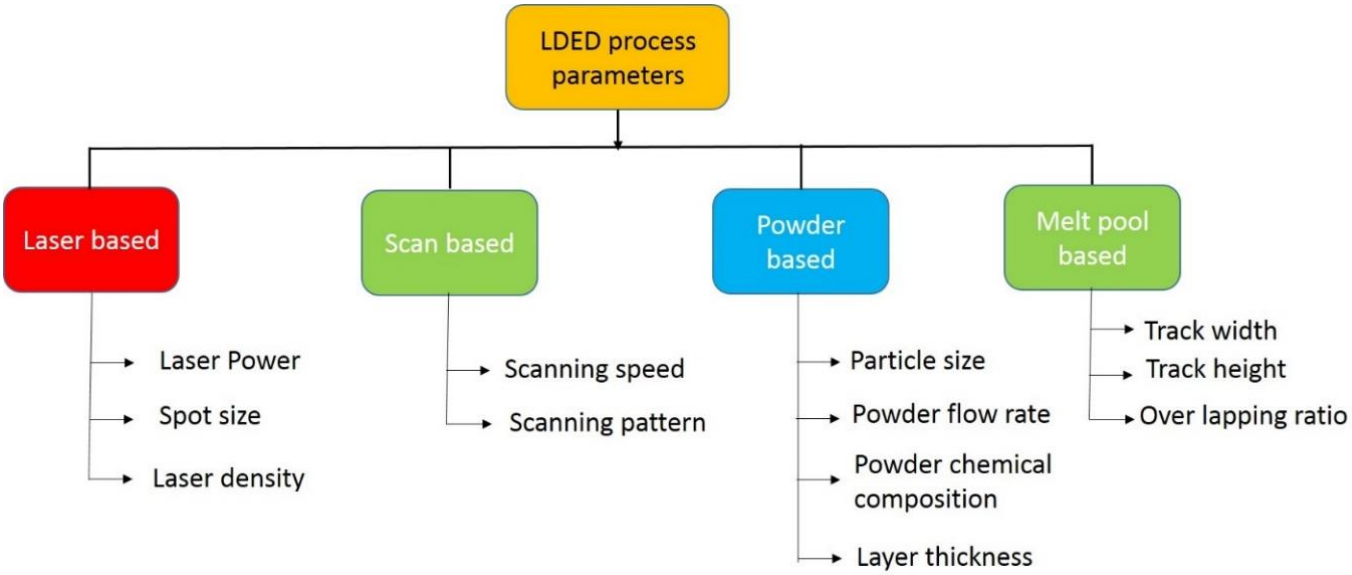

Fig. 1.12 Process parameters of DED system

1.2.4.3 Process parameters involved in PBF process

The amount of laser energy applied to the material determines the final part's mechanical properties. When the laser's power is insufficient for melting, discontinuous tracks are produced; nevertheless, when the laser's power is greater than what is necessary for melting the supplied material, the substrate and previously deposited layer are severely melted. For a specific laser density and contact time, the deposition rate rises with material flow rate up to a threshold value. When it exceeds the threshold value, the samples cross-section turns round and has weak adhesion to the substrate. Laser movement per unit of time can be used to describe scanning speed. For PBF and DED processes, the typical scan ranges are 960-1200 mm/s. Variations in scanning speed have an impact on energy density, as shown in equation (1.1). To optimise the process parameters for bulk deposition, for single track analysis the following equations into account.

$$\text{Energy density} = \frac{P}{V*HD*LT} \quad (1.1)$$

Here, *P* is laser power, *v* is scanning speed, *HD* is hatch distance and *Lt* is layer thickness. The overlap ratio also affects the samples deposition condition

$$\text{Overlap ratio} = \frac{x}{w} \quad (1.2)$$

Here, w is the track width and x is the centre distance between two adjacent tracks. The component's mechanical characteristics are significantly impacted by the laser path. Because of this, choosing a scan strategy is crucial to the procedure.

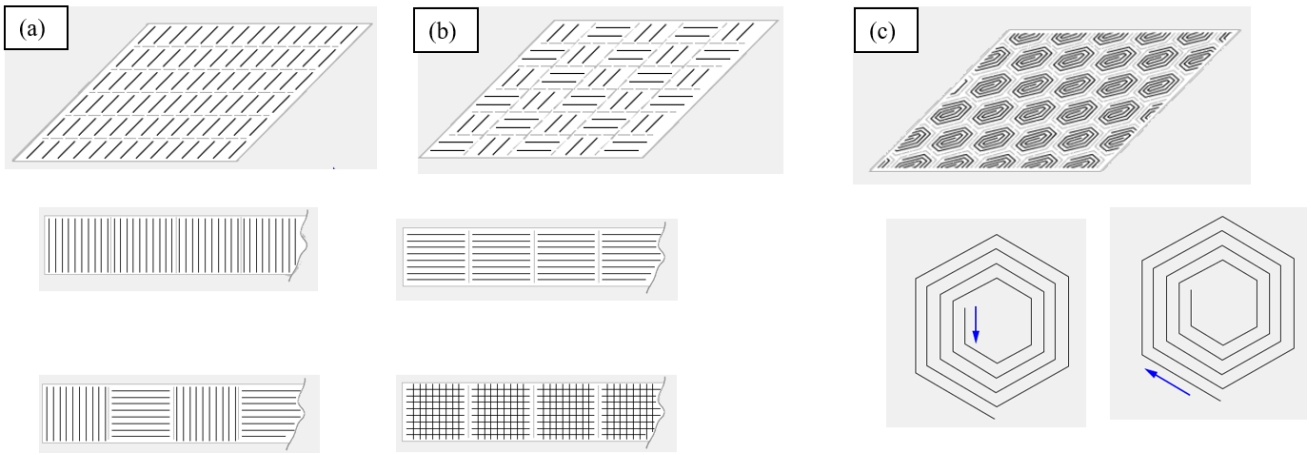

Fig. 1.13. (a) Strip, (b) rectangular and (c) hexagonal Scan strategies used for DMP Flex 100 (Make 3D systems)

Scan strategy usage for L-PBF process is key parameter. The hexagonal inside out scan strategy is commonly used scan strategy inn L-PBF process (make 3D systems). Due to the consistent heat distribution and minimization of residual stresses, rectangular and hexagonal strategy is typically chosen in the L-PBF process.

Hatch angle is the angle formed by the directions of a laser beam as they scan successive layers, as seen in Fig. 1.14. For instance, a 45^0 degree angle between two successive layers shows that the first and eighth levels are identical. In a prior investigation, the change in characteristics with different hatch angles was not statistically significant.

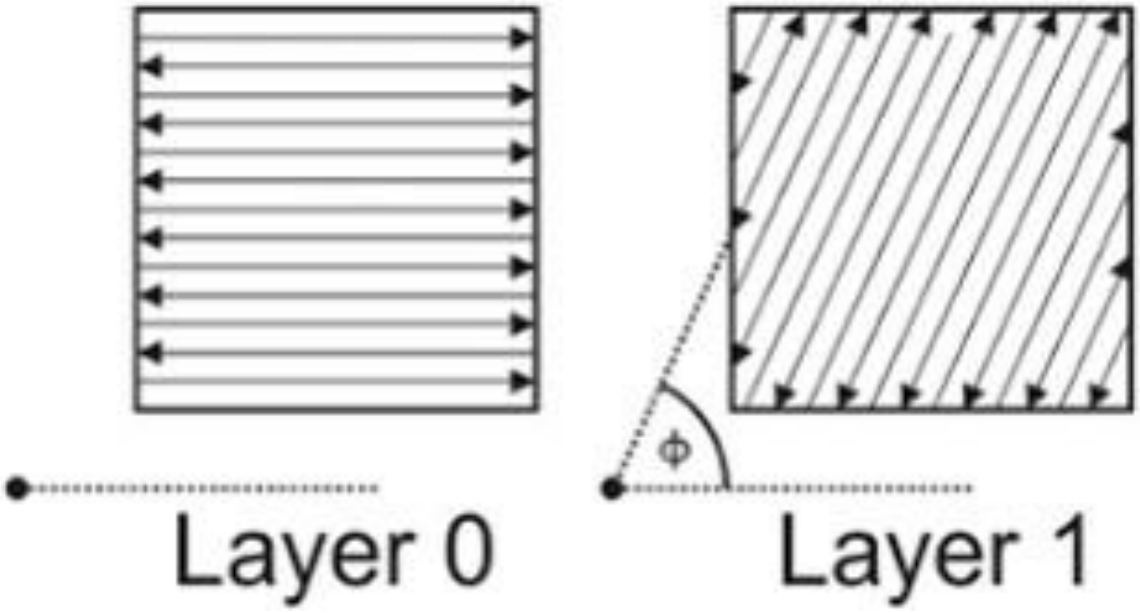

Fig. 1.14 Schematic of hatch angle between two consecutive layers [21]

A shift in build direction, as seen in Fig. 1.15, indicates a change in mechanical characteristics. In comparison to samples made with 0° and 90°, specimens made with 45° exhibit better ultimate tensile strength (UTS) and elongation. This suggests that LAM portions are very anisotropic. For the numbers 0°, 45°, and 90°, the average UTS is 935.57 MPa, followed by 963.50 MPa and 952.97 MPa.

The most important factor affecting the component's surface finish is layer thickness. When the construct part's layer thickness is decreased, an improvement in surface smoothness is obtained in the Z-direction. The change in layer thickness has little impact on mechanical properties. For the PBF process, the typical layer thickness range is 10-100 µm.

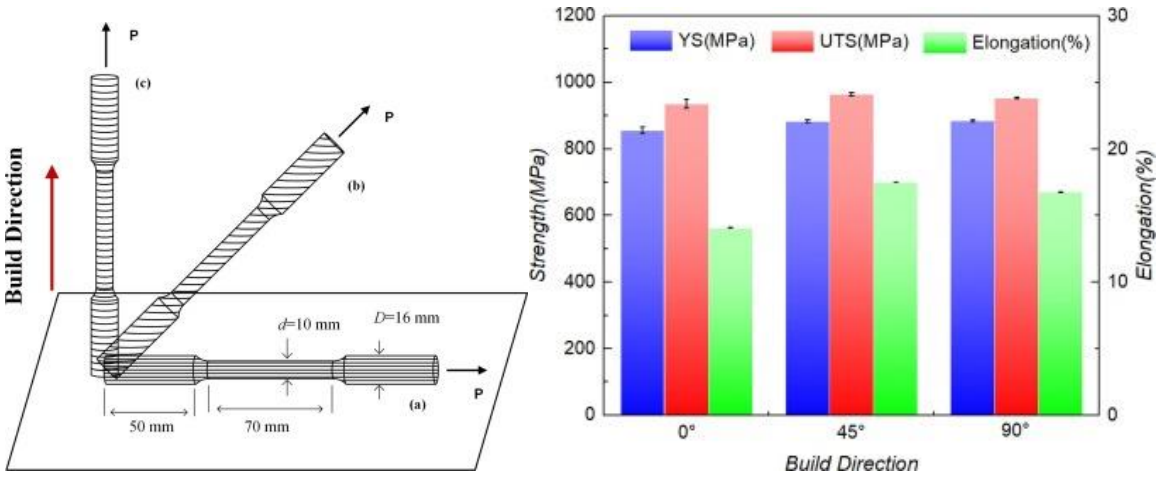

Fig. 1.15 Variation of strength with respect to build direction for (a)tensile samples in different orientation and (b) their strengths [22]

In the metal AM process, flaws such porosity, cracking, delamination, residual stresses, distortion, and balling effect are frequently present. Therefore, in the metal AM process, choosing the best process parameters is considerably more crucial. Table 1.2 displays the types of defects and their respective remedies.

Table 1.2: Typical defects involved in AM process

Type of defect	Reason	Remedies
Porosity and lack of fusion	Entrapped gas, un-melted powder and insufficient over lap	laser power and scanning speed selection, and hot iso-static pressing (HIP)
Delamination and cracking	Generation of residual stresses	Heat treatment
Balling effect	Oxidation of molten pool, high scanning speed and low laser power resulting in low wettability	Optimized process parameters and controlled atmosphere
Stair case effect	High layer thickness and build direction for curved and inclined surfaces	Proper selection of process parameters and build direction
Feature size	Size of the energy source	Process parameters selection and machining
Loss of alloying elements	High laser density, larger surface to volume ratio	Selection of optimum laser power and scanning speed

1.2.4.4 Post treatment of L-PBF process

Major issues with L-PBF process include residual stresses, variations in geometrical form, and unmelted powder. Post-treatment is necessary to address the genuinely new exactly. The built part must first have loose, unsintered powder removed from it, and the supports must then be removed using machining or a band saw. The build portion is removed from the substrate or build plate using wire electrical discharge machining in the L-PBF process. The applications will determine the next stage of post-processing. Ultrasonic machining, glass blasting, polishing, and CNC milling can all be used to increase the surface finish. To enhance the surface finish of the components, laser shot peening (LSP), laser annealing (LA), and laser machining (LM) procedures are successfully used. Rapid heating and cooling cause tensile stresses to build up on the surface of L-PBF components. Using LSP, compressive stresses are introduced into the component, and it

also enhances surface characteristics like corrosion and wear resistance. Inconel 718 that has had LSP processing improves in hardness, wear, and corrosion by 27%, 77%, and 70%, respectively.

To relieve internal stresses brought on by large thermal gradients, post-heat treatment is applied. Additionally, it is used to change the component's mechanical properties and the grain size, orientation, and porosity. Annealing is frequently used to reduce internal stresses, and precipitation-hardened materials are frequently subjected to solution heat treatment followed by ageing. Solution heat treatment dissolves undesired phases, whereas ageing enhances hardness by forming and promoting precipitation phases. By using hot isostatic pressing, metal AM flaws including porosity, voids, and cracks inside the component are eliminated (HIP).

1.3 Motivation

High cooling rates (105 K/s) are possible with laser additive manufacturing (LAM), which has faster processing and solidification velocities. In comparison to as-cast samples, this leads to finer microstructure and better mechanical strength. For processing a wide range of materials, including iron-based alloys, nickel-based alloys, cobalt-based alloys, etc. for diverse engineering applications, L-PBF is one of the LAM processes. However, L-PBF can be a viable choice for creating structures that are – near net-shaped without incurring appreciable material losses.

Due to its exceptional qualities, such as high strength, corrosion fatigue resistance, etc., 17-4 PH SS(17-4 PH SS) is utilised in a variety of engineering applications in aerospace, energy, automotive, nuclear, and marine sectors. Although 17-4 PH SS manufactured components are produced using traditional manufacturing techniques, this method is expensive to use for producing complexly shaped components. L-PBF technique is used to fabricate complicated 17-4 PH SS parts at the lowest possible cost. Although it has many uses, it can only be employed in a limited number of applications because to its poor damping capacity and fatigue strength.

Therefore, maximal hardness and density are used as the basis for the parametric investigation. As-deposited 17-4 PH SS, and heat-treated samples are used in microstructure, micro hardness, and corrosion investigation. Studying damping capacity and fatigue strength of the 17-4 PH SS under various conditions was also done.

1.4 Organization of thesis

Chapter-1: Introduction

The advantages of AMover traditional procedures are addressed in Introduction. The chapter also focuses on the classification of metal additive manufacturing. Binder jetting, selective laser sintering, laminated object manufacturing, powder bed fusion, and directed energy deposition are examples of MAM-based methods that are highlighted along with their advantages. The fundamental process variables and post-processing steps involved in the MAM process are explained.

Chapter-2: Literature review

The goal of the literature review is to provide comprehensive information about the mechanical properties and microstructure of 17-4 PH SS and other materials produced by L-PBF. It also explores how the microstructure and mechanical properties of 17-4 PH SS are affected by post-heat treatment. The damping capacity and fatigue strength for 17-4 PH SS made by L-PBF were also discussed.

Chapter 3 : Experimental Methods

The goal of experimental methods is to give an overview of the materials, experimental methods used. The various characterization tools that are used for conducting experiments were also discussed.

Chapter-4: Parametric investigations and characterization of 17-4 PH SS samples made by L-PBF

A parametric analysis of stainless steel 17-4 PH produced by L-PBF is carried out. Using a full factorial experimental design, samples were deposited by altering the laser power, scanning speed, and scan technique. Investigation is done into how the L-PBF process parameters affect density and micro-hardness. The impact of process factors on the microstructure and corrosion resistance of the 17-4 PH SS was also discussed in the current study.

Chapter-5: Influence of scanning strategies on microstructure, residual stress, and corrosion behavior of 17-4 PH SS fabricated by selective laser melting

The effect of different scan strategies like hexagonal (inside out and outside in), rectangular (horizontal, vertical, alternate and both), strip(horizontal, vertical, alternate, and both) on the microstructure, residual stresses, and corrosion behavior of the 17-4 PH SS fabricated by selective laser melting.

Chapter-6: Influence of hexagonal scanning strategy island size on microstructure, micro hardness and residual stress of 17-4 PH SS made by SLM

The effect of hexagonal scan strategy island size on the microstructure, micro hardness, residual stresses and corrosion behavior of 17-4 PH SS fabricated by selective laser melting with a scan rotation angle of 90 degrees.

Chapter-7: Effect of heat treatment on the damping behavior and fatigue strength of L-PBF 17-4 PH SS

As built samples were made by laser powder bed fusion and different heat treatments were done to understand the microstructure, hardness, frequency-dependent, and temperature-dependent damping characteristics.

Chapter-8: Conclusion and future scope

CHAPTER 2

LITERATURE REVIEW

2.1 Parametric investigation and characterization of 17-4 PH SS parts fabricated by selective laser melting

Taban et al. [23] investigated the impact of processing parameters on microstructures and mechanical properties of 316L stainless steel fabricated by SLM. They reported that samples at higher scan speeds have finer microstructure, greater density, and better mechanical properties because of high cooling rates. Thijs et al. [24] provided a detailed description of the influence of process parameters on the microstructure of Ti–6Al–4V processed with SLM. They reported that microstructure variation was due to faster cooling rate and better melting of previous layers. They also stated that scanning strategy defines the position of the elongated grains, which is dictated by the local heat transfer condition (and part geometry). Dai et al. [25] investigated the impact of energy density on SLM microstructure of aluminum parts. They found that increased energy density results in a lack of fusion porosity and entrapped gas porosity. Wang et al. [26] used a meander scan strategy to fabricate SS 316L samples with laser power ranging from 200 to 400W. They stated that porosity decreases as energy density increases and stabilizes after a particular stage. They also reported that cell structure changes from fine to coarse with an increase in energy density. Ali et al. [25] reported that the rectangular alternate scan strategy showed higher hardness than strip alternate scan strategy for all samples due to faster cooling rates and complete powder melting between two laser tracks. Bian et al. [27] found that a decrease in laser power resulted in decreased residual stresses for Al-Mg alloy. They also reported that the strip scan strategy showed more residual stresses than checkerboard scan strategy. Lashgari et al. [28] investigated the influence of hexagon scan strategy with 25000μm radius and 100μm overlap between two hexagons and concentric scan strategy on the microstructure and mechanical properties of additively manufactured 17-4 PH SS. They reported that the weld pool geometry was same for both strategies in vertical direction, but there was a smaller molten pool for horizontal samples because of lower cooling rate and uniform dispersion rate (Fig. 2.1). They also stated that the hardness and corrosion resistance of the hexagonal scan strategy was higher than that of concentric scan strategy due to low defects and porosities in the volume fraction.

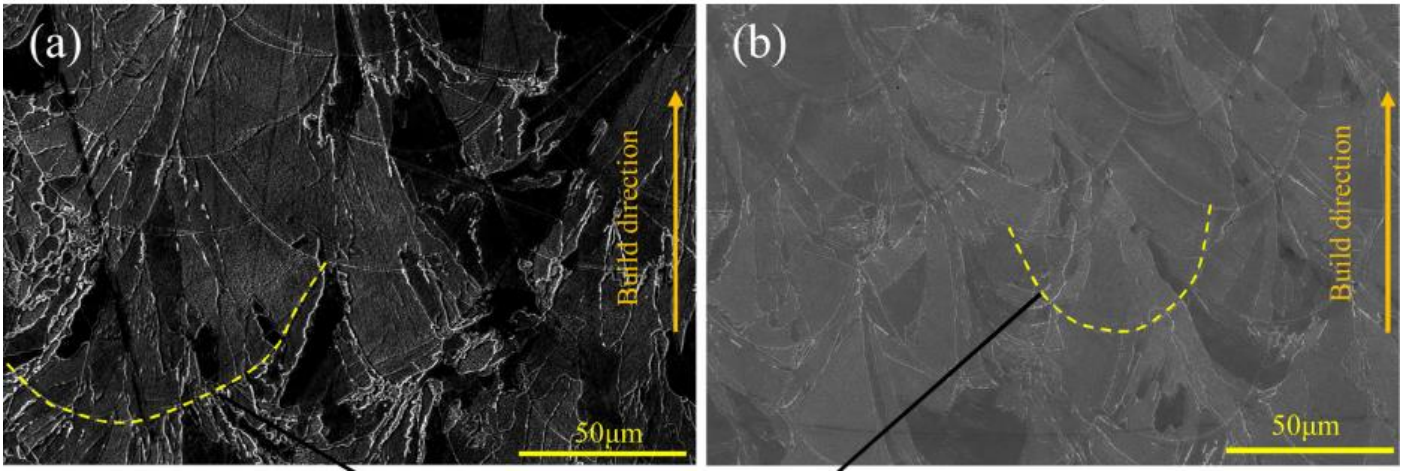

Fig. 2.1. Weld pool geometry for SLM samples along build direction

Wu et al [29] reported that corrosion behavior was influenced by cathode reactions and microstructure for 17-4 PH SS fabricated by SLM. Swaroop et al [30] reported that pitting corrosion of 17-4 PH SS SLM occurred at delta ferrite regions for as-built samples and this delta ferrite phase in the matrix acts as a strong pit initiator (Fig. 2.2).

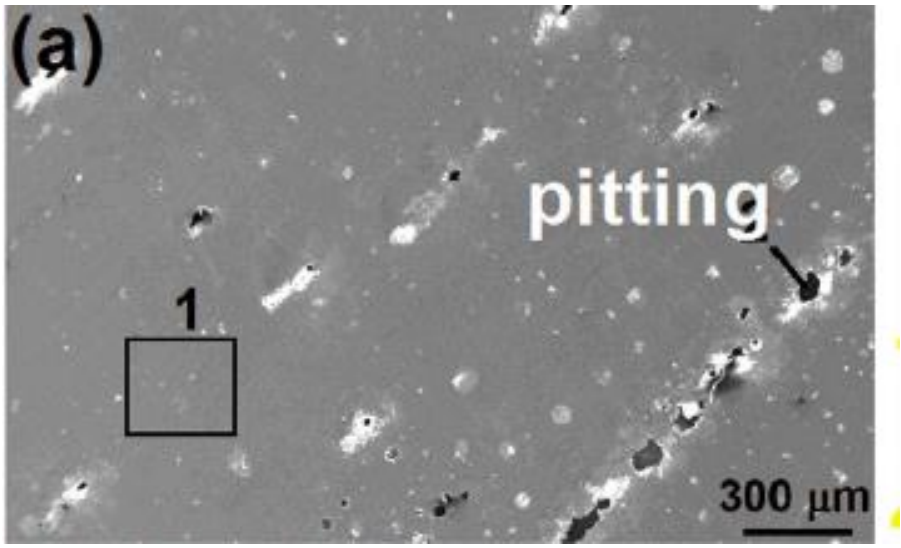

Fig. 2.2. SEM image of corroded specimen

P. Ponnusamy[31] investigated the influence of varying defocus distance at a constant laser power on the surface roughness, microstructure, and hardness of the samples of 17-4PH stainless steel processed by SLM ProX200 machine. For getting good quality parts and mechanical properties, it is required to optimize process parameters. Michella Alnajjar[32] investigated the microstructure,

yield strength, hydrogen embrittlement and fracture mode of SLM and wrought 17-4 PH SS .Microstructure of SLM ed contains more austenitic grains elongated along the building direction and more than wrought steel. The yield strength was also 10% more than wrought steel The hydrogen embrittlement, crack initiation and propagation of SLM parts are more than wrought steel because of higher grain size. The fracture surface of wrought steel showed a brittle intergranular fracture mode close to the surface and a ductile mode at the center. The subcritical crack growth and the final fast overload fracture were obtained by transgranular cleavage in SLM parts. Anton Zhukov et al [33] studied the strength characteristics of steel specimens after SLM of powders 17-4 PH, SS316L, 324. He reported that hardness depends on construction parameters and carbon ratio. E.murr [34]investigated the initial microstructure by OM, SEM, XRD, TEM. The martesnitic powder produced in nitrogen environment gives martensitic structure (Fig. 2.3), while austenitic powder produces austenitic part. But in argon environment, both give martensitic structure .This is due to rapid cooling affected by nitrogen gas as the thermal conductivity of nitrogen is 40% more than that of argon gas.

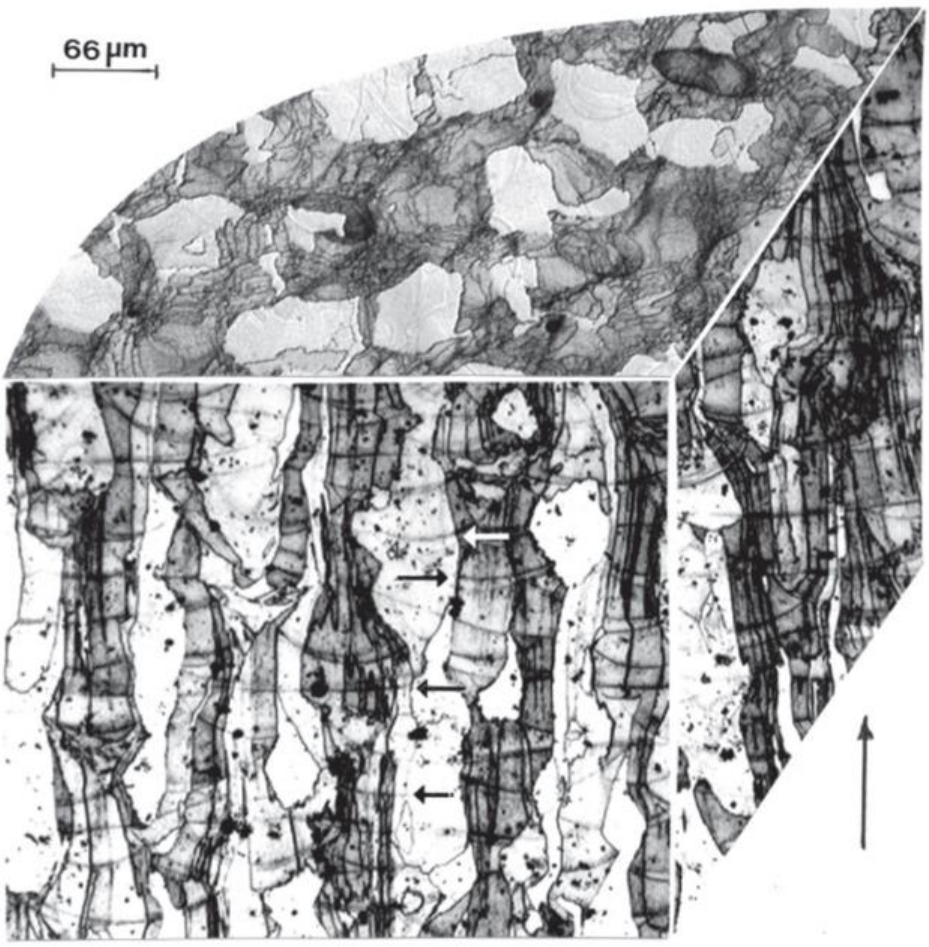

Fig. 2.3. Microstructure of 17-4 PH SS in 3D representation

The hardness for both powders , as fabricated and tempered samples, was calculated and compared with Rockwell c and Vickers hardness tester. G.Durshun et al[35] reported the effect of laser power and scan speed on the surface characteristics and density of SLM316L Parts. Higher laser power and lower scan speed results in better surface characteristics and fewer defects. Laser power significance is much more than scan speed. The oxygen and carbon concentration at melt pool boundaries induces cracks and balling effect in overlapped regions.

Swathi Vunnam [36] investigated the effect of chemical composition on the microstructure of the 17-4 PH SS made by SLM in as built condition. By changing the alloy composition without any heat treatment fully martensitic structure was obtained.(Cr/Ni equivalent change)[DMLS]. Andelle kudzal [37] investigated the effect of scan strategy (Fig. 2.4) on the microstructure and mechanical properties of SLM 17-4 PH SS. The microstructure contains dual ferrite-austenite phase

composition (Fig. 2.4). When the scan lines perpendicular to load direction, the retained austenite (only 25%) was half compared to scan lines parallel to load direction. Change of direction within the scan line path results in delamination porosity and change in volume of retained austenite.

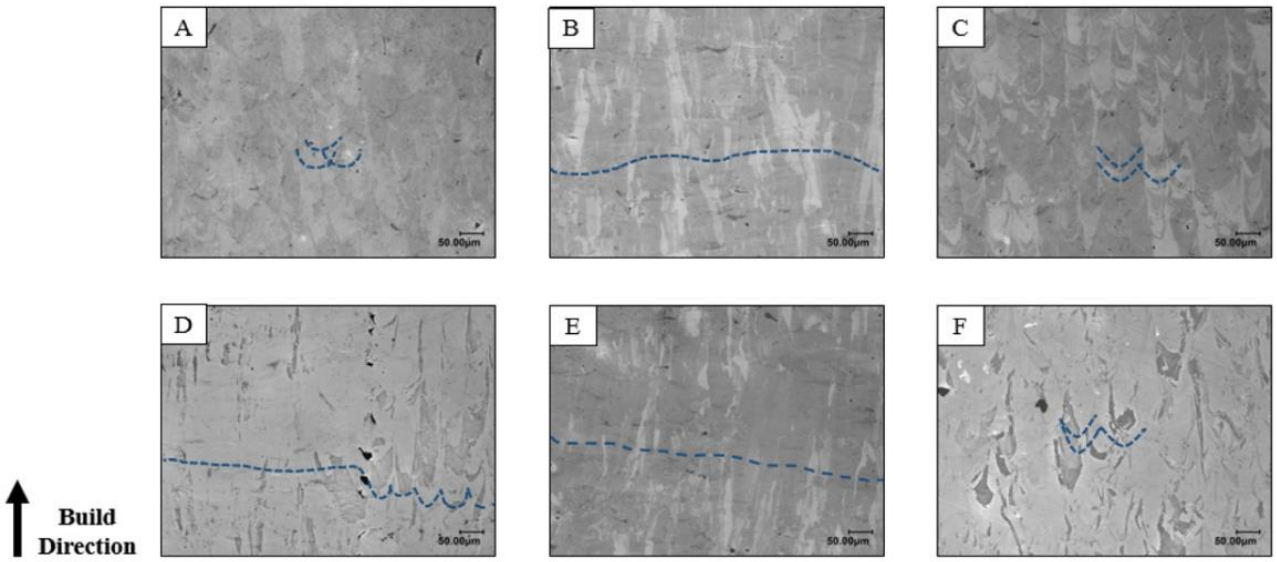

Fig. 2.4. Optical micrographs of samples with different scan strategies used for experiment

2.2. Influence of scanning strategies on microstructure, residual stress, and corrosion behavior of 17-4 PH SS fabricated by selective laser melting

Zhao et al. [28] reported that scanning strategy and scanning direction were discovered to be the most effective processing parameters for fabricating a SS316L component. They also reported that for a 90-degree scanning direction the mechanical and corrosion properties improved due to the formation of smaller grain size. Jiang et al. [38] reported that the alternating strategy had higher density and better mechanical properties than horizontal scan strategy due to alternating melt pool and low thermal gradient for steels. Wan et al [39] reported that scan strategy-X showed better density, lower void distribution than scan strategy-XY for Inconel 718 specimens fabricated by SLM. Tarun et al. [40], [41] reported that 90-degree scan direction specimen showed better density and better mechanical properties compared to 0 scan direction for maraging steel and its properties were similar to that of wrought alloy. They also reported that XY scan strategy density was better than X scan strategy because of alternating molten pools and strong particle fusion while there was the frequent deposition of tracks and thermal background in the bidirectional X scan technique in

maraging steel. Bian et al. [42] reported that the strip scan strategy showed more residual stresses than the checkerboard scan strategy for Al-Mg alloy due to large thermal background and scanning track for strip scanning strategy (Fig. 2.5).

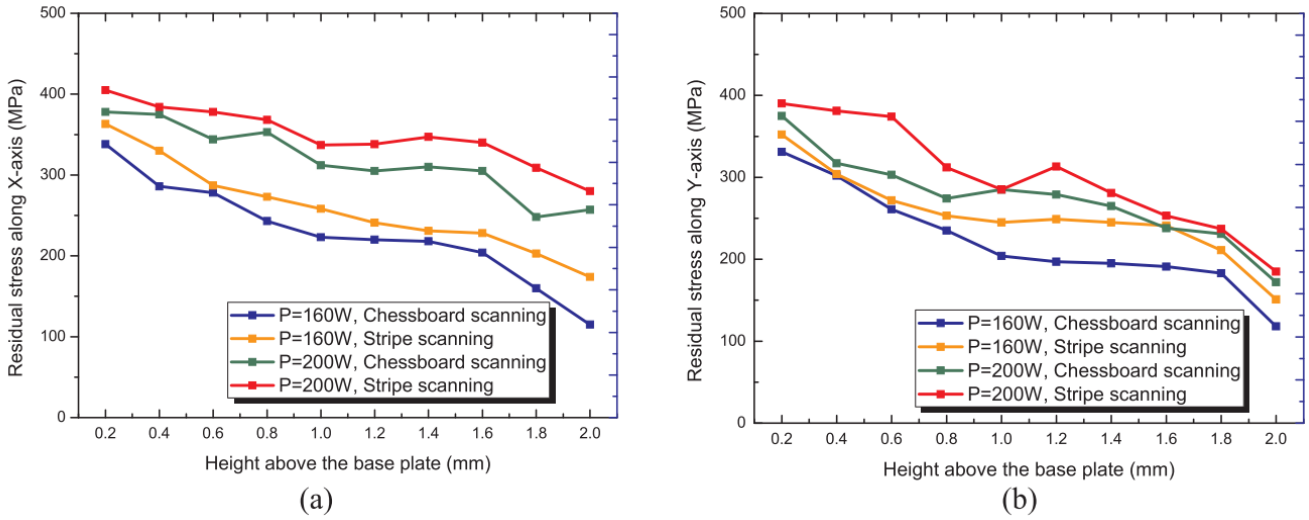

Fig. 2.5.Residual stresses representation from the base plate[42]

Kruth et al. [43] looked into the effect of island scanning strategy on the microstructures and textures of AlSi10Mg alloys processed by SLM. They reported that islands act as stress releasing zones for island scanning strategy. Rashid et al [23]investigated the effect of two different scanning strategies on density and microstructural phase composition and micro hardness and the effect of different HT on phase composition and micro hardness was also analyzed. The samples with double scan strategy showed high hardness and more density compared to printed parts with single scan strategy. Sun et al [44] investigated the effect of scan strategies on the microstructure and mechanical behavior of SS316L fabricated by SLM. The microstructure, grain growth, grain size and mechanical properties of SS316L are affected by scan strategies. Applying scan strategy with rotation angle between successive layers breaks columnar growth and formation of fine equiaxial grains which leads to good tensile strength and tensile properties. Micro hardness was also improved by hexagonal scan strategy.

2.3 Influence of hexagonal island size on microstructure,micro hardness, residual stresses and corrosion behavior of 17-4 PH SS made by SLM

Kong et al. [5] studied the impact of laser power on L-PBF-fabricated 316L stainless steel and found that increasing laser power improved mechanical properties. Robinson et al.[8] reported that 90 Scanning rotation angles resulted in better mechanical properties for L-PBF components and alternate scan strategy reported low residual stresses because of alternate molten pools. Rashid et al. [9] stated that second scan for 17-4 PH SS alloy revealed that residual austenite turned into martensite, led to reduction of voids, gas porosities, and balling particles between layers, resulting in improved efficiency. The impact of hexagon and concentric scan techniques on the microstructure and mechanical characteristics of additively made 17-4PH stainless steel were examined by Lashgari et al. [16]. According to their results, the vertical weld pool shape was the same for both strategies, but the horizontal samples' molten pools were smaller due to slower cooling rates and more uniform dispersion rates. For Ti6Al4V alloy, Ali et al. [17] observed that residual stresses were lower with a 90^{o} scan rotation direction and that there was no relationship between variation in mechanical properties and scan strategy. According to Hao et al. [18], the best processing parameters for producing a component were found to be scan speed, scanning method, and laser power. Additionally, they noted that when laser power increased, particle fusion also increased, causing a decrease in porosity and a variation in the heights of sintered layers. Toyserkani et al. [10] reported that as laser power increased, the weld pool narrowed and grain refinement occurred at high laser power. They also stated that different island sizes often imply different scanning vector lengths during the L-PBF operation, which result in different residual stresses. Wang et al [11] reported the nature of thermal behaviours within molten pools because of which residual stresses could significantly influence island size. Lu et al [12] reported that at lower island size,the mechanical properties and residual stresses of Inconel 718 checker board strategy tends to be optimal compared to higher island sizes because of stress release from cracking during SLM process. H.Zhang et al[27] reported that influence of island size in checker board strategy on microstructure, surface quality, residual stresses and corrosion resistance of SLM Al-Mg alloy. The minimum residuals stress and higher corrosion resistance was obtained for medium scan strategy. Surface smoothness was good for smaller island size. The residual stresses were more for 1.2 mm island size as the total scanning time and scanning length. The residual stresses were fewer

at 2.4 mm island size. Higher residual stresses are there for larger island size as the temperature gradient and scan lengths were high.Higher corrosion resistance was obtained for moderate island size (4.8mm).The massive island borders in small island size led to increase of molten pool boundary.The molten pool also increased with large island size due to disorder caused by numerous molten pools, as shown in Fig. 2.6.

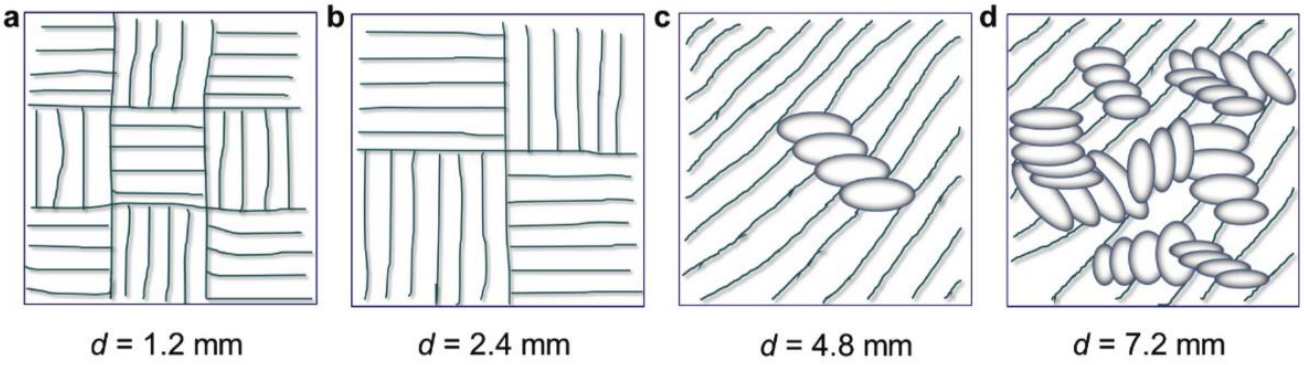

Fig. 2.6. Molten pool configurations for different checkerboard island size samples

2.4. Impact of heat treatment on the microstructure, damping and fatigue behavior of 17-4 PH SS

J. Hebert[45] investigated the microstructure and phase evolution of additively manufactured and wrought 17-4PH SS alloy and the effect of heat treatments like solution annealing and aging was investigated. The microstructural studies demonstrate that 17-4PH AM components can achieve microstructures and hardness similar to those of wrought samples by post-built heat treatments. Zhiheng Hu [46] investigated the influence of separate processing parameters on the density, defect, micro hardness and the influence of heat-treatment on mechanical properties. Density was affected by scan velocity and slice thickness. The effect of hatch thickness was evident on scan velocity. The microhardness was affected by scan velocity, hatch spacing and slice thickness. The yield strength of the heat treated sample increases significantly and the elongation decreases due to the transformation of microstructure (Fig. 2.7) and the changes in the precipitation strengthening phases. Aref Yadollahi et al [47], [48] investigated the effect of build direction and heat treatment on fatigue behavior of SLM build 17-4 PH SS parts. Post SLM heat treatment was necessary in order to improve its tensile strength and fatigue behavior. The heat treatment on HCF made it sensitive to impurities and crack initiation stage dominated the total fatigue life time. The

application and utilization of SLM parts depends on their mechanical properties which are influenced by the defects. Various process parameter combinations results in a unique and complex thermal history and temperature field leads to different cooling rates and mechanical properties. Build direction has impact on aspect ratio and mechanical properties. The influence of heat treatment on fatigue crack growth was not evident but the build direction of the sample showed much impact on fatigue behavior of L-PBF samples. (Fig. 2.8)

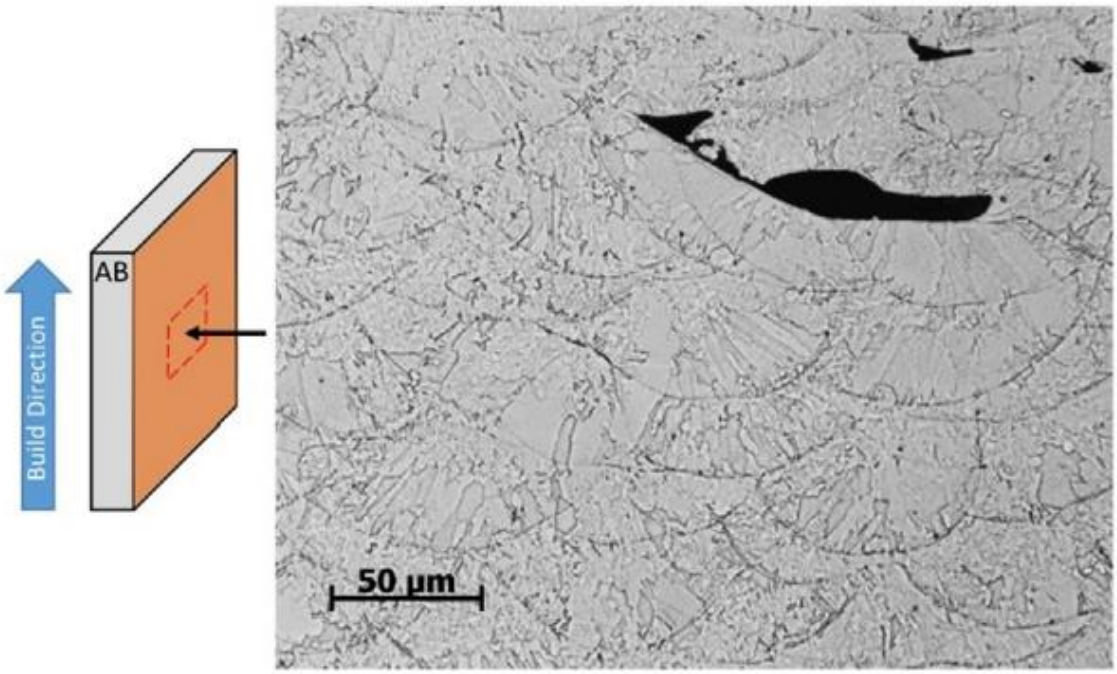

Fig. 2.7.Optical micrograph showing lack of defects for sample along build direction

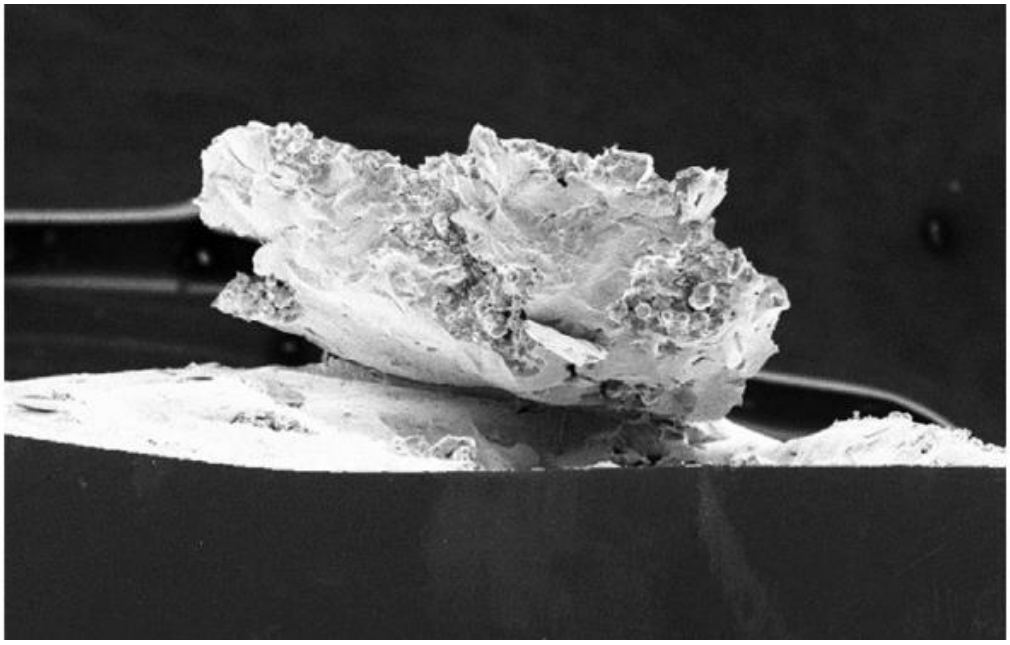

Fig. 2.8. Delamination crack fracture surface of MC (T) Specimen

Yanyao Jiang et al [49] investigated the static and fatigue experiments on the AM and CM 17-4PH SS in ambient air. The tensile strength of both materials was almost same and the ductility of AM 17-4PH SS parts was lower than that of CM part .Fatigue experiments were conducted under fully reversed strain condition and with strain amplitudes ranging from 0.15% to 1.0%.fatigue limit and strain life fatigue curves of both materials were calculated. Defects and porosity affected the weakened fatigue properties and ductility of AM part. Ashish Kumar Nath [19] investigated the effect of heat treatment on microstructure, mechanical and corrosion properties of 15-5PH SS parts made by SLM process. Microstructure and its effect on mechanical properties and corrosion properties were investigated. Aging condition (H900) increases yield strength, hardness and corrosion resistance through the formation of fine spherical ε-Cu-rich precipitates. (H1150) make the specimen ductile having relatively low yield strength, hardness but high impact energy. Solution annealing was found to reduce anisotropy in mechanical properties through the homogenization of microstructure. Solution annealing before aging is recommended for the homogeneity in microstructure (Fig. 2.9). Sudha Cheruvathur [50] investigated the effect of stress relieving on the microstructure and properties like hardness of AM 17-4 PH and conventional materials. The hardness was increased but stress relieving for 1h was not having the effect on directionally solidified microstructure. Even for wrought material it was insufficient to alleviate the segregation of microstructure.

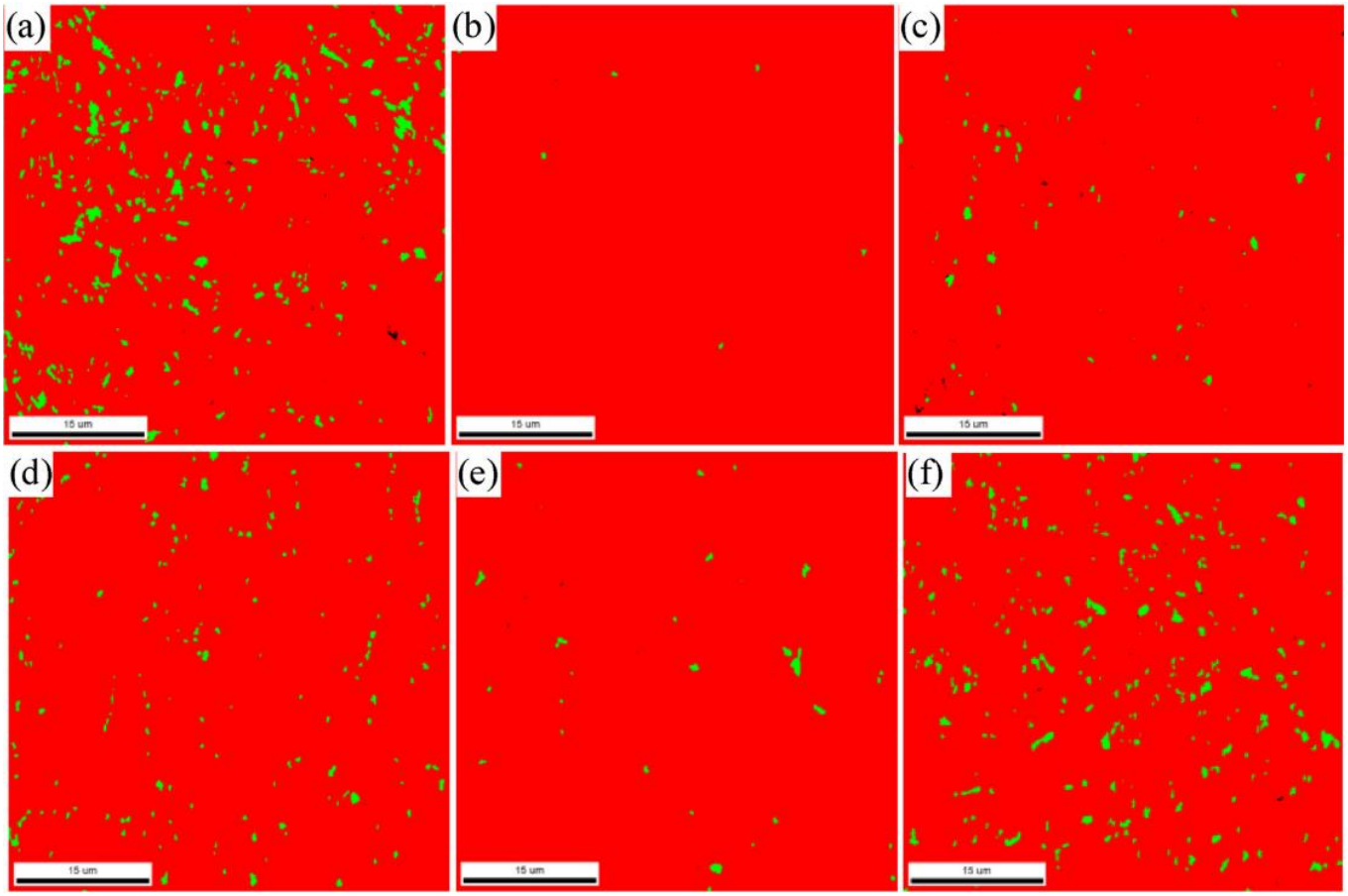

Fig. 2.9. EBSD analysis showing the amount of retained and reverted austenite[19]

The literature review of 17-4 PH SS and 15-5 PH SS under as built and heat treatment condition and their study were summarized in Table 2.1.

Table 2.1. Literature summary of the 17-4 PH SS and 15-5PH SS under different conditions

S.No	Material	Type of Study	Conclusion
01	17-4 PH SS	Microstructure & texture before Heat Treatment	Microstructure of the as- fabricated samples consists of austenite and martensite while some pores resulted because of entrapment of gas
02	17-4 PH SS	Microstructure & texture after Heat Treatment	Martensite and retained austenite was obtained after completion of Heat Treatment some studies has shown that martesite percentage changed after solution annealing and aging
03	17-4 PH SS	Effect of fabrication environment and atomizing media	Fabrication atmosphere also has impact on phases of 17-4 PH SS microstructure
04	17-4 PH SS	Effect of porosity and Density	Medium scan speed giving higher denser sample because of complete melting of the sample and zero pores in the sample
05	17-4 PH SS	Effect of powder reuse	By reusing powder, the powder properties influence the density and surface roughness of the produced part
06	17-4 PH SS	Effect of Heat Treatment on Micro Hardness	By Aging Heat Treatment, the Hardness was higher and samples are isotropic due to martesnite and precipitation of Cu rich particles. Stress relieving also reported that the Hardness was increased slightly when compared to as fabricated sample
07	17-4 PH SS	Effect of Heat Treatment on Yield Strength and Elongation	Heat treatment samples have lower elongation and higher yield strength compared to as built samples
08	17-4 PH SS	Effect of Heat Treatment on wear strength	Wear rate is less for L-PBF 17-4Precipiation Hardened Stainless Steel samples than Conventionally 17-4 PH SS in lubricated condition because of higher Surface Roughness.
09	17-4 PH SS	Influence of Heat Treatment on Corrosion Properties	Corrosion potential of 17-4 PH SS(even for both gas and water atomized parts) is better than the wrought parts
10	17-4 PH SS	Effect of Heat treatment on fatigue properties	Heat treatment will only benefit low cycle fatigue but not high cycle fatigue.The fatigue properties of 17-4 PH parts with the with the variation of part location on build plate and reuse of powder was insensitive in as fabricated condition
11	15-5 PH SS	Effect of Heat treatment on all Properties of 15-5 PH SS SLM	Aging done after completion of Solution Annealing is recommended for the homogeneity in microstructure for 15-5 PH SS AM parts. Wear and Corrosion Potential of Additive Manufactured Parts are more than Conventional Parts

2.5. Summary

It is observed that the effect of SLM process parameters on microstructure, mechanical, and corrosion properties has received a lot of attention in the literature, but there have been few studies on the combination of process and design parameter optimization related to 17-4 PH SS. By appropriately tailoring SLM processing and design parameters, the microstructure, mechanical and corrosion properties of 17-4 PH SS can be improved. Scan strategy is one of the most critical design parameters influencing microstructure, mechanical, and corrosion properties. Similarly, residual stress generation and corrosion behavior in additive manufactured parts under the impact of process and design parameters has received scant attention.

In addition to that, Most of the studies are related to the meander/strip and rectangular strategies but there are few studies dealing with effect of hexagonal strategy on the microstructure and mechanical properties of 17-4 PH SS made by SLM. There are no studies on the comparison of the effect of different strategies on the microstructure and mechanical properties of 17-4 PH SS SLM. Moreover, the effect of scan strategy on residual stresses and corrosion behavior of SLM made components has received scant attention.

However, studies focusing on the influence of island size on the microstructure and mechanical properties of 17-4 PH SS alloy have been absent. Moreover, the optimal hexagonal island scanning strategy parameters for L-PBF processed 17-4 PH SS alloy are unknown. Thus, it is important to investigate the effect of island size on the microstructure, residual stress, and properties of L-PBF-processed 17-4 PH SS alloys, as this would help process optimization and engineering applications. Various hexagonal island sizes ranging from 1.2 mm to 10 mm were used to fabricate 17-4 PH SS specimens in this research to understand the effect of hexagonal island size on densification, microstructure, mechanical properties, and residual stresses.

Morever,there has been a lot of research on the effect of scan strategies, process parameters, and heat treatment on the microstructure and mechanical properties. There have been limited studies reported on the damping behavior of L-PBF-made components made with other materials [51], [52]. However, there have been few studies on the effect of heat treatment on damping behavior and correlating that with microstructure.

2.6. Gaps identified from the literature

Most of the studies are related to the effect of microstructure and mechanical properties on the strip and rectangular scan strategies and influence of process parameters but there is scant attention paid to influence of hexagonal scan strategy on the microstructure and mechanical properties. Similarly, the effect of scan strategies on microstructure, mechanical and corrosion properties has received limited attention. The effect of heat treatment on the microstructure, mechanical properties, fatigue crack growth and damping capacity received low attention. Along with this, the following literature gaps also have been identified based on the overall literature survey

1. There is limited literature on the combination of process and design parameter optimization related to 17-4 PH SS
2. Effect on mechanical properties has to be deeply studied for 17-4 PH SS SLM, especially for Hexagonal and checkerboard/Rectangular scan strategy
3. The effect of island size of Hexagonal scan strategy has to be deeply studied on the mechanical properties, and Corrosion Behavior for 17-4 PH SS SLM
4. There is limited research work done on effect of heat treatment on the corrosion, residual stress and correlation with mechanical properties on 17-4 PH SS
5. The effect of heat treatment on the damping behavior and fatigue crack growth rate and correlation with mechanical properties on 17-4 PH SS

2.7. Objectives framed

Based on the literature survey, the following objectives were framed

1. Effect of process parameters and scan strategy on microstructure, mechanical properties, corrosion and wear behavior of as built 17-4 PH SS samples made by SLM
2. Effect of scan strategy on microstructure, mechanical properties, corrosion and wear behavior of as-built 17-4 PH SS samples made by SLM
3. Influence of hexagonal scanning strategy island size on the microstructure, microhardness, residual stress, corrosion and wear behavior of as-built 17-4 PH SS samples made by SLM

4. Effect of heat treatment on the microstructure, mechanical properties, fatigue crack growth and damping capacity of 17-4 PH SS samples made by SLM

2.8 Research Plan

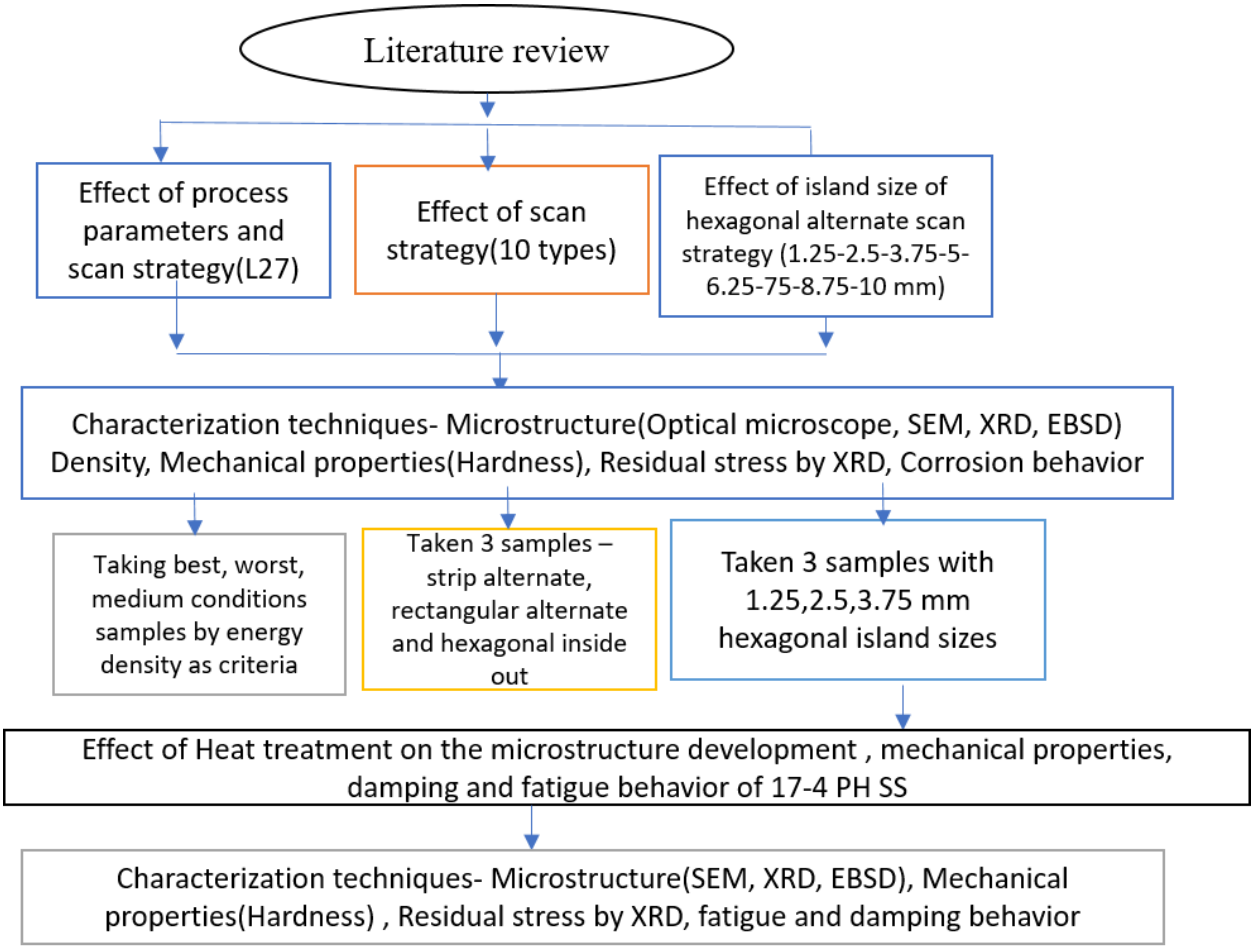

Fig. 2.10. Flowchart of entire thesis

CHAPTER 3
MATERIALS AND METHODS

3.1 Materials

The material used for the investigation was 17-4 PH SS. The morphology of gas atomized 17-4 PH SS powder morphology was observed using a scanning electron microscope, as shown in Fig. 3.1. The powder particle size was measured using Image J analysis from the SEM image and the particle size was around 10-45 µm. The chemical composition of the powder was calculated using EDAX analysis as listed in Table 3.1. 17-4 PH SS Samples were fabricated using DMP Flex 100 machine. A wavelength of 1060nm and a 100W fiber laser was used for the investigation. The SLM process was conducted under an argon atmosphere with an oxygen content of less than 50 PPM and the argon gas flow rate was maintained at 35 liters/ minute.

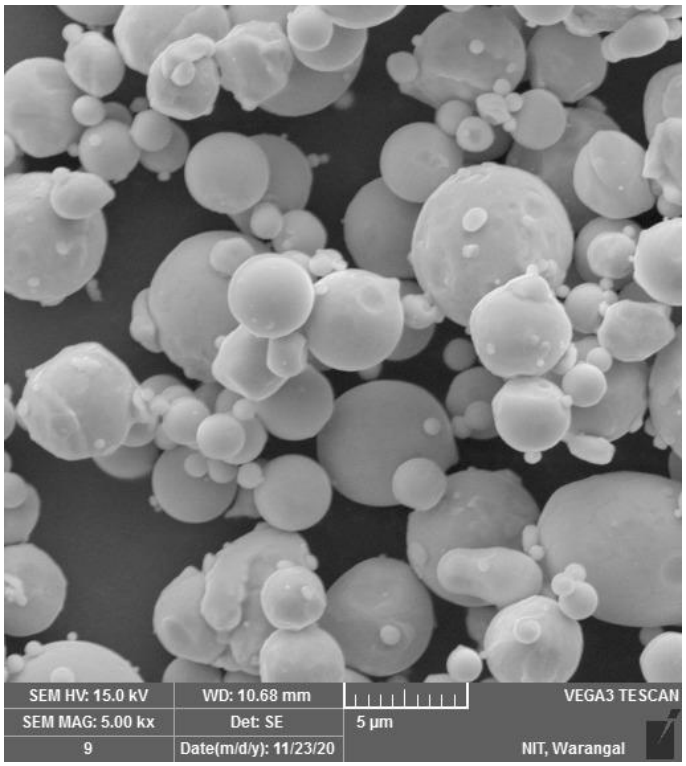

Fig. 3.1. SEM image of 17-4PH SS powder used in SLM deposition

Table 3.1: Chemical Composition of 17-4 PH SS Powder

Chemical Composition	**Fe**	**Cr**	**Ni**	**Cu**	**C**	**Mn**	**Si**
Weight%	66.59	16.95	4.11	4.27	3.97	0.895	0.845

SS 304 is used as the substrate material in sandblasted conditions to improve laser absorption. Prior to experiments, the substrate was cleaned with acetone to remove the impurities on the substrate surface.

3.2 Methods

In this experiment, 17-4 PH SS samples was deposited using the L-PBF technique shown in Fig. 3.2. The system consists of a roller and glove box in addition to a 1 KW continuous wave fibre laser. A powder supply bin, sintering piston, where the build plate must be attached, and nitrogen used as an inert gas in the process chamber. In order to conduct the experiments, a constant standoff distance of 10 mm and a laser spot diameter of 80 µm were used. Powder and laser were fed onto the sintering piston (build plate) to the point of deposition. The laser head moves in X and Y directions, and the sintering piston moves in Z direction to deposit one layer on top of the other. For bulk materials, stripe, rectangular, and hexagonal scanning strategies were used.

Fig. 3.2 .Schematic of L-PBF system deployed for the experiments

Laser power, scanning speed, and scanning strategy are the most important L-PBF process parameters. The laser spot diameter was maintained constant throughout the investigation since altering it would require modifying the experimental apparatus. Initially trial experiments were conducted by varying the laser power from 60W to 100W, scan speeds from 600 mm/sec and hatch distance between 40-50 µm. For bulk deposition, the process parameters that produce continuous deposits with a minimal amount of defects and hardness were used. 27 Cubical blocks of 17-4 PH SS with 10×10×10 mm^3 size were fabricated using Taguchi L_{27} (3^{13}) full factorial design for the experiments. Nine batches of cubical blocks with different energy densities but same layer thickness of 0.03 mm, hatch distance of 45 µm were used for the present research work. Each batch contained three samples designed with the same laser power, energy density, scanning speed, and hatch distance, but with different scanning strategies such as strip alternate, rectangular alternate, and hexagonal inside-out on SS 304 substrate. Based on the machine parameters range, laser powers of 80, 90, and 100 W, scan speeds of 960,1200, and 1440 mm/s were selected, as shown in Table 3.2**.** An overlap of 90 µm between two islands was kept for all three scan strategies, and an island size of 2500 µm was kept for rectangular alternate and hexagonal inside-out

strategies. The samples were deposited with a starting scan angle of 315^{o} and a scan rotation angle of 90^{o} between two layers to build a 10 mm cube of 333 layers.

Table 3.2: Different combination s of L-PBF process parameters and its corresponding energy density

Sample no.	**Laser power (W)**	**Scan speed (mm/s)**	**Scan strategy(*)**	**Energy density (J/mm^3)**
01	80	960	S	61.72
02	80	960	R	61.72
03	80	960	H	61.72
04	80	1200	S	49.38
05	80	1200	R	49.38
06	80	1200	H	49.38
07	80	1440	S	41.15
08	80	1440	R	41.15
09	80	1440	H	41.15
10	90	960	S	69.44
11	90	960	R	69.44
12	90	960	H	69.44
13	90	1200	S	55.55
14	90	1200	R	55.55
15	90	1200	H	55.55
16	90	1440	S	46.29
17	90	1440	R	46.29
18	90	1440	H	46.29
19	100	960	S	77.16
20	100	960	R	77.16
21	100	960	H	77.16
22	100	1200	S	61.72
23	100	1200	R	61.72
24	100	1200	H	61.72
25	100	1440	S	51.44
26	100	1440	R	51.44
27	100	1440	H	51.44

*S:Strip alternate ,R: Rectangular alternate and H:Hexagonal inside out scan strategies

For investigating the effect of scan strategy, the following parameters: laser power of 100 W, the scan speed of 1200 mm/sec, hatch distance of 45 microns, and a layer thickness of 30 microns were used for carrying out the study.

Moreover, to investigate the effect of island size on L-PBF Processed 17-4 PH SS, different hexagon island sizes of 1.25, 2.5, 3.75, 5, 6.25, 7.5, 8.75, and 10 mm were deposited using an L-PBF machine with dimensions 10×10×10 mm^3.

Similarly, for investigating the impact of heat treatment, the as built samples were deposited with process parameters of laser power 100W, scan speed of 1200mm/sec, hatch distance of 45µm, scan rotation angle of 67°, layer thickness of 30µm and hexagonal inside-out scan strategy. Heat treatments for different samples (L-PBF make) were made in a muffle furnace at different temperatures and a constant argon gas flow rate of 5 L/min was maintained during the heat treatment process (Table 3.3).

Table 3.3. Heat treatment schedules

Sample condition	Temperature/Time/Type of cooling
As built (AB)	-
Solution Annealing (SA)	AB/1038°C/30 min/AC
Aging (H 900)	SA/483°C/4 hour/AC
Over aging (H 1150)	SA/621°C/4 hour/AC
MOD H900 (SA)	SA/525°C/4 hour/AC
MOD H900 (AB)	AB/525°C/4 hour/AC

3.3.Characterization

Cubical block density was determined by Archimedes principle and then the blocks were sectioned to determine microstructure and micro hardness. The sectioned specimens were polished and then etched with Marbles reagent for both optical and scanning electron microscope examination. Panalytical XRD was used to carry out phase analysis. X-ray diffraction (XRD) was carried out from 20 - 120° at a scan step size of 0.016°. Scherrer formula (refer equation to 3.1) was used for calculating crystallite size for L-PBF samples in as-built and heat-treated samples.

$$d = \frac{C.\lambda}{\beta.cos\theta} \qquad 3.1$$

Where, C is Scherrer constant (0.9), λ is wavelength of X-ray source, β is full width half maximum (FWHM) in radians, θ is peak position in radians. Ten readings were taken for each sample in transverse and longitudinal direction while measuring micro hardness. Electrolytic etching was used to calculate grain size and grain orientation using EBSD analysis. Residual stresses were determined using X-ray dispersive $Sin^2\psi$ method using 2-theta scan remained at 65 degrees.

Electrochemical tests were performed with various process parameters. With the use of emery paper and silica suspension, the specimens' surfaces were polished. . The specimen's exposed surface area was around one cm^2 and the solution employed was a 3.5% by weight NaCl solution. Prior to doing the experiment, the densities of all the samples were measured. At room temperature, the electrochemical experiment was conducted. For this study, a standard three-electrode cell arrangement comprising a working electrode of a 17-4 PH SS specimen, a counter electrode of platinum foil, and a reference electrode of Ag/AgCl was used. The samples were in contact with the solution to achieve a steady OCP value, and the frequency was changed from 10^{-2} to 10^5 Hz while the amplitude was maintained at 10 mV. With a scan rate of 1mV, the potentiodynamic polarisation test was conducted between a range of -0.5mV and +0.5 mV. The experimental setup is shown in Fig. 3.3.

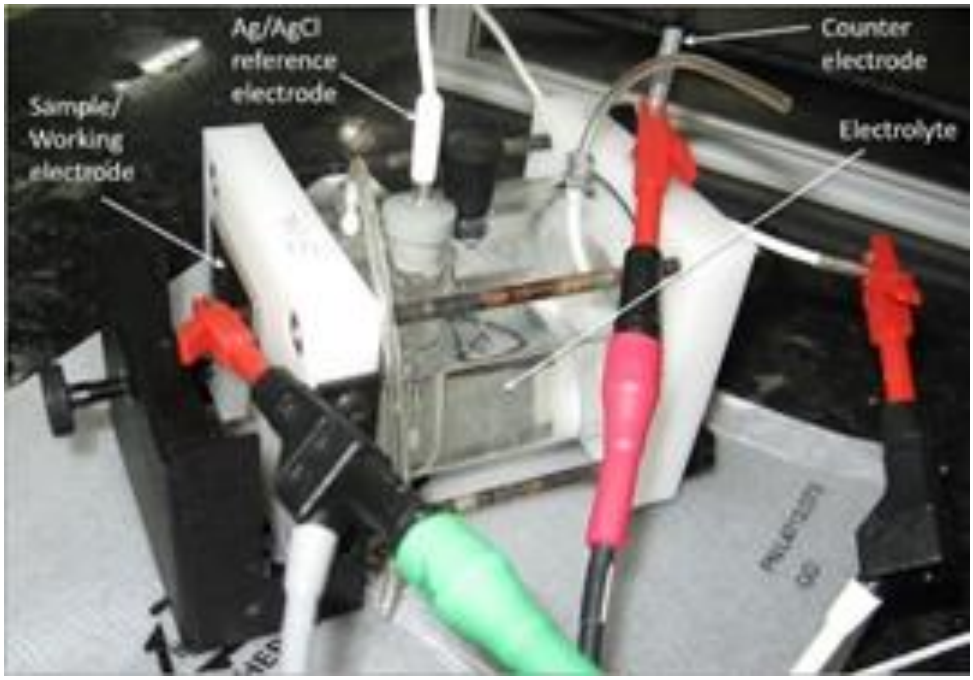

Fig. 3.3 Electrochemical setup for corrosion test

The frequency-dependent and temperature-dependent damping tests were done on the Metavib dynamic mechanical analyzer (DMA) at ambient temperature while varying the frequency from 1-10Hz and at 1 Hz by varying temperature from room temperature to 450 °C. The testing mode was 3-point bending test at a constant strain amplitude of 1×10^{-6} and at a load of 100 N.

Fig. 3.4. Damping setup for measuring damping capacity

Compact tension specimens were prepared using L-PBF which undergone various heat treatments. The fatigue crack growth rate testing was done using UT-04-0100 MEDIAN-100 machine with a load ratio of 0.1 and frequency of 15 Hz respectively. The crack propagation rate was measured using COD (Crack propagation displacement) gauge. SEM was used to observe the fractured surfaces

Fig. 3.5. Fatigue testing setup to measure fatigue crack growth rate

3.4. Summary

Material and characterization tools used for the experimental work were discussed in detail. A series of trial experiments were conducted to finalize the range of process parameters used for depositing samples as shown in Table 3.2. The Schematic representation of experimental setup and the range of parameters were discussed before discussing results section.

CHAPTER 4

Parametric investigation and characterization of 17-4 PH SS parts fabricated by selective laser melting

4.1. Introduction

The literature review demonstrates the significance of parametric analysis in determining the process parameters for bulk sample deposition without porosity and cracks for any material during LAM. Controlling the geometry of LAM-built structures also requires careful consideration of process parameter selection. Using two combined L-PBF parameters—process parameters (laser power and scan speed) and design parameter (scan strategy)—parametric investigation was carried out in this chapter to determine the range of ideal process parameter combinations based on the relative density and hardness. In addition, corrosion studies were performed at different combination of process and design parameters.

4.2. Process parametric Investigation

4.2.1. Relative Density

The relative densities of samples using various energy densities, scan speed, and scan strategies are shown in Table 4.1. It was found that the relative density values were found to be greater than 95% for all the samples. The relative density of the samples with medium energy density was found to be higher than for samples with low and high energy densities. The relative density of the samples increased with an increase in laser power keeping all other parameters constant though it was maximum for medium scan speed. The relative density variation for all 27 experiments with different scan strategies is shown in Fig. 4.1. (a-c).

Table 4.1: Average density and average hardness of all the samples

Sample no.	Laser power (W)	Scan speed (mm/s)	Scan Strategy(*)	Energy density (J/mm^3)	Density (gm/cc)	Transverse hardness (VHN)	Longitudinal hardness (VHN)
01	80	960	S	61.72	97.1±0.2	305±5	300±5
02	80	960	R	61.72	97.4±0.2	308±5	304±5
03	80	960	H	61.72	97.8±0.1	310±3	307±3
04	80	1200	S	49.38	97.1±0.2	308±5	306±5
05	80	1200	R	49.38	97.5±0.2	312±5	310±3
06	80	1200	H	49.38	97.9±0.2	315±3	314±5
07	80	1440	S	41.15	95±0.15	225±5	244±5
08	80	1440	R	41.15	95.2±0.2	245±5	250±3
09	80	1440	H	41.15	95.8±0.2	256±5	259±5
10	90	960	S	69.44	97±0.14	285±5	292±3
11	90	960	R	69.44	98±0.2	290±3	298±5
12	90	960	H	69.44	98.3±0.1	305±5	305±5
13	90	1200	S	55.55	98±0.2	310±5	310±5
14	90	1200	R	55.55	98.3±0.2	318±3	315±4
15	90	1200	H	55.55	98.5±0.1	325±3	321±5
16	90	1440	S	46.29	96.7±0.2	255±3	272±5
17	90	1440	R	46.29	96.9±0.2	265±5	280±5
18	90	1440	H	46.29	97.2±0.2	274±5	289±3
19	100	960	S	77.16	97.4±0.2	280±3	285±5
20	100	960	R	77.16	97.5±0.15	285±5	290±4
21	100	960	H	77.16	97.8±0.2	291±5	295±5
22	100	1200	S	61.72	98.2±0.2	315±3	320±3
23	100	1200	R	61.72	98.7±0.1	330±5	330±5
24	100	1200	H	61.72	99.2±0.1	352±3	352±3
25	100	1440	S	51.44	96.8±0.1	265±5	283±5
26	100	1440	R	51.44	97.2±0.2	272±3	288±3
27	100	1440	H	51.44	97.5±0.2	279±5	292±5

*S: Strip alternate,R: Rectangular alternate and H:Hexagonal inside out scan strategies

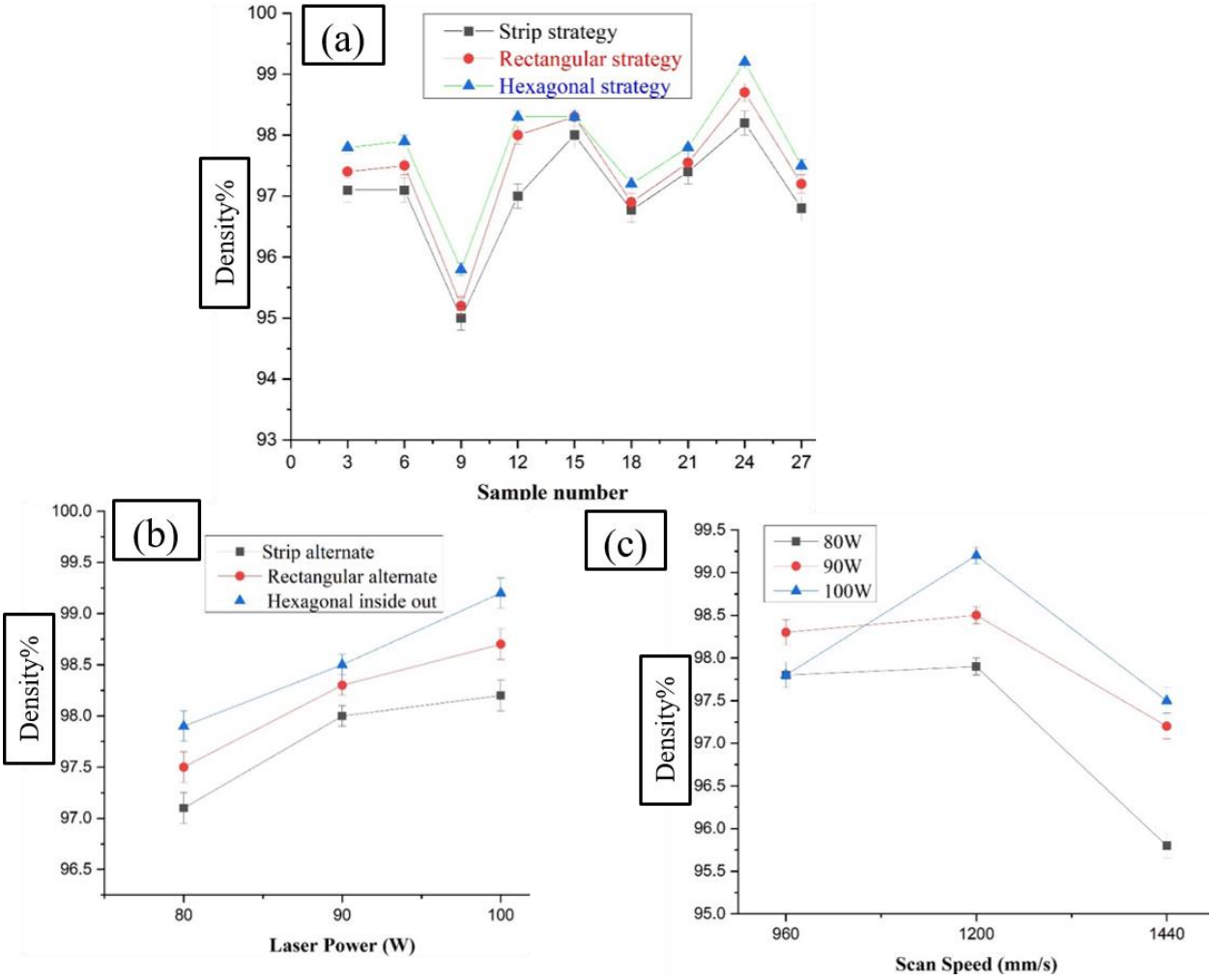

Fig. 4.1. Variation of density for (a) Different strategies, (b) Different laser powers, and (c) Different scan speeds

It was found to be higher for Sample 24 with a medium energy density of 61.72 J/mm^3 and lower for Sample no 7 with an energy density of 41.15 J/mm^{3,} as shown in Fig. 4.1.(a). Sample 24 built with medium energy density was 3.73% and 1.41% denser than Sample 9 with low energy density and Sample 21 with high energy density, as shown in Fig. 4.1.(a). At lower and higher energy densities, balling defects occur, making the samples lose their relative density. The relative density was found to be optimal for Sample 24 with 100 W laser power, and it was 1.5% more than for Sample 6 at 80 W laser power sample and 0.65% more than Sample 15 at 90 W laser power, as shown in Fig. 4.1.(b). As the laser power increases, with other parameters constant, there is no balling effect, leading to an increase in relative density, as shown in Fig. 4.1.(b). Similarly, the relative density of Sample 24 with a medium scan speed of 1200 mm/s was found to be 1.4% and 1.8% higher than Sample 21 with a scan speed of 960 mm/s, and Sample 27 with a scan speed of

1440 mm/s, respectively,shown in Fig. 4.1.(c). When scan speed was lower, there was insufficient re-melting of the previous layer and, as a result, weak bonding of powder in the layer happened. The relative density was found to be higher for sample 24 fabricated uisng a hexagonal inside-out scan strategy. It was 0.6% and 0.4% more than for sample 22 with strip alternate strategy and sample 23 with rectangular alternate strategy because of the complete melting of the powder, as shown in Fig. 4.1.(a).

4.2.2. Micro hardness

The microhardness values of samples fabricated using various process and design parameters are shown in Table 4.1, and they are plotted in Fig. 4.2 &4.3. Samples fabricated using the hexagonal inside-out scanning strategy show higher microhardness than those fabricated using the strip alternate and rectangular alternate scanning strategies while keeping all other parameters constant. The samples fabricated with a medium scanning speed of 1200 mm/s, using hexagonal inside-out scan strategy, and medium energy density of 61.72 J/mm^3 resulted in highest microhardness compared to other samples in both longitudinal and transverse directions. The microhardness values are consistent with build direction for all the scanning strategies. But, there was a variation in transverse microhardness due to variation in molten pool size.

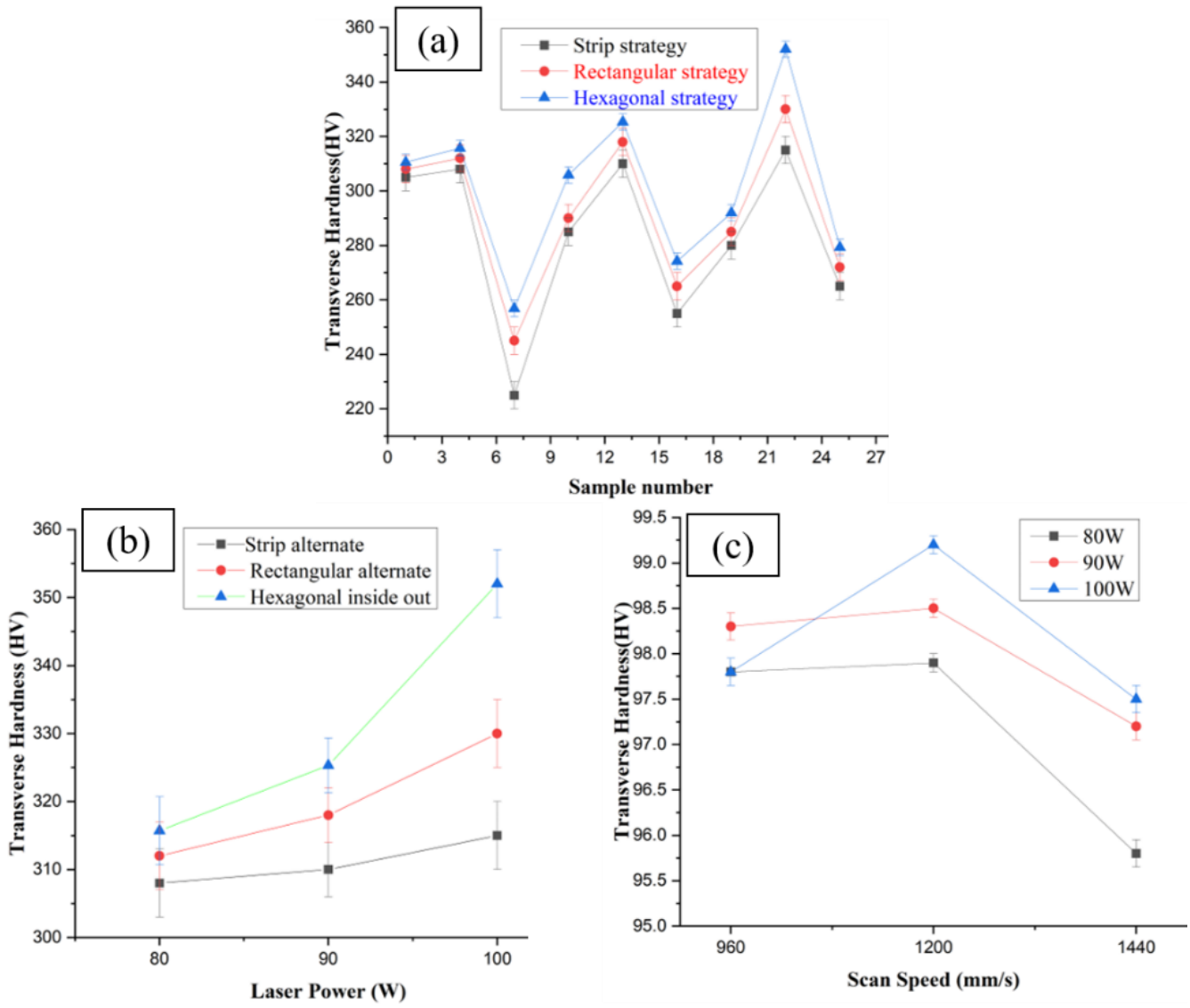

Fig. 4.2. Variation of transverse hardness for (a) different strategies, (b) different laser powers, and (c) different scan speeds

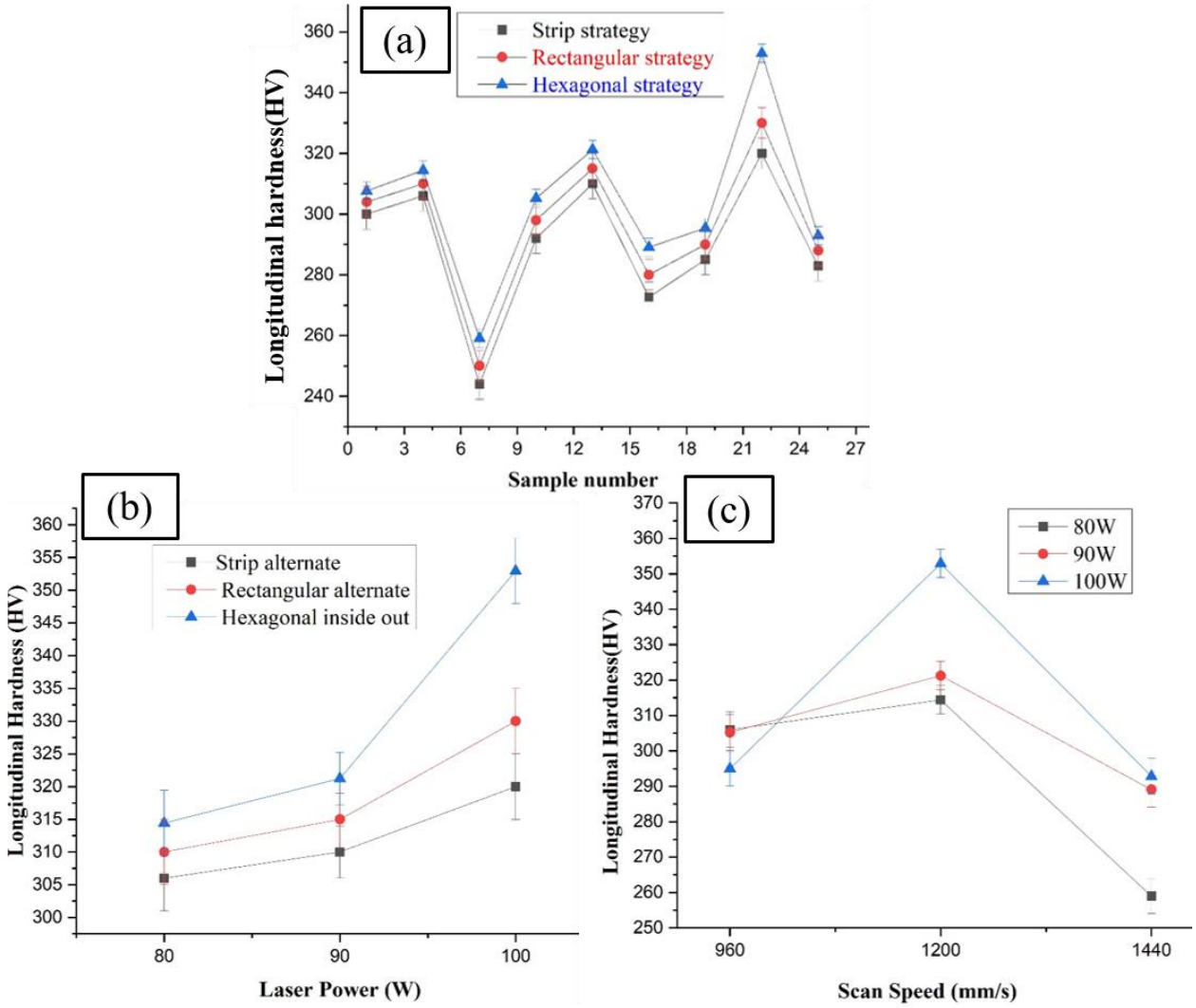

Fig. 4.3. Variation of longitudinal hardness for (a) different strategies, (b) different laser powers, and (c) different scan speeds

The average transverse and longitudinal hardness of sample 24 with medium energy density were found to be 27.2% more than that of sample 9 with low energy density and 17.32% higher than sample 21 with high energy density, as shown in Fig. 4.2. (a) & 4.3. (a). When energy density increased from low to medium value, hardness increased because of the complete melting of powder and fewer defects. The average transverse and longitudinal hardness of sample 24 with 100 W laser power was 10.5% more than that of sample 6 at 80 W laser power and 7.6 % more than that of sample 15 at 90 W laser power. As the laser power increases, complete melting of the powder and densification occurs, resulting in higher hardness, as shown in Fig. 4.2. (b) & 4.3.(b). The average transverse and longitudinal hardness for sample 24 at a scan speed of 1200 mm/s was 15.62% and 20.73% more than for sample 21 at a scan speed of 960 mm/s and sample 27 at a scan

speed of 1440 mm/s while all other parameters were constant as shown in Fig. 4.2. (c) & 4.3. (c). The medium scan velocity showed higher hardness as lower laser scanning results in slower cooling rate. But if the scan speed is very high, it does not melt the powder and leads to porosity. The hardness of sample 24 fabricated using the hexagonal inside-out scan strategy was 6.8% and 6.25% more than that of samples processed with strip alternate and rectangular alternate scan strategies, respectively, while keeping all other parameters constant (shown in Fig. 4.2. (a) & 4.3. (a)), because of higher densification. This is in line with findings of previous research [53]

4.3. Microstructure

The microstructure of all the samples with different energy densities, scan velocities, scan strategies, and laser power is shown in Fig. 4.4. The microstructure of all samples contains large fine grains at the melt pool boundary and columnar grains in the matrix along the laser beam direction. The optical microstructure images at an energy density of 41.15 J/mm^3 are shown in Fig. 4.4 (b-d). The microstructure images of three different scan strategies at a medium energy density of 61.72 J/mm^3 are shown in Fig. 4.4 (g-i). The hardness and density of sample 22, sample 23, and sample 24 at an energy density of 61.72 j/mm^3 were higher than for samples 7, sample 8, and sample 9 at energy density 41.15 J/mm^3 because of smaller grain size, as shown in Fig. 4.4 (g-i). The presence of a more austenite phase (white color) is seen in Fig. 4.4 (g-i) compared to microstructure in Fig. 4.4 (b-d), which improves hardness values. As the energy density increases, the overlap between two layers increases as the previous layer melts, and the vertical distance between tracks increases, as shown in Fig. 4.4 (g-i). The optical microstructure of sample 6, sample15, and sample 24 fabricated through laser power of 80 W, 90 W, and 100 W, scan speed of 1200 mm/s, hatch distance of 45 µm, and subject to hexagonal inside out scan strategy is shown in Fig. 4.4 (a,e, i) The defects decreased as laser power increased due to the formation of smaller molten pools. The optical microscope images for sample 21, sample 24, and sample 27 with variation of scan speed from 960 to 1200 and 1440mm/s but with constant laser power of 100 W, and using hexagonal inside out scan strategy are shown in Fig. 4.4 (f, i, j) respectively. The lack of fusion porosity and incomplete melting of powder decreased, and then it increased in the samples with an increase in scan speed. The optical microscope images of samples with strategy variation are shown in Fig. 4.4 (f, i, j). When keeping other parameters constant, like laser power at 100 W and scan speed at 1200 mm/s, there was a slight variation of properties as there was not much change in molten pool size and phases between these samples, but the columnar dendrites

expanded in the direction of heat flow because of large surface area and high cooling rates. The hexagonal inside-out scan strategy contains columnar dendrites which expanded in the direction of heat flow due to large surface area and high cooling rate. Therefore, the hexagonal inside-out scan strategy exhibited better properties among all scan strategies due to fewer defects. The highest porosity was obtained for strip alternate scan strategy because of the disruption of molten pools between the layers as the layers rotate with a scanning angle of 90° between them. Defects like lack of fusion occur in the layers between or between melt pools in the build direction, while pores occur mainly in the melt pool interiors [54]. During the SLM phase, an overlap of 90 µm was kept between two hexagonal inside-out and rectangular alternate scan strategy islands, to reduce porosity that develops during the process. The grain morphology developed along the build-direction in the hexagon scanning pattern is cellular and irregular because of high cooling rate and large scan area. In vertically printed samples, there was no significant variance in weld pool geometry. It could be due to small cross-section of the laser in vertical samples and the presence of powder which results in cooling rate delay [55].

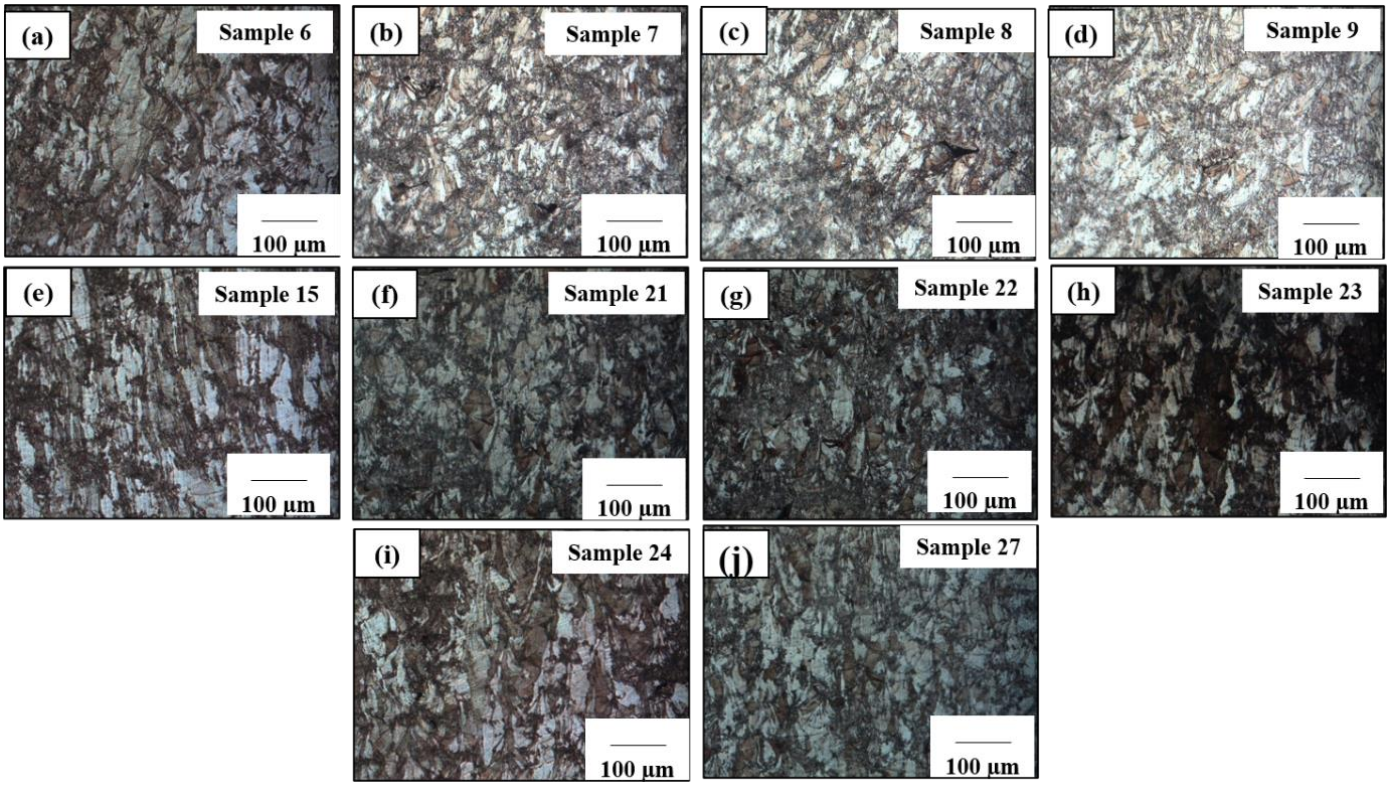

Fig. 4.4 Optical images of the samples ((a) sample 6-(b) sample 7-(c) sample 8-(d) sample 9-(e) sample 15- (f) sample 21- (g) sample 22-(h) sample 23- (i) sample 24-(j) sample 27)

4.4. Residual Stress

AM components show residual stress. Tensile residual stresses are prevalent in the surface region, while compressive residual stresses are expected in core volume [56]–[58]**.** The current study focuses mainly on the surface region. The residual stresses are measured on the top surface of each specimen along the build direction for samples with low and medium energy density generated using hexagonal inside-out scan strategy. The stress measurements were calculated using $\sin^2\psi$ method at three angles (0^o,90^o,135^o). The principal stresses were labeled σ_i (i=1,2,3), where σ_1 is the maximum principal stress while the other is orthogonal.

The residual stresses along both principal planes were same for both specimens. The residual stresses were calculated for each sample at the central location of each surface of the specimen. It was observed that residual stresses for the samples at medium energy density were lower than those with low energy density. A decrease in residual stresses with increased energy density and laser power was observed. The mean residual stress measured in sample 9 was 746 MPa, while the residual stresses in sample 24 was 476.0 MPa.

There was an overlap of 90 µm between two laser islands in all three types of strategies to prevent incomplete powder melting, and there was also connection between two laser tracks. But at low energy density, balling defect occurred, making the sample more brittle, leading to non-uniform deposition of powder in the previously deposited layers. This is the reason that led to high porosity and low density in low energy density sample compared to high energy density samples, resulting in high residual stresses.

4.5. Corrosion Studies

The weight loss tests of Sample 09, Sample 21, and Sample 24 with low, high, and medium energy densities were conducted by immersing them in electrolytic solution for 20 days. The results are tabulated in Table 4.2. The corrosion rate was calculated using weight loss method through the following formula (equation 4.1)

$$CR = \frac{534W}{DT} \ldots\ldots\ldots eq\ 4.1$$

where W is weight loss(g/cm^2), D is density(g/cm^3)and T-time of exposure in hours

Table 4.2. Results of weight loss test

Sample no	Weight loss(g/cm^2)	Density(g/cm^3)	Corrosion rate(mpy)	E_{corr} (V)
09	0.00016	7.63	2.33×10^{-5}	-0.210
21	0.000044	7.78	6.29×10^{-6}	-0.163
24	0.000043	7.8	6.14×10^{-6}	-0.132

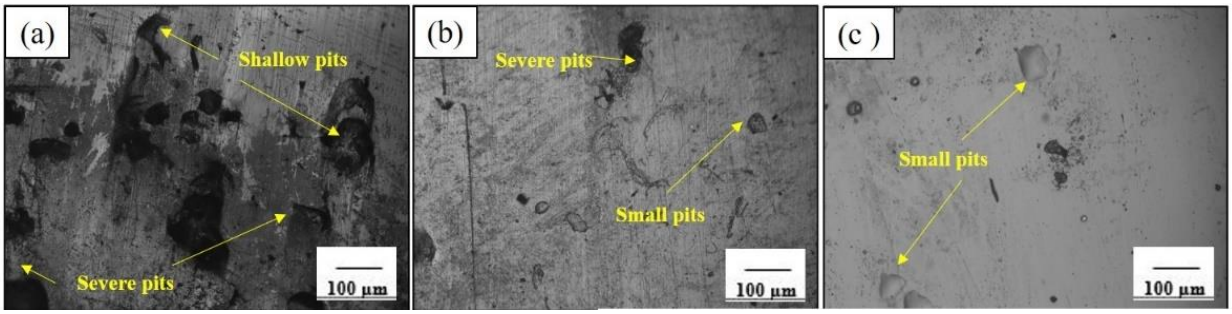

Fig. 4.5.Optical micrographs of samples after doing weight loss tests for energy densities of (a)41.15 J/mm^3,(b)77.16 J/mm^3, and (c)61.72J/mm^3

From **Table 4.2**, it was identified that weight loss and corrosion rate decreased for medium energy density sample compared to low and high energy densities samples. The defects and porosities affecting corrosion rate were eliminated as the energy density increased from low to medium. These defects increased as the energy density increased (as shown in Fig. 4.4.a-c). So the defects and porosity present in the lower and higher energy density samples act as passivation pitting potential sites in the samples. A similar observation was also reported by wang et al [29]**.**

4.6. Summary

The process parameters identified for the samples with the highest relative density and hardness are parameters that have a medium energy density of 61.72 J/mm^3, high laser power of 100W, medium scan speed of 1200 mm/s, and employ hexagonal scan strategy. The microstructure contains ɣ austenite and α-ferrite phases. The microstructure of all samples contains large fine grains at the melt pool boundary and columnar grains in the matrix along the laser beam direction. The columnar grain boundaries in the vicinity of molten pools were directed towards the top surface of the sample. The proportion of columnar grains decreased at medium energy density,

with a corresponding increase of fine grains compared to samples with low energy density. The residual stresses were lower for medium energy density samples compared to low energy density samples. The corrosion rate was found to be less than 0.5 mpy at the time of performing weight loss tests; pitting resistance was exceptional with stable pits and free from corrosion cracks. The corrosion resistance was higher for medium energy density and hexagonal inside-out scan strategy samples because of lower defects and higher density.

CHAPTER 5

Influence of scanning strategies on microstructure, residual stress, and corrosion behavior of 17-4 PH SS fabricated by selective laser melting

5.1 Introduction

By comparing the relative density and micro hardness, the various process parameter combinations are identified in the preceding chapter. Then, 17-4 PH SS samples were deposited using several scan strategies, including strip alternate, rectangular alternate, and hexagonal inside out, with a laser power of 100W and a scan speed of 1200 mm/sec. This chapter examines the microstructure, hardness, and corrosion behaviour of L-PBF 17-4 PH SS samples using various scanning strategies.

5.2. Transverse and Longitudinal Hardness

The variation of hardness is depicted in Table 5.1 and 5.2. Both transverse and longitudinal hardness values were calculated for all the samples of different scan strategies. In the strip and rectangular scan strategies, including all types of strategies,i.e. samples with a horizontal, vertical, and alternate types of strategy exhibited more hardness compared to samples with both direction type strategies because low energy was supplied in each layer compared to both type strategy. It resulted in a less dense sample as more amount of powder melted in case of both type strategy compared to horizontal, vertical, and alternate types of strategies. As more energy was input in the case of both type of scan strategy balling defect occurred because of large surface tension which was unable to wet the molten metal with the previous layers. The alternating molten pool in an alternate type of strategy results in greater fusion of powder particles and higher bonding of powder particles which results in better properties compared to horizontal and vertical type of scan strategies. The hexagonal inside out scan strategy showed a lower thermal gradient and lower absorption of energy compared to strip alternate and rectangular alternate scan strategies. It resulted in lower defects and pores compared to other two types of scan strategies and led to higher hardness. Similarly, all types of strip scan strategies exhibited a large thermal gradient and high absorption of energy which led to slow cooling rate and lower hardness compared to all types of rectangular scan strategies, and this was reported by other

researchers too [59]. The hexagonal inside out strategy has high hardness compared to the hexagonal outside in strategy because of higher cooling rate as the scan track starts with contour and ends again at outside for hexagonal inside out strategy. The hardness of wrought 17-4 PH SS was lower the hardness of other scan strategy samples because of faster cooling rates in AM samples, resulting in fine grain size and better mechanical properties.(Table 5.2)

Table 5.1. Average hardness values for all scan strategy samples and wrought alloy

Sample no	Scan strategy	Transverse Hardness (VHN)	Longitudinal Hardness (VHN)
1	Stripe Horizontal	258±5	263±5
2	Stripe Vertical	264.55±4	269.55±5
3	Stripe Alternate	321.24±3	326.24±4
4	Stripe Both	196.45±5	201.45±5
5	Rectangular Horizontal	308±3	313±3
6	Rectangular Vertical	309.36±5	314.36±5
7	Rectangular Alternate	388±4	393±4
8	Rectangular Both	245±5	250±3
9	Hexagonal Inside out	390±3	395±3
10	Hexagonal Outside in	353.28±5	353.28±5

Table 5.2. Average hardness values for wrought alloy

Sample no	Scan strategy	Transverse Hardness (VHN)	Longitudinal Hardness (VHN)
1	Wrought alloy	195±5	200±5

5.3. Microstructure

The side surface with different molten pools of all samples with different types of scan strategies and molten pool boundaries is shown in Fig. 5.1. (a-k). Molten pool region exhibited regular wise patterns for rectangular alternate and both hexagonal scan strategies. Columnar grains were

observed at all strip and rectangular scan strategies except in rectangular alternate strategy as shown in Fig. 5.1. (a-k). Because of the larger thermal gradient compared to rectangular alternate and hexagonal type scan strategies. The wrought alloy contains Δ ferrite stringers known as dark streaks as shown in Fig. 5.1.k. There are fine precipitates present in the SLM samples compared to wrought alloy which resulted in better hardness and density for SLM samples compared to wrought 17-4 PH SS alloy.

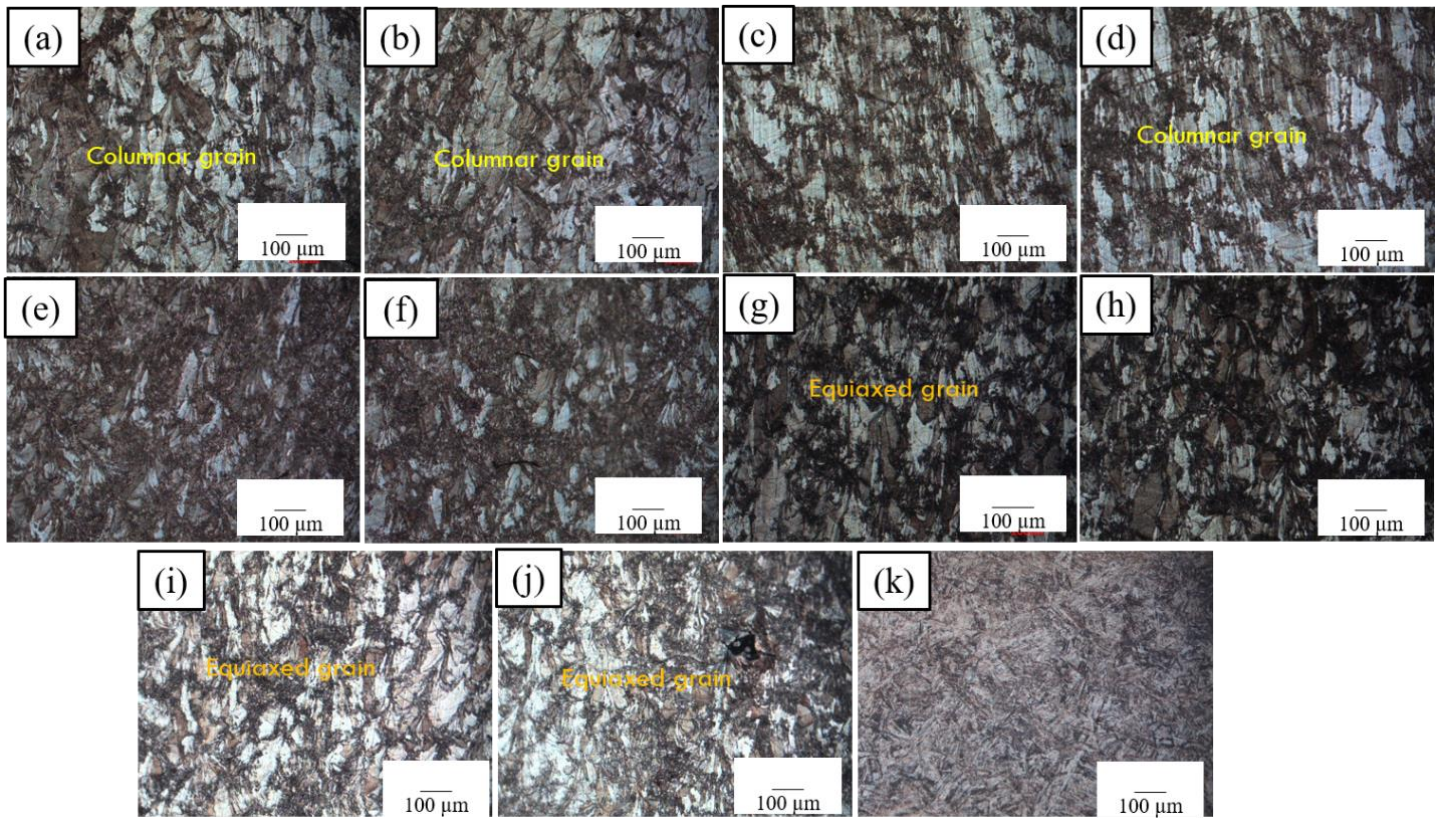

Fig. 5.1. The microstructure of side surface for scan strategy of a)strip horizontal b)strip vertical c)strip alternated)strip both e)rectangular horizontal f) rectangular vertical g) rectangular alternate h) rectangular both i)hexagonal inside out j)hexagonal outside in, and k)wrought alloy

5.4. Residual stress

The residual stresses were measured on the top surface of each specimen along the build direction for samples with different scan strategies. The stress measurements were calculated using $\sin^2\psi$ method at three angles (0,90,135). The main stresses were labeled σ_i (i=1,2,3) where σ_1 is maximum principal stress where other stresses are orthogonal to each other. The residual stresses along both

the principal planes were the same for both specimens. The residual stresses for hexagonal inside-out sample was lower than for all other samples with different types of scan strategies. The residual stresses were higher for strip-type sample among all types of scan strategies as shown in Fig. 5.2.

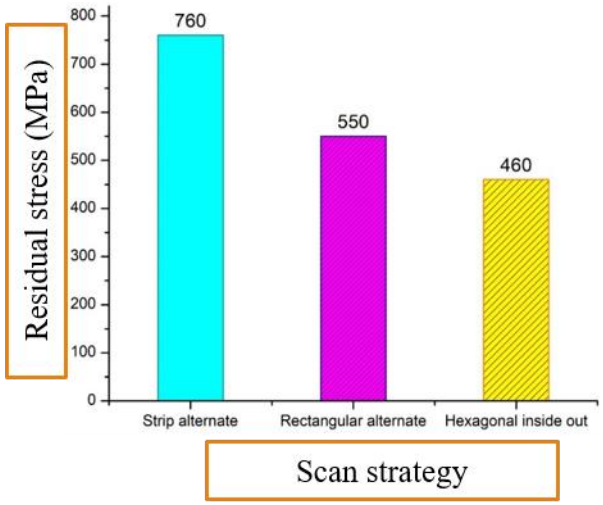

Fig. 5.2. Variation of residual stresses for a) strip alternate, b) rectangular alternate, and c) hexagonal inside out samples

The mean residual stresses decreases as we go from strip alternate strategy to rectangular alternate strategy and then hexagonal inside out strategy. An overlap of 90 microns was kept between two laser tracks for all scan strategies which enables complete melting of the powder. But the balling defect and large thermal gradient in the strip alternate sample make the sample fail to bond with the substrate and non-uniform deposition of powder over previous layers occurred. This makes the strip alternate sample to be more porous and less dense, which results in higher residual stresses and this has been confirmed by other researchers [43].

Residual stresses increased with a long scanning track, and weak preheating effect and at high thermal gradient. Repeated heating and laser rescanning of previous overlap regions at different island borders acts as a stress release zone [60]. The island laser scanning strategy was found to be one of the most effective ways to reduce residual stress. As there were no islands in the strip alternate strategy, there were no stress release zones while rectangular and hexagonal strategies showed stress release zones which resulted in lower thermal residual stresses for the two strategies. The thermal gradient of the rectangular alternate strategy was higher compared to hexagonal inside out, which

resulted in high residual stresses. So, the ranking of the samples with increasing residual stresses was strip alternate >rectangular alternate > hexagonal inside out strategy.

5.5. Corrosion studies

Open-circuit potential tests were done for all the samples for 600 minutes, and OCP values were observed in Fig. 5.3-a. The open-circuit potential values of decreasing order for hexagonal inside out scan strategy sample (-0.17V)> Rectangular alternate sample (-0.25V)> Strip alternate scan strategy sample (-0.32V). The tendency to form passivating film was higher for hexagonal inside-out scan strategy sample than other two samples. Corrosion potential at OCP is a measure of the tendency to form passivating film, and when corrosion potential at OCP is higher, corrosion resistance is higher. The tendency to form passivating film is higher for hexagonal inside out scan strategy sample compared to other two samples with rectangular alternate and strip alternate strategies. Potentiodynamic polarization tests were performed for samples with strip alternate, rectangular alternate, and hexagonal inside out scan strategies after obtaining a steady-state by doing an OCP test for 600 minutes. Tafel curves are data fitting curves obtained after doing potentiodynamic polarization tests. The samples at three different scan strategies tend to passivate more than OCP, but the passivating was faster, and a smoother polarization curve was obtained for hexagonal inside-out scan strategy sample compared to the sample with strip alternate and rectangular alternate scan strategies. The corrosion potential (E_{corr}) is obtained at the point where anodic and cathodic potentials meet in the Tafel plot. The corrosion potential (E_{corr}) of each sample is extracted from the Tafel curves in Fig. 5.3-b. The excellent corrosion resistance samples should have high E_{corr} (lowest negative value) and samples with low E_{corr} (highest negative value) corrodes faster than other samples. The corrosion potential values of samples with strip alternate and rectangular alternate scan strategies were lower compared to samples fabricated through hexagonal inside-out scan strategy. The volume fraction of defects and porosities also play an important role in corrosion resistance. As the porosity of sample with strip alternate is higher compared to hexagonal inside out and rectangular alternate scan strategies samples, the regions near the pores were more easily attacked and dissolved than the rest of the sample. The defects on the sample try to break the oxide film and lead to the accelerated dissolution of metal, as it is confirmed by other researchers [61]. So, the sample with hexagonal inside-out scan strategy, with the lowest porosity,

attained the highest corrosion resistance, and the sample with strip alternate scan strategy, with high porosity, attained high corrosion.

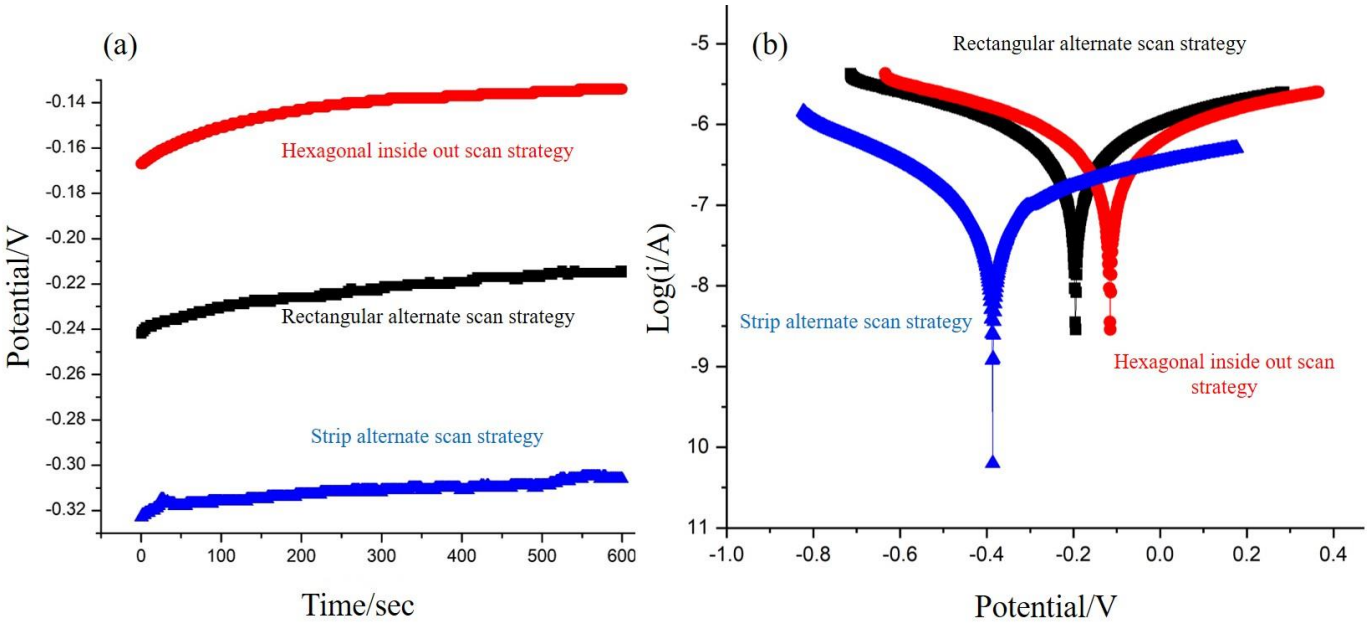

Fig. 5.3. Corrosion curves for samples with different scan strategies ((a) Open circuit potential values and (b) Tafel plots)

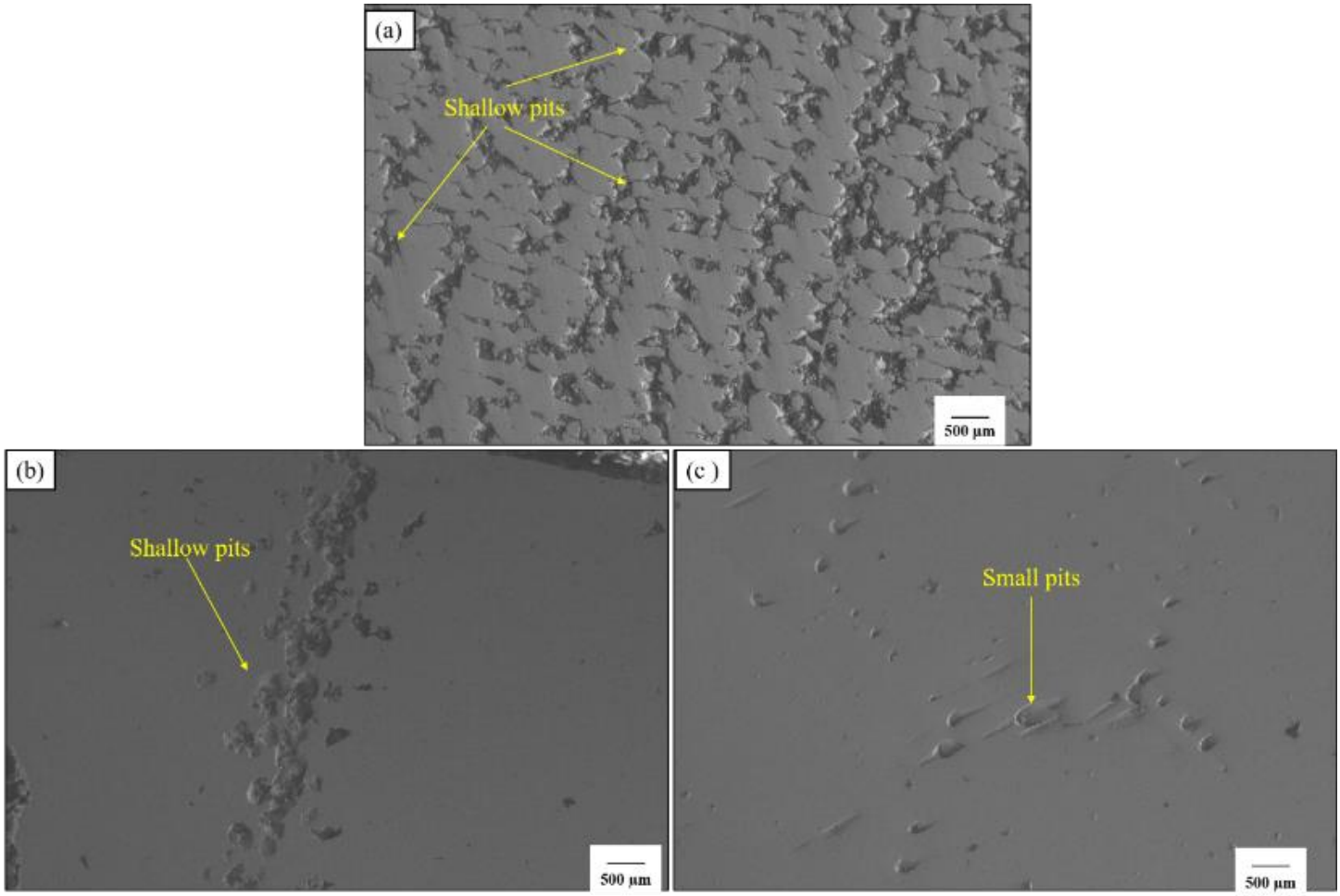

Fig. 5.4. SEM images of samples with scan strategy of (a) strip alternate, (b) rectangular alternate, and (c) hexagonal inside out

After the Tafel polarization test, the corroded samples were observed by using SEM (Fig. 5.4). Continuous corrosion activity resulted in the formation of pits. Large-sized pits were observed in samples with strip alternate, rectangular alternate strategies, and small-sized pits were observed in sample with hexagonal inside out scan strategy. The sample with hexagonal scan strategy exhibited highest corrosion resistance and it was due to hindrance of growth of pits and a smaller number of pit morphologies. But the number of pit morphologies observed was more for samples with strip alternate and rectangular alternate scan strategies, and there were no corrosion cracks evidenced in any of the samples, as shown in Supplementary Fig 5.4.The growth of pits was hindered by austenitic grains, as they exhibited better corrosion resistance than ferritic grains [62]. These results were also in line with the weight loss test results as discussed in the previous section.

5.6 Summary

The hardness of all scan strategy samples were higher than that of wrought alloy because of high cooling rates and finer grain size for SLM samples. Hexagonal inside-out scan strategy exhibited highest hardness among all scan strategy samples because of low thermal gradient and complete fusion of powder particles. Side surface microstructure contained small molten pools. Columnar grains were observed at horizontal, vertical and both types of scan strategies in all strip and rectangular scan strategies except in rectangular alternate strategy because of the large thermal gradient compared to rectangular alternate and hexagonal type scan strategies. The ranking of the samples with higher residual stresses were strip alternate >rectangular alternate >hexagonal inside out strategy because of long scanning track, weak preheating effect, and high thermal gradient in strip and rectangular scan strategies compared to hexagonal inside out scan strategy.The corrosion rate was found to be lower than 0.5 mpy based on weight loss tests, pitting resistance was exceptional with stable pits and the sample was free from corrosion cracks. The corrosion resistance was higher for hexagonal inside-out scan strategy samples because of lower defects

Chapter-6

Influence of hexagonal scanning strategy island size on microstructure, residual stress and corrosion behavior of 17-4 PH SS made by L-PBF

6.1 Introduction

In the previous chapter, microstructure characterisation, hardness and corrosion studies of L-PBF 17-4 PH SS bulk samples were carried out at different scanning strategies. Considering the high hardness of L-PBF 17-4 PH SS at a laser power of 100 W, scan speed of 1200 mm/sec and hexagonal inside out scan strategy was used for island size variation. In this chapter the influence of hexagonal island size on the Microstructure, hardness, corrosion behavior was determined at different island sizes.

6.2 Island size influence on scan time

The average time per layer for different hexagonal island sizes fabricated under L-PBF machine is given in Fig. 6.1. As the island scan size increases, the scanning time for the hexagonal island size samples decreased. The longest scanning time was observed for 1.25 mm hexagonal island scan size and it was around 4.6 sec which is almost 84% of the time for 10 mm island size. The scanning time for 10 mm hexagonal island size was around 2.5sec. As the size of the island decreased, the laser beam jump increased, which explains varying scanning times for islands of different sizes. If the overlap regions are more at smaller island sizes, the scanning length for smaller island sizes increases. So, island size did affect the scanning time of samples and led to higher processing efficiency in terms of time obtained for larger island sizes.

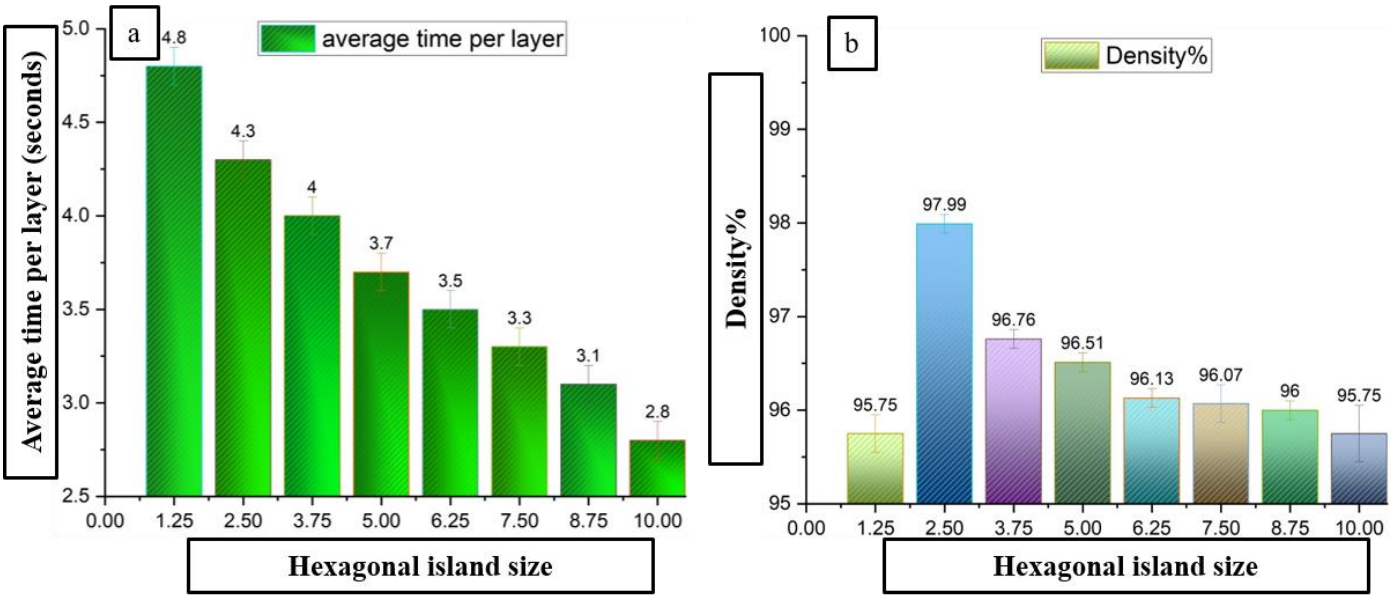

Fig. 6.1. (a)The averages scan time and (b) density variation with island size

6.3. Micro Hardness

The average hardness of all the samples was around 330-380 VHN in both longitudinal and transverse directions as shown in Fig. 6.2 (a-b). The hardness of the sample with hexagonal island size 2.5 mm was higher than all the samples with different island sizes as the molten pool was stable and irregular. The hardness of the sample with the lowest island size and largest island sizes was very low compared to the island with 2.5 mm size. The hardness varied with island size and higher hardness was exhibited due to fine grain size [13]**.** The hardness variation for the samples was due to variation in the percentage of austenite and ferrite, as shown in Fig. 6.2**.**

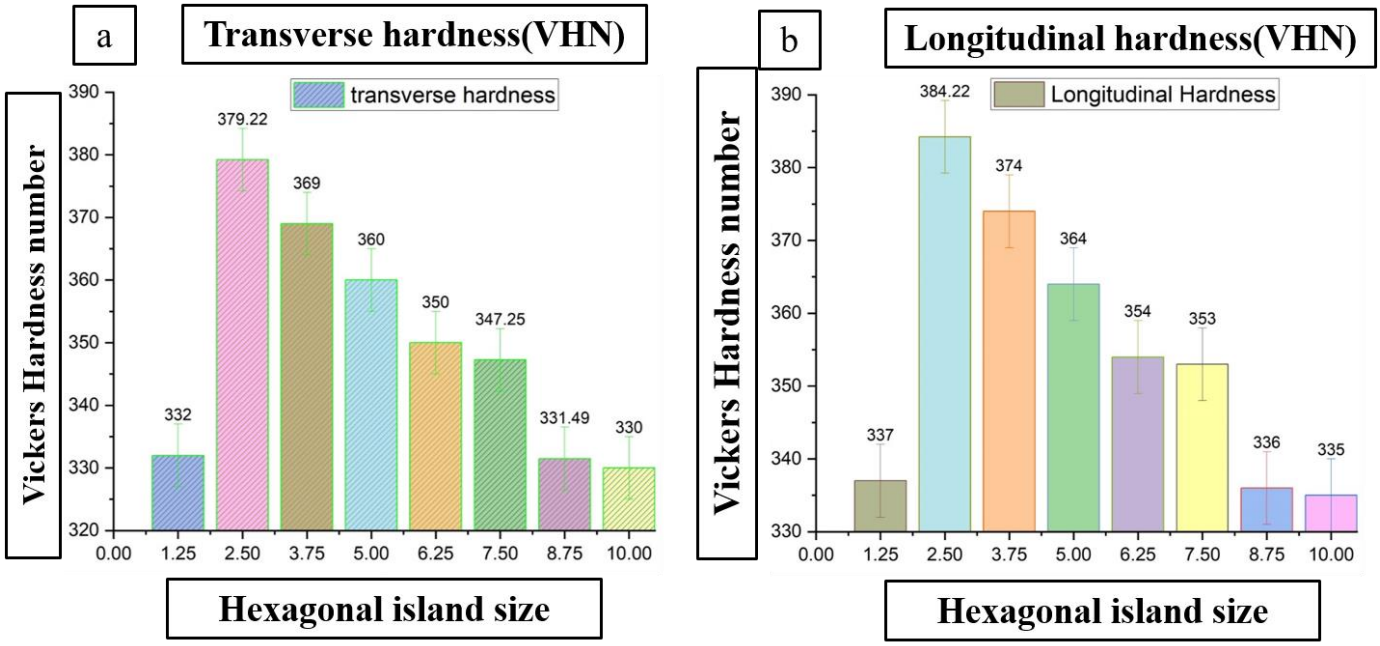

Fig. 6.2 Hardness variation with island size in a) Transverse Direction b) Longitudinal Direction

6.4. Microstructure

Molten pool boundaries of SEM images of all the island size samples fabricated by L-PBF are depicted in Fig.6.3 (a-c). Large columnar grains formed in the centre of the molten pool, and fine equiaxed grains formed along grain boundaries as a result of nucleating agents, respectively, in the two regions of the microstructure. Columnar grain formation in the centre of the molten pool was caused by thermal behaviour during solidification. The fine grain area of the medium island size samples was more compared to large island sizes and very small island sizes. The 17-4 PH SS alloy consists of Cu precipitates. As the island size increases from 1.25 to 2.5 mm, the percentage of carbon, silicon, chromium, nickel, and copper increases, resulting in improvement of mechanical properties: once this composition of chemical elements decreases as shown in Fig. 6.3, it results in the decrease of mechanical properties.

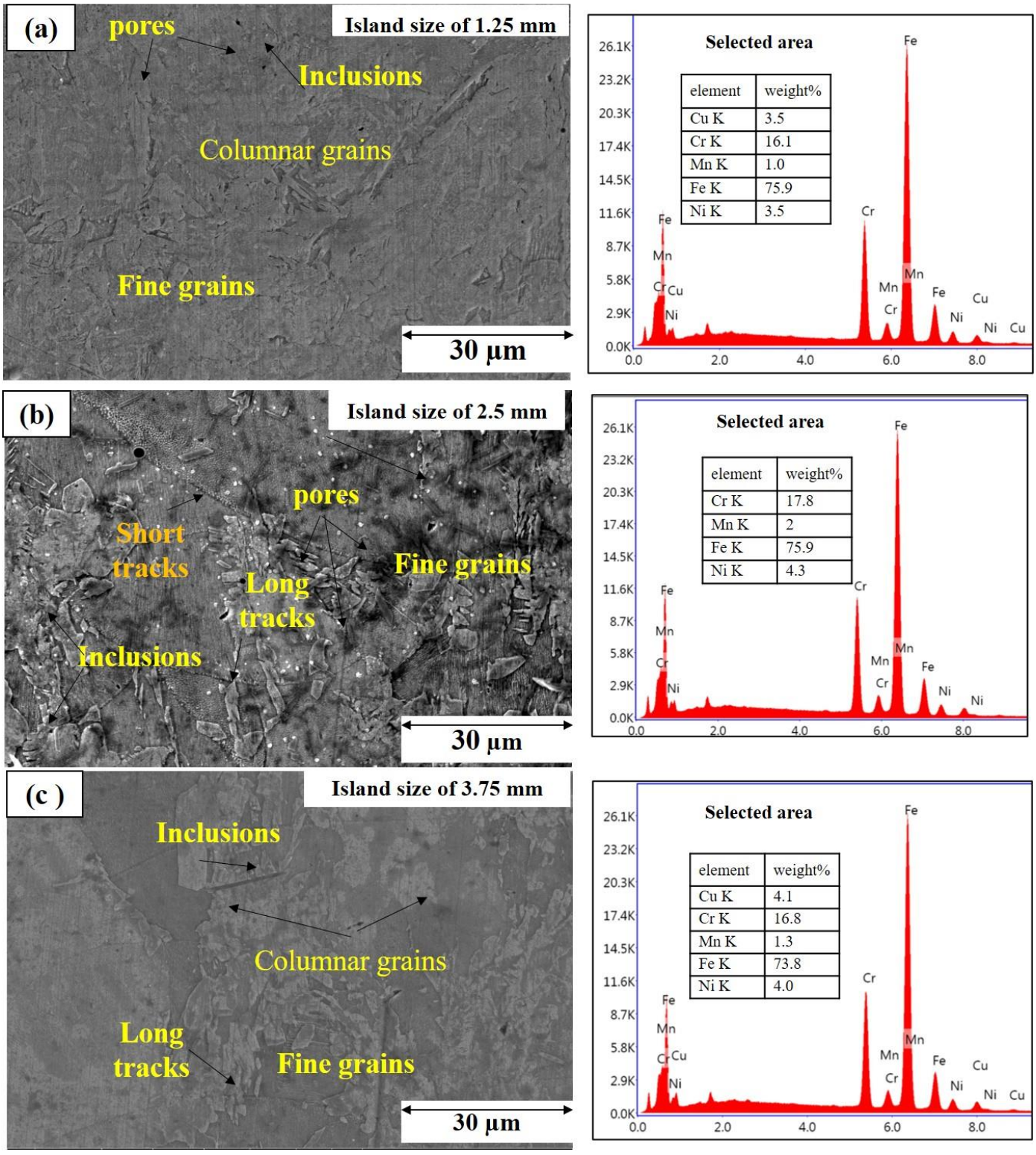

Fig. 6.3 Side surface SEM images of hexagonal island samples with a variation of island sizes of a) 1.25mm, b) 2.5mm and c) 3.75 mm

Several micropores were observed at a 1.25 mm island. At 2.5 island size, only some micropores were observed compared to micropores in 1.25 mm island size While the island size increased from 2.5 to 10 mm, the number of micropores increased. There were no severe defects such as unmolten pores or cracks in smaller island sizes. When the island size increased, the powder between the island would not melt completely, which lead to porosity of the samples. At larger island size, reduction of preheating effect occurs, a large temperature gradient is generated within the molten pool leading to higher Marangoni convention and higher melt instability. So, defects like micropores easily occur. So, the hardness of the sample with hexagonal island size 2.5 mm was higher than all the samples with different island sizes as the molten pool was stable and irregular. The hardness varied with island size with higher hardness exhibited due to fine grain size and phase change from ferrite to austenite.

6.5. Phase Analysis

Fig. 6.4 depicts the results of the phase study using XRD on the side surfaces of hexagonal island samples with a range of island sizes of 1.25, 2.5, and 3.75 mm. Austenite and ferrite phases were present in all of the samples. Ferrite phase was discovered all of the samples at 44.393 degrees, and austenite phase was detected in all the samples at 43.600 degrees. Hexagonal island samples with a range of island sizes of 2.5 mm had the maximum intensity. It was caused by microsegregation and changing thermal stresses.Variation in residual stresses was the cause of small shift in the ferrite phase at the plane (110) of higher hexagonal island samples with a range of island sizes of 2.5 mm. For hexagonal island samples with a range of island sizes of 2.5 mm sample, the lattice plane (110) peak position was detected at 44.59063 degrees, and at 44.5721 degrees, for low and higher hexagonal sizes of 1.25- and 3.75-mm. Equation (6.1) was used to get the crystallite size (d) for three energy density samples

$$d = \frac{k.\Lambda}{\beta.cos\Theta} \qquad (6.1)$$

In this formula, k is the Scherrer constant (0.9), Λ is the wavelength of the X-ray source, β is the full width at half maximum (radians), and Θ is the peak position (radians). For hexagonal island sizes of 2.5,1.25 and 3.75 mm samples, the estimated crystallite size was 36.9412 nm, 36.9463 nm, and 36.9530 nm, respectively. The hexagonal 2.5 mm island sample yielded the smallest crystallite size. From Fig. 6.4, it can be seen that a smaller crystallite size caused the peak

width of the hexagonal 2.5 mm island size sample to increase relative to hexagonal 1.25 mm and 3.75 mm island size samples. Due to complete melting of the powder particles and fewer defects, hexagonal 2.5 mm island size samples produced finer crystallites than other two.

These samples' atomization process involved nitrogen uptake, which led to greater stabilisation of FCC austenite phase. Since nitrogen is an austenite stabiliser, the processing chamber was kept in a nitrogen environment during the sample's deposition, which led to high austenite phase. This was noted in prior research for samples that were as-built, where the α-ferrite phase was found at the (110) lattice plane and the γ-austenite phase at the (111) lattice plane.

,

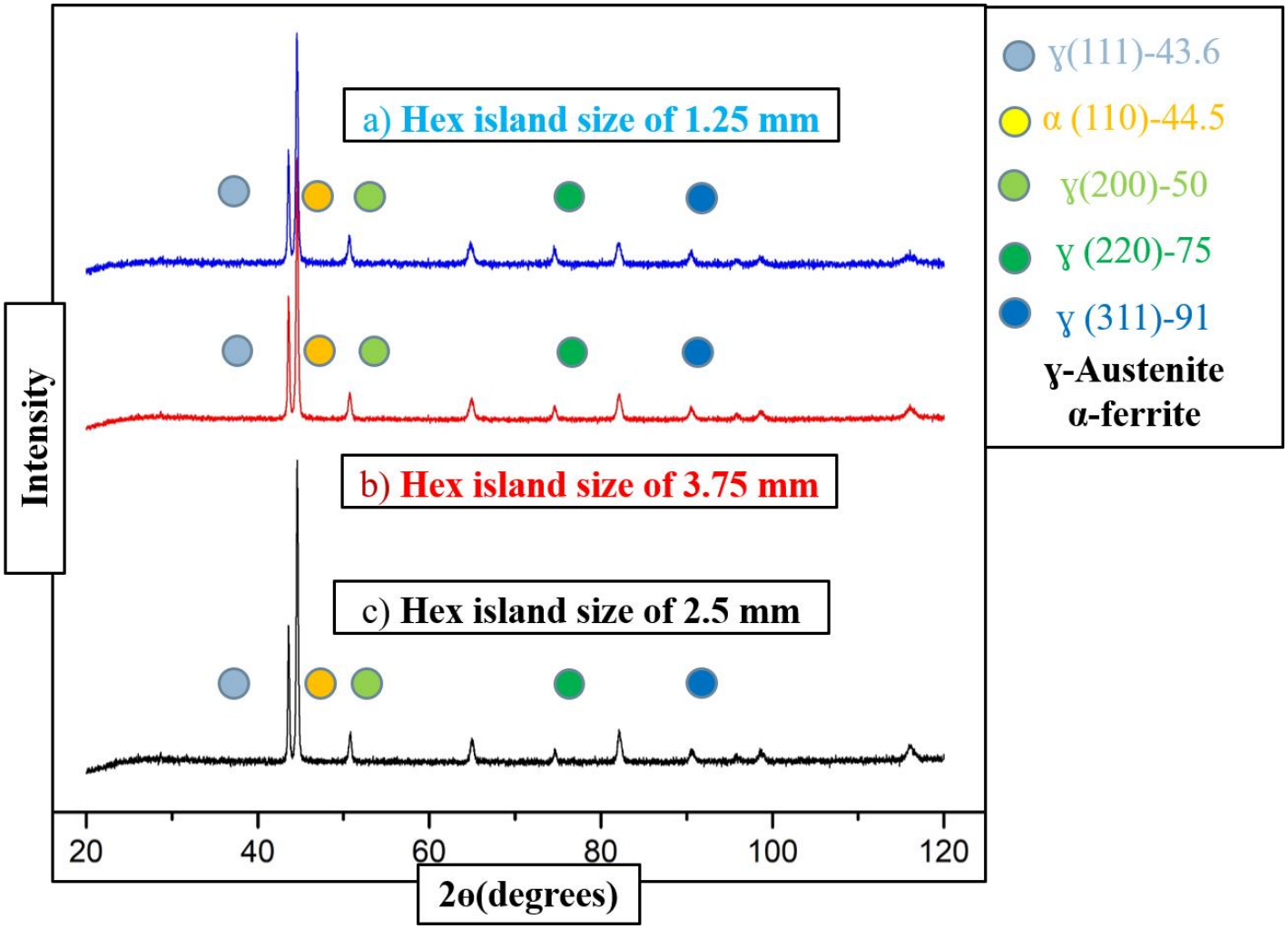

Fig. 6.4.XRD image of hexagonal island samples with a variation of island sizes

6.6. EBSD analysis

In order to comprehend and study the microstructure and phase composition of the hexagonal scan strategy samples with island sizes of 2.5 mm and 10 mm, EBSD analysis was carried out, as shown in Fig. 6.5 and 6.6**.** The microstructure mainly consists of ferrite (red color) and austenite (green color) and is confirmed by XRD phase analysis. A large number of fine grains were observed in austenite phase region. They formed due to large strains at grain boundaries, high density of dislocations and fine grain size.

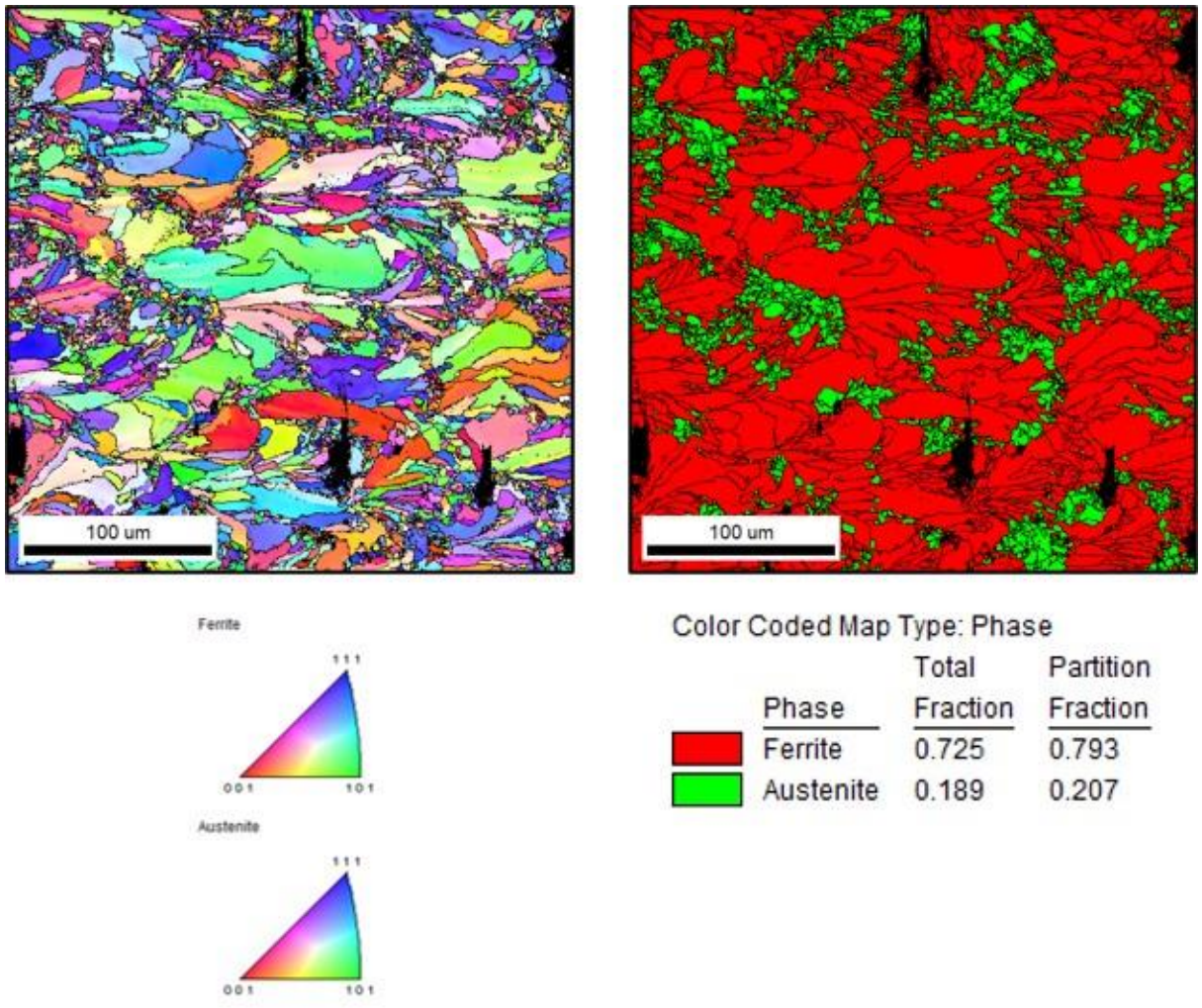

Fig. 6.5.EBSD images of the hexagonal island size of 2.5 mm

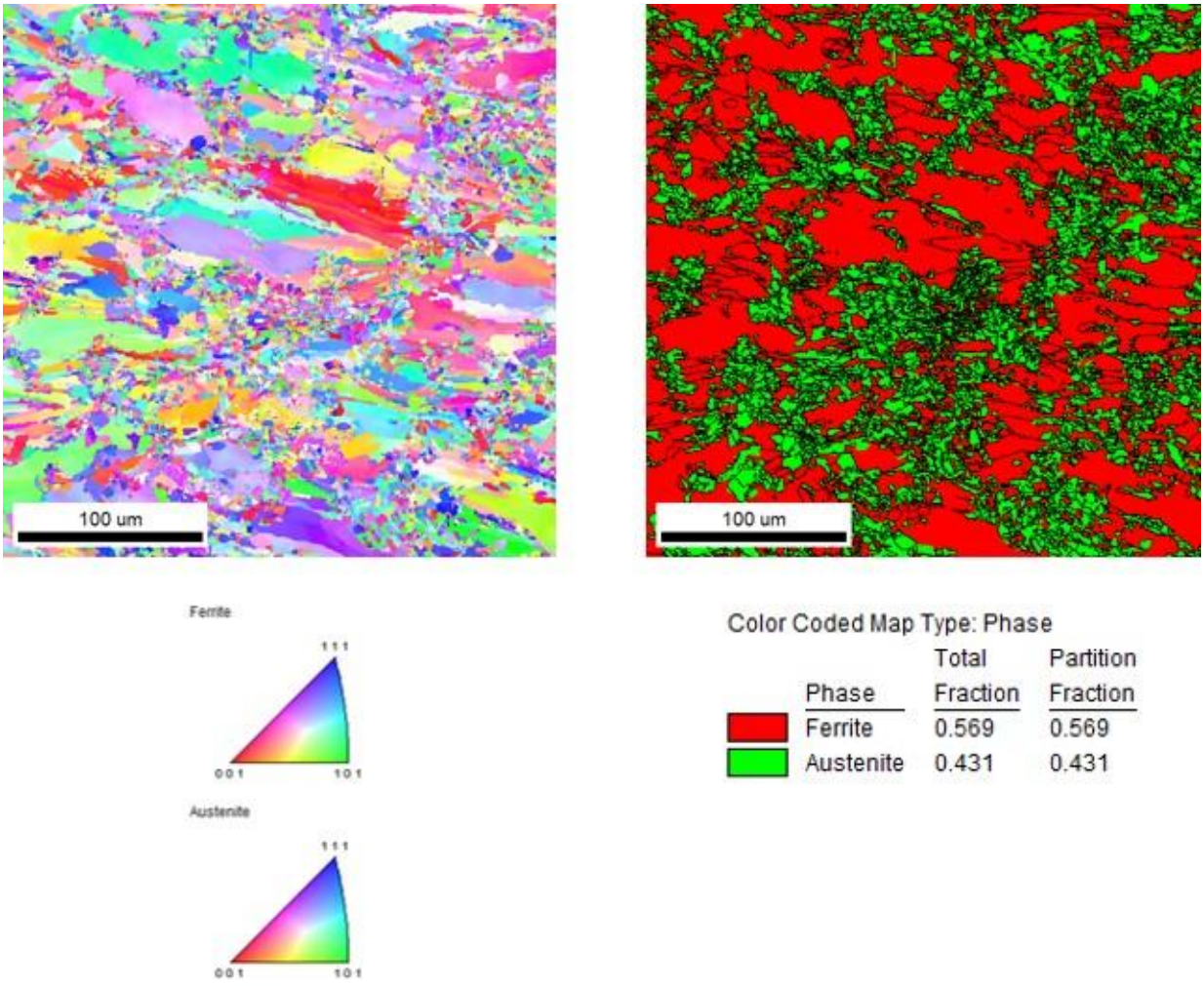

Fig. 6.6. EBSD images of the hexagonal island size of 10 mm

Table 6.1. The statistical data for the EBSD results

Sample condition	Grain size (μm)	Phase partition fraction %	
		Ferrite	Austenite
Island size of 2.5mm	2.14823	72.5	18.9
Island size of 10mm	2.66766	56.9	43.1

Both samples had the EBSD orientation maps and matching phase volume percentages that are shown in Fig. 6.5 and 6.6. The same inverse pole Fig. map, which is displayed in the lower left corner of each image, was used to observe all grain orientation maps. When compared to a sample with 10 mm hexagonal island size, the fraction of columnar grains falls for 2.5 mm, while fine

grains rise in proportion. The EBSD orientation maps shown in Fig. 6.5 and 6.6 almost show ɣ-austenite phase in the finer grain size area for both hexagonal samples with 2.5 mm island size and 10 mm size. The volume fraction and area-weighted mean grain size were obtained for both samples. The volume fraction for ɣ phase increases from 18.9% to 43.1 % while there is a decrease in α-ferrite phase from 72.5 % to 56.9%, which decreases hardness for 10 mm sample. (Table 6.1)

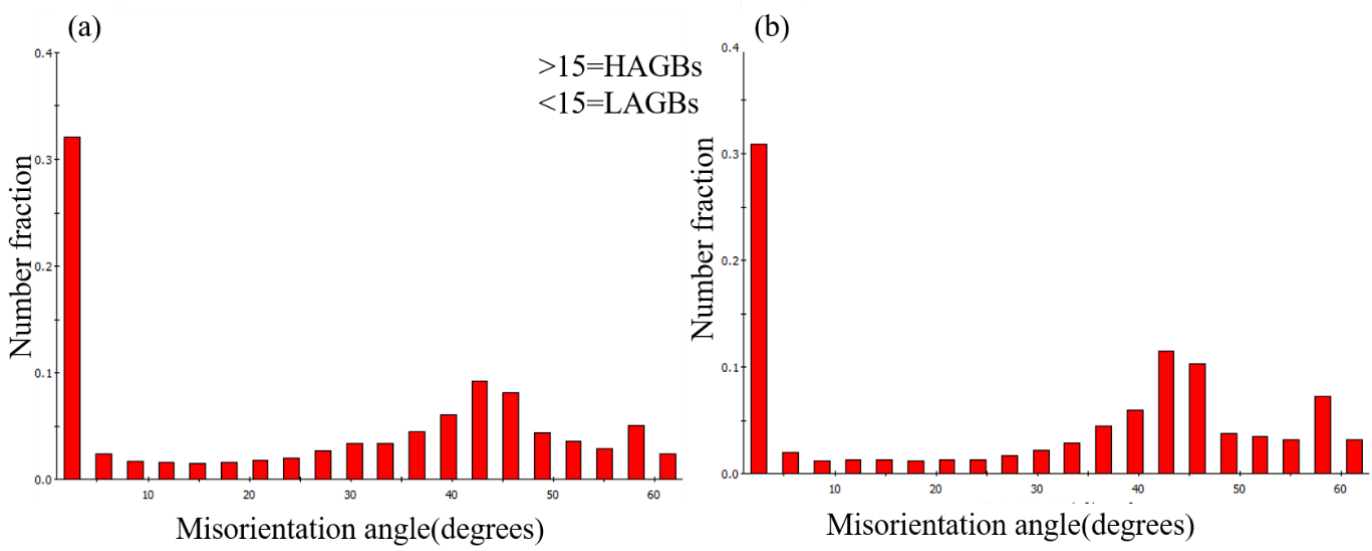

Fig. 6.7.Misorientation angles for the sample with hexagonal island sizes of 2.5mm and 10mm

It can be observed that both samples with hexagonal samples with 2.5 mm and 10mm island sizes have a high fraction of low angle grain boundaries as shown in Fig. 6.7**,** which indicates the disruption of larger grains and a deformed state. The volume fraction of high angle grain boundaries increased for 10 mm hexagonal island size. The average misorientation angles for 10 mm hexagonal island size were 26.8053 and for the hexagonal sample with 2.5 mm island size, it was 28.9953 respectively.

6.7. Residual stress

For samples using the hexagonal scan strategy, on the top surface of each specimen, along the building direction, residual stresses were measured for island sizes of 1.25, 2.5, 3.75, 5,7.5, and 10mm. Three angles of $\sin^2 \psi$ method were used to calculate the stress readings (0,90,135). The maximal principal stress is indicated by letter σ (i=1, 2, 3), while other stresses are orthogonal to it.

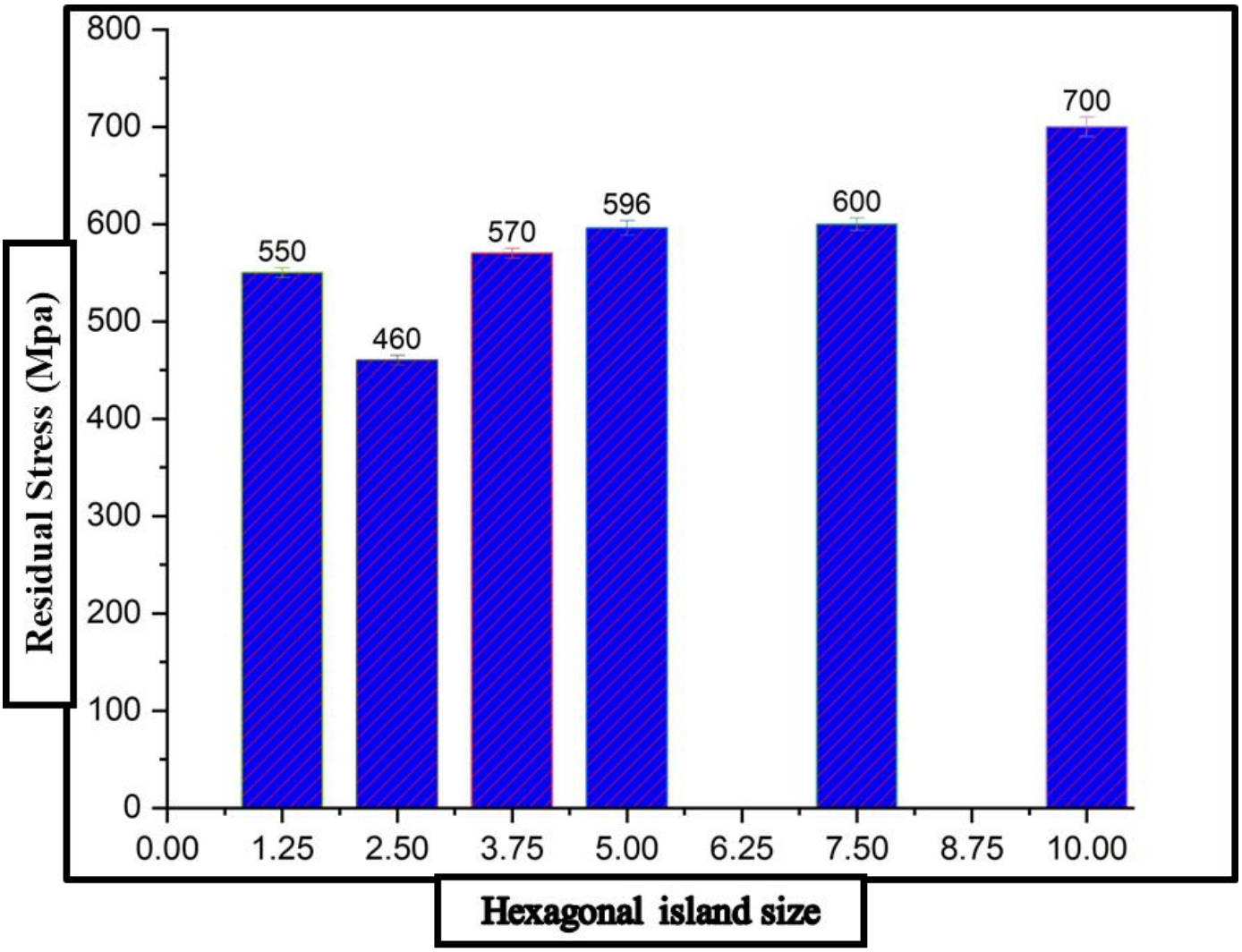

Fig. 6.8.Variation of residual stresses with hexagonal island size samples with island size

At high hexagonal island size, balling defect occurred which made the sample more brittle with non-uniform deposition of powder compared to previously deposited layers. So, there was high porosity and low density in the high hexagonal island size sample compared to low hexagonal island size samples, which also resulted in more residual stresses.

In general, complex stresses are formed in L-PBF process as a result of subsequent layer's tendency to shrink during the cool-down phase, whereas such deformation is limited by the preceding neighboring layer. Tensile stress is formed in the next layer, while compressive stress is formed in the previous layer. Residual stresses have a significant impact on the functionality and service life of components processed using L-PBF approach. One of the best methods for

reducing residual stress was to be island laser scanning, and the residual stress dropped as the size of the island decreased [63]**.** The residual stress increases as the island size increases when the island size is more than 2.5 mm, as shown in Fig. 6.8**.** When a large island size was used, it produced a weak preheating effect and a long scanning track, resulting in a high-temperature gradient and, as a result, high residual stress. Furthermore, because of laser rescanning and pre-heating impact by preceding island, island border overlap regions frequently serve as zones of stress release [64]. When the island size decreases, the stress release areas at borders /overlap regions of the island increased, which resulted in a decrease of residual stress for 17-4 PH SS samples but for a sample with an island size of 1.25 mm, the residual stresses were generated inside the sample, resulting in higher residual stresses compared to island sizes of 2.5 mm. Lu et al [44] located cracks on the island size of two mm due to the massive overall scanning length and big overlap regions. The scanning time of every layer expanded in comparison to sample with higher island sizes. Large laser energy was given to sample with decrease island size ensuing in excessive residual heat impact and massive molten pool depth

Excessive laser energy was employed at a noticeably small island length, ensuring in an excessive level of residual heat effect. This implied increased residual stresses at noticeably decreased hexagonal island length. So, the ranking of samples with residual stresses was 2.5mm<1.25mm<3.25mm<5mm<7.5mm<10mm. The island size impacts the residual stresses. So, the residual stresses decreased at a hexagonal island length of 2.5mm.

6.8. Corrosion studies

Fig. 6.9 indicates potentiodynamic polarization curves of 17-4 PH SS samples processed through L-PBF at distinct island sizes in 3.5 wt.% NaCl at room temperature. Corrosion potentials (Ecorr) values of around -0.370V to -0.003V were obtained for distinct specimens indicating that typical passive behavior for distinct island sizes. It was also determined that corrosion current density swiftly expanded in the anodic branch of polarization curves of 17-4PH SS samples with distinct island sizes, indicating that pitting corrosion was generated. Pitting corrosion is usually associated with breakdown of passive films formed at the surface of the samples, which is attacked by chloride. The pitting resistance increased with decrease in island size and it was also more for higher island sizes (Table 6.2). Pitting resistance became better for island length of 2.5 mm as compared to different island sizes. Corrosion current density was determined from polarization

curves from Tafel slope exploration method, which is another critical parameter for comparing corrosion rate and corrosion resistance. The minimal corrosion current was received for a sample with an island size of 2.5 mm, and it was steady with Ecorr values. Thus, it was observed that the sample with hexagonal island size of 2.5 mm obtained superior corrosion resistance compared to higher or lower hexagonal island sizes.

There are reasons for lower corrosion resistance at lower and higher island sizes. They are grain refinement and molten pool boundary at high grain boundary density. If the reaction activity along the molten pool is stronger,corrosion is higher. Similarly, the precipitates also act as microelectrodes to boost the corrosion process. But there is not much difference in the precipitate formation and grain size distribution because of which the molten pool boundary configuration acts as key factor in determining the impact of corrosion resistance on L-PBF components with different island sizes. It was determined from the optical images of the side surface of the samples that island size affects the molten pool configurations. At hexagonal island size of 1.25 mm, regular molten pool boundary combined with massive island borders may be identified, leading to excessive molten pool boundary density. The number of island borders decreased at 2.5 mm island size which resulted in decrease in molten pool boundary density. As the island size increases, the influence of island borders decreases, but a few ellipsoidal molten pools had been found at the bottom of the layer leading to molten pool density increase. Thus, the molten pool density was higher at small and high hexagonal island sizes and it became disorderly at very high island sizes. The molten pool density at small island sizes was due to excessive island borders however at high island sizes it was due to high temperature gradient and high molten pool depth.

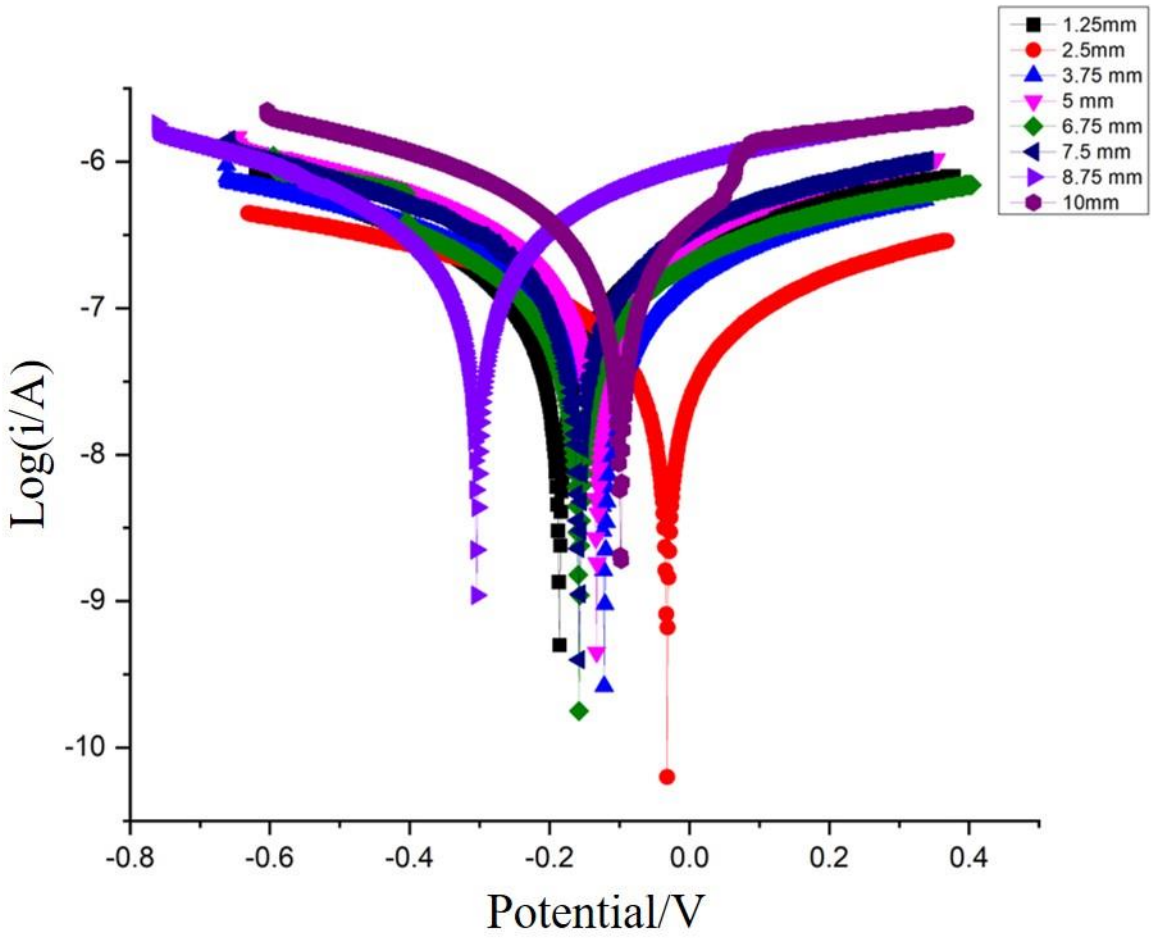

Fig. 6.9.Corrosion curves for samples with different hexagonal island sizes (Tafel plots)

Table 6.2. Corrosion potentials of samples with different island sizes

Island size (mm)	E_{corr} (V)
1.25	-0.186
2.5	-0.032
3.75	-0.122
5	-0.133
6.25	-0.158
7.5	-0.158
8.75	-0.304
10	-0.099

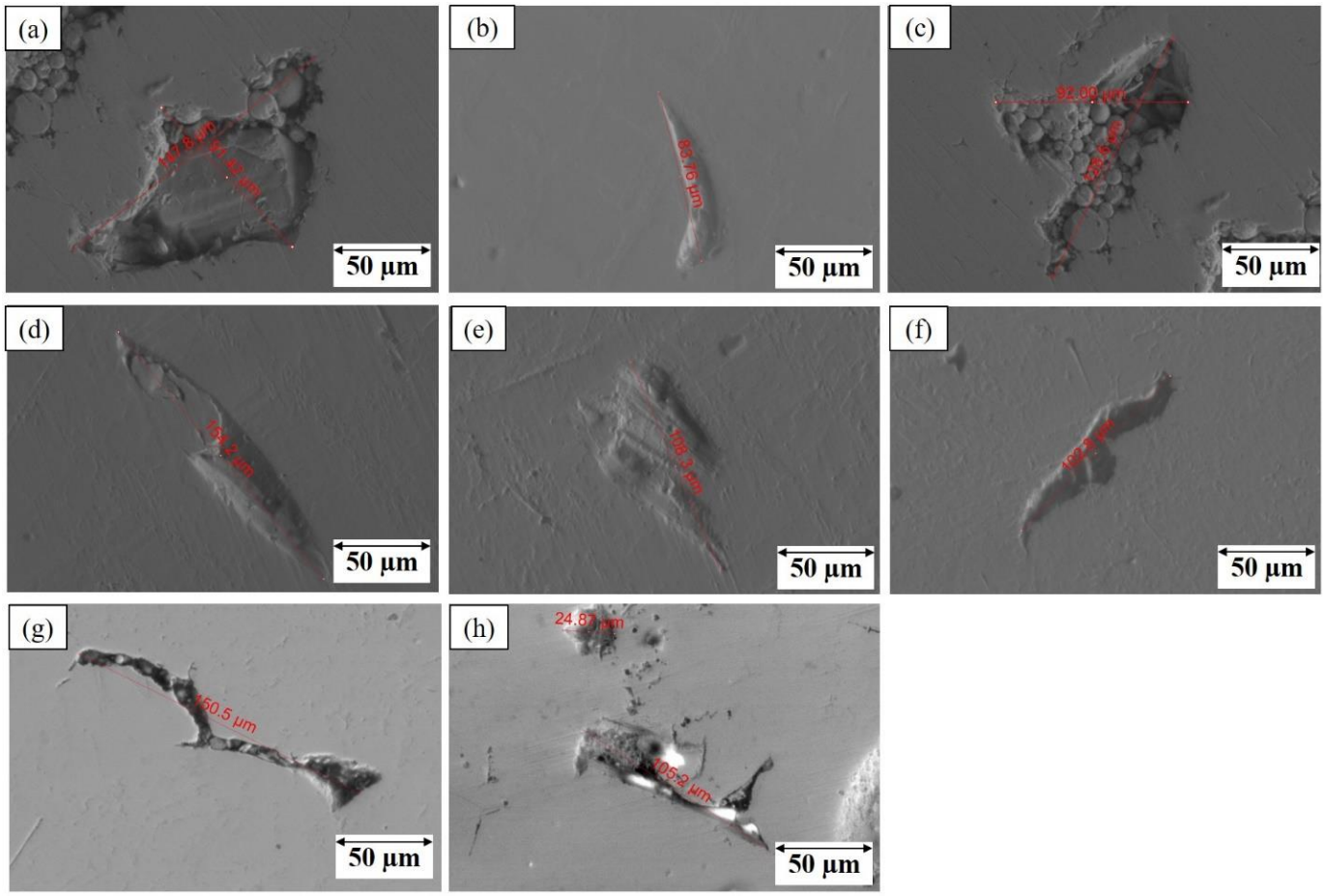

Fig. 6.10.SEM images of samples with hexagonal island sizes

Following the Tafel polarisation test, SEM was used to examine the corroded samples (Fig. 6.10**)**. All the samples with various island sizes showed typical morphologies. All of the samples contained both large and small pits. Pits developed as a result of ongoing corrosion activity. According to Fig. 6.9, there were more pit morphologies seen in samples with low and larger island sizes, however none of the samples had corrosion cracks visible. The pits that were noticed are stable and located in the ferritic region. Austenitic grains prevent the creation of pits because they have greater corrosion resistance than ferritic grains. Deep and massive pits were observed for 1.25mm and 8.75 island size samples, indicating high corrosion while lower pits were observed at 2.5mm island size, indicating superior resistance to corrosion.

Electro chemical impedance spectroscopy (EIS) measurements were made to investigate the surface state of 17-4 PH SS samples with various island sizes, with the findings shown in Fig.

6.11. According to Fig. 6.11.(a), capacitive loops were seen for every specimen in the Nyquist plot. The Nyquist plot shows that the island size of 2.5 mm has a bigger radius than other samples' islands while the island size of 10 mm has a smaller radius, indicating that the sample with hexagonal island size of 2.5 mm showed lower corrosion rate. Based on bode plots, improved impedance was found in Fig. 6.11.(b) for 2.5 mm in length for the hexagonal island, which is connected with Nyquist plot. Corrosion resistance dropped when island size increased from 2.5 mm to 10 mm and then dropped at 1.25 mm, which was in good agreement with findings from polarization tests.

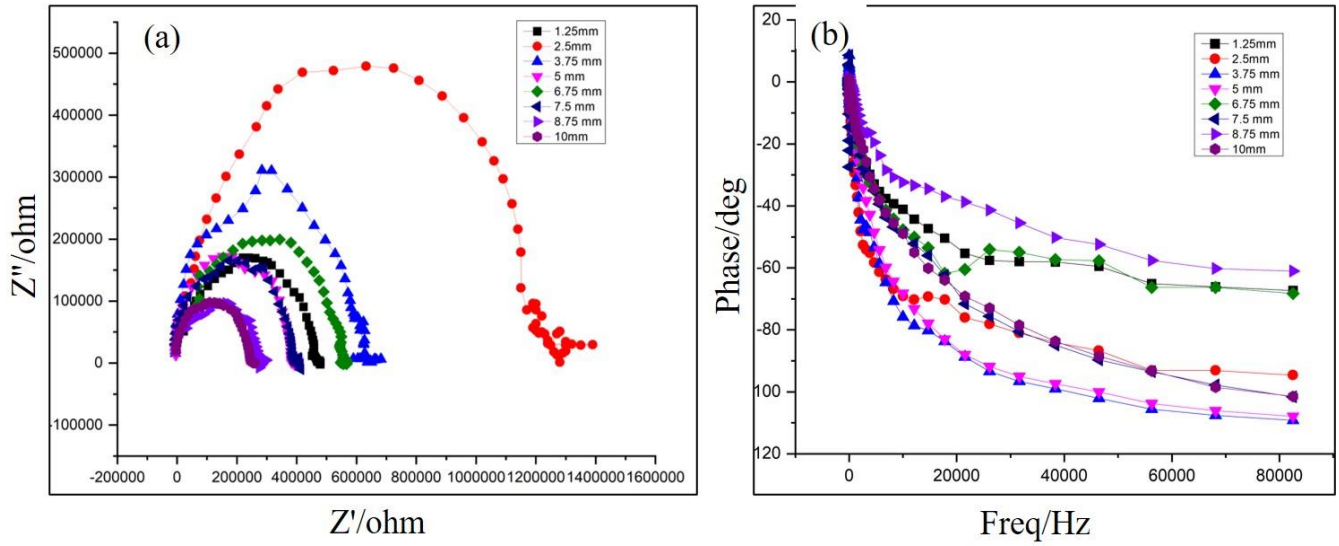

Fig. 6.11.Impedance plots for different hexagonal island sizes (a) Nyquist plot and (b) Bode plot

6.9. Summary

The hardness varied with island size, with higher hardness exhibited for 2.5 mm island size due to fine grain size and variation in the percentage of austenite and ferrite. The EBSD orientation maps show ɣ-austenite phase in the finer grain size area for both hexagonal samples with 2.5 mm island size and 10 mm size. The volume fraction for ɣ phase increased from 18.9% to 43.1 % while there was a decrease in the α-ferrite phase from 72.5 % to 56.9%, which increased hardness.The residual stresses increased as the hexagonal island length increased because while a large island size was used, it produced a long scanning track with a vulnerable pre-heating effect, ensuing in excessive-temperature gradient and, as a result, excessive residual stress. Furthermore, due to laser re-scanning and pre-heating effect from the previous island, the overlap regions at island borders

frequently serve as stress release zones. The residual stresses and corrosion rate were much lower at a hexagonal island size of 2.5mm due to lesser number of formations of pits.

Chapter-7

Effect of heat treatment on the fatigue and damping behavior of L-PBF 17-4 PH SS

7.1. Introduction

In the previous chapter, the influence of hexagonal island size on the Microstructure, hardness, corrosion behaviour are carried out at different island sizes. Considering the previous chapter the best parameter conditions was used for understanding the impact of heat treatment on the fatigue and damping behaviour correlating with microstructure.

7.2. XRD analysis, microstructure and damping behaviour

XRD analysis was performed to estimate the phases and precipitates present in L-PBF samples made with different heat treatments, as shown in Fig. 7.1. Retained austenite was present in all the samples. The occurrence of retained austenite was more at grain boundaries where ferrite formation was obstructed and faster cooling rates of L-PBF samples led to high fine grain size which ultimately results in high percentage of formation of retained austenite. The specimen preparation and powder atomization were also done in nitrogen environment which also contributed to the presence of austenite. As built (AB) and MOD H900 (AB) showed more amount of retained austenite while overaging samples showed lower amount of retained austenite phases. Ferrite phase was present in all the samples. Cu and chromium carbide precipitates were present in all samples but in overaged (H 1150) samples, these precipitates were more compared to aged samples. Williamson Hall's theory was used to calculate dislocation density, microstrain, and residual stresses. It was understood that dislocation density increased for solution annealing (SA) followed by standard aging (H 900) samples compared to as-built, Mod H 900 (AB), and H 1150 samples with lower dislocation density (Table 7.1).

Table 7.1. Average grain size, area, hardness and dislocation density for the samples

Sample(Heat Treatment) condition	Temperature/Time/Type of cooling	Dislocation Density(10^{-3})	Grain size (μm)	Grain area $(\mu m)^2$	Hardness (VHN)
As built (AB)	-	9.05E-06	0.95	1.26	379
Solution Annealing (SA)	AB/1038°C/30 min/*AC	9.205534	0.56	2.1	398
Aging (H 900)	SA/483°C/4 hour/*AC	3.231405	0.65	1.69	383
Over aging (H 1150)	SA/621°C/4 hour/*AC	0.001852	0.7	1.26	362
MOD H900 (SA)	SA/525°C/4 hour/*AC	0.079781	0.69	1.84	380
MOD H900 (AB)	AB/525°C/4 hour/*AC	0.004504	1.09	1.37	362

*AC-Air Cooling

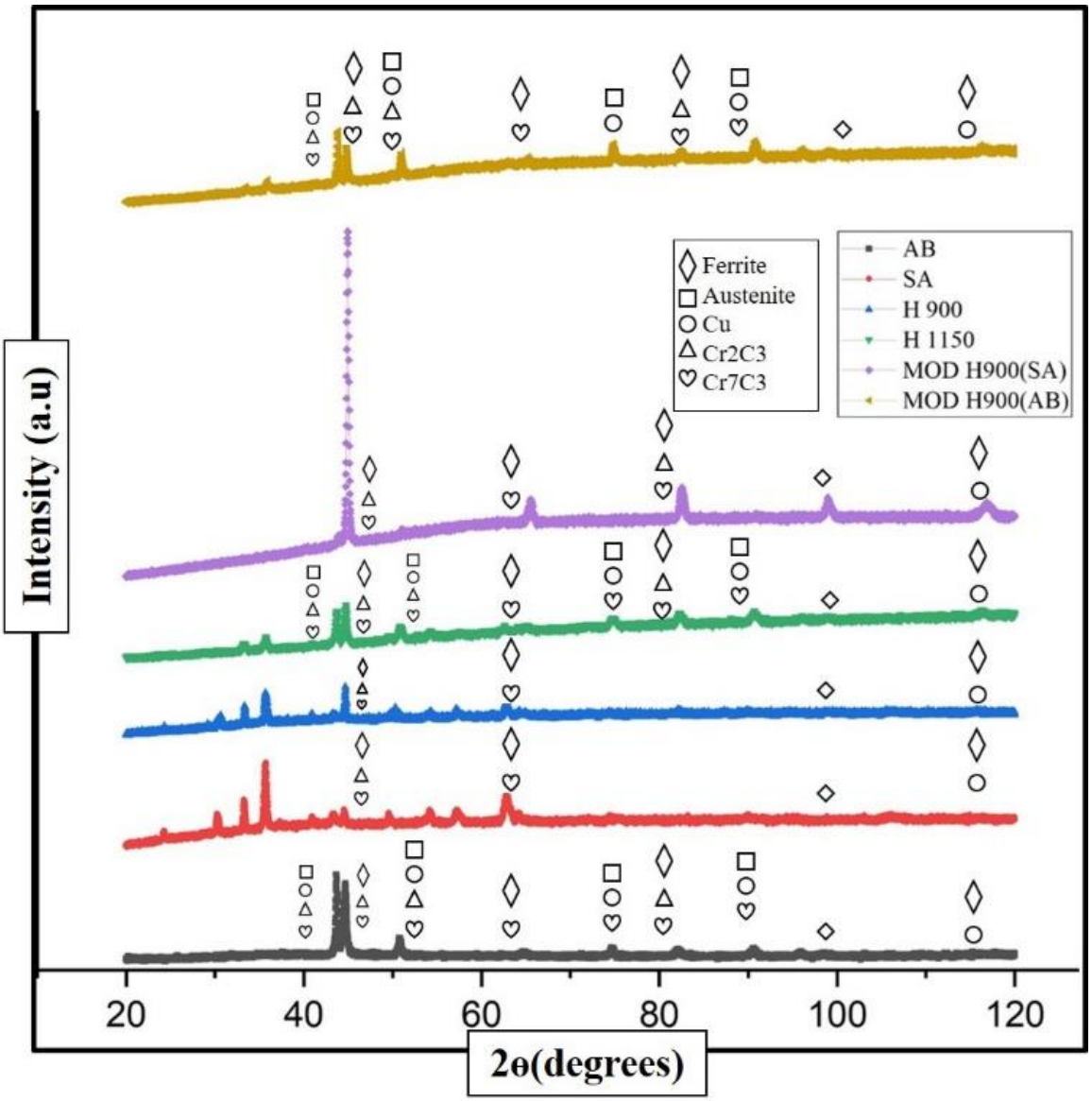

Fig. 7.1.X ray diffraction patterns for L-PBF samples made with different heat treatments

EBSD analysis (Fig. 7.2. (a)) showed that as built sample contains more retained austenite phase than solution annealed sample (Fig. 7.2. (b)). the sample after aging (H900) contains reverted austenite (Fig. 7.2. (c)) and it increases the aging temperature increases from 483°C (for H900) to 661°C (for H1150) (Fig. 7.2. (d)). Coarse grain structure for Cu-rich precipitates was observed in overaged samples (H1150) (Fig. 7.2. (d)). But there was no substantial change in reverted austenite when aging temperature was increased to 525°C (Fig. 7.2. (e)) compared to standard aging temperature of 483°C (Fig. 7.2. (c)). But the samples that underwent only aging without solution annealing showed a large amount of retained austenite (Fig. 7.2. (f)). The presence of austenite

phase and coarser grain size (Fig. 7.2.g, j and l) decreases the hardness of the sample, especially for as-built, Mod H 900 (AB), and H 1150 samples and it was lowest for Mod H 900 (AB) samples. This is attributed to an increase in aging temperature to 621°C which makes Cu-rich precipitates coarsen and increase reverted austenite while reducing hardness. The solution annealing without aging and sample with standard aging (Fig. 7.2.h and i) were given highest hardness because of the lowest reverted austenite, fine grain size (Table 7.1), and highest dislocation density.

The frequency dependent damping characteristics are shown in Fig. 7.3. (a). The increase in frequency resulted in decrease in damping capacity. The grain boundary area increased as grain size decreased which led to increase in damping capacity. Moreover, the decrease in the number of dislocations also decreased the damping characteristics as the frequency increased, as confirmed by Granto-Lucko damping theory [65]. This is the reason for decrease in the damping capacity as frequency increases. Moreover, solution annealing followed by standard aging samples led to large dislocation density compared to as built, Mod H 900 (AB), and H 1150 samples which increased damping capacity. The temperature dependent damping characteristics are shown in Fig. 7.3. (b). The damping capacity increased gradually up to 110°C and steeply increased for all samples from 110°C. As the temperature increases, the damping capacity increased and it was due to ease of grain boundary movement at higher temperature and rapid energy dissipation. The SA sample with fine grain size showed highest damping characteristics and Mod H900 (AB) sample with highest grain size showed lowest damping capacity. So it is understood that grain size and grain boundary area impact damping capacity and it was also confirmed by other researchers[65]. The solution annealing sample with fine grain size and higher grain boundary area followed by aging sample had higher damping capacity and the damping capacity reduced as the temperature increased for all the samples.

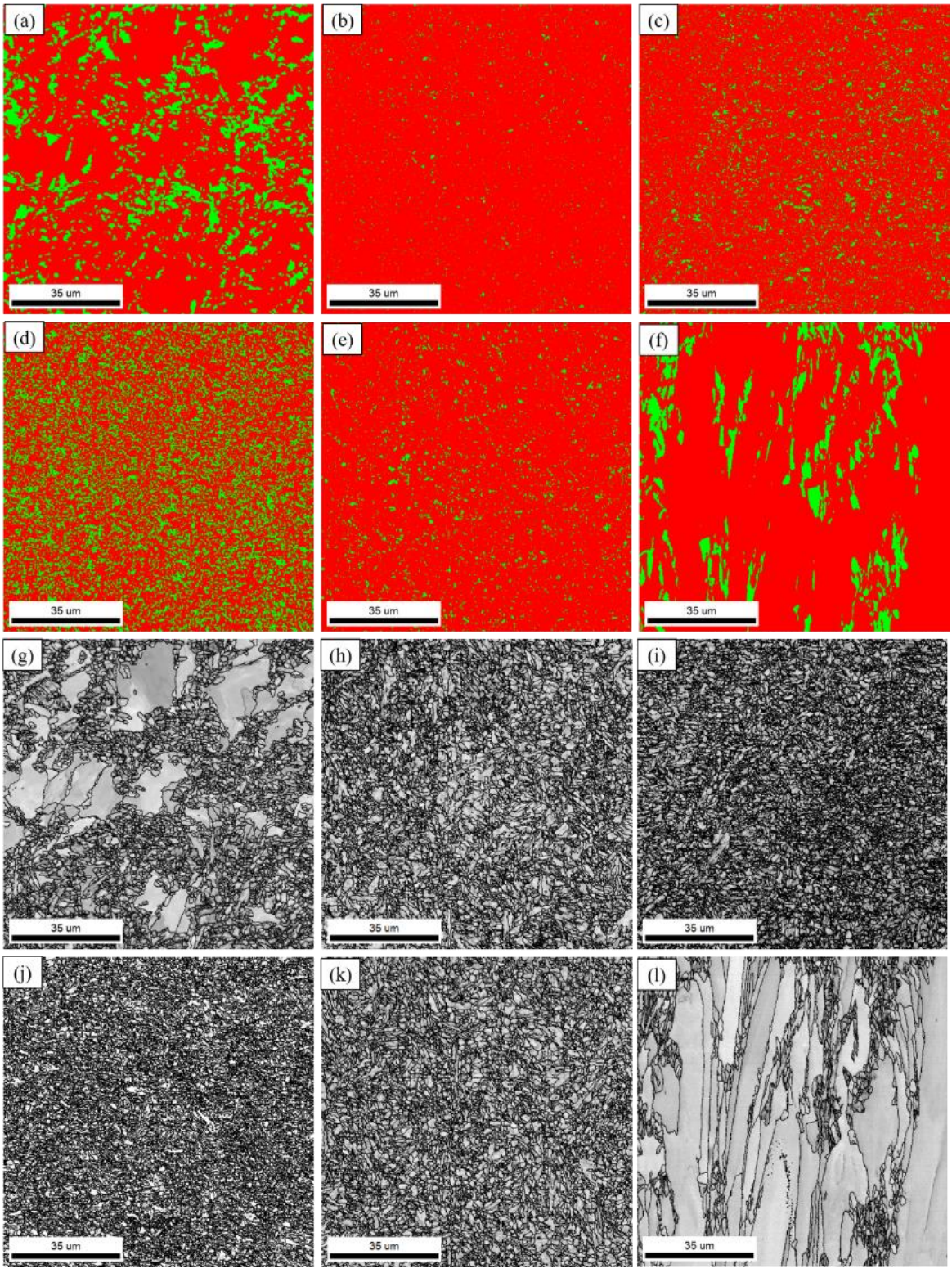

Fig. 7.2. (a-f) EBSD analysis showing amount of retained and reverted austenite (green) in ferrite (red) matrix , (g-l) Grey scale EBSD images for L-PBF samples

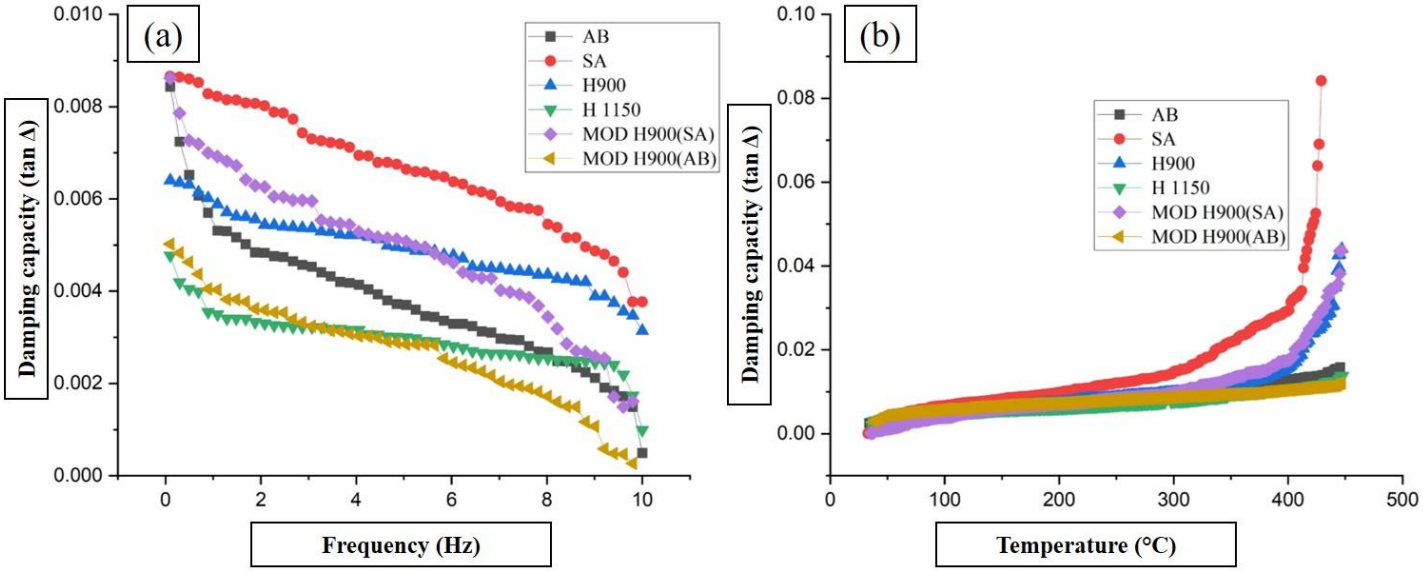

Fig. 7.3. (a) Frequency dependent and (b) temperature dependent damping capacity of L-PBF samples

7.3. Fatigue behavior

The fatigue crack length (a) vs. number fatigue cycle (N) graph was plotted initially to estimate the fatigue life of samples, as displayed in Fig. 7.4 (a). It was identified from the graph that the fatigue life of heat treated samples was greater than that of as built samples, and with increase in fatigue cycles, FCG rate also accelerated. It proves that heat treated samples stopped the fatigue crack from further expanding. In addition, it can be observed from the graph that the a-N curve of heat treated samples consists of fluctuations, while it was smooth for the base metal. In heat treated samples, various factors such as fine-grained structure, a high fraction of grain boundaries, precipitation factor, retained austenite etc., act as obstacles for fatigue crack propagation and stop the crack from expanding further.

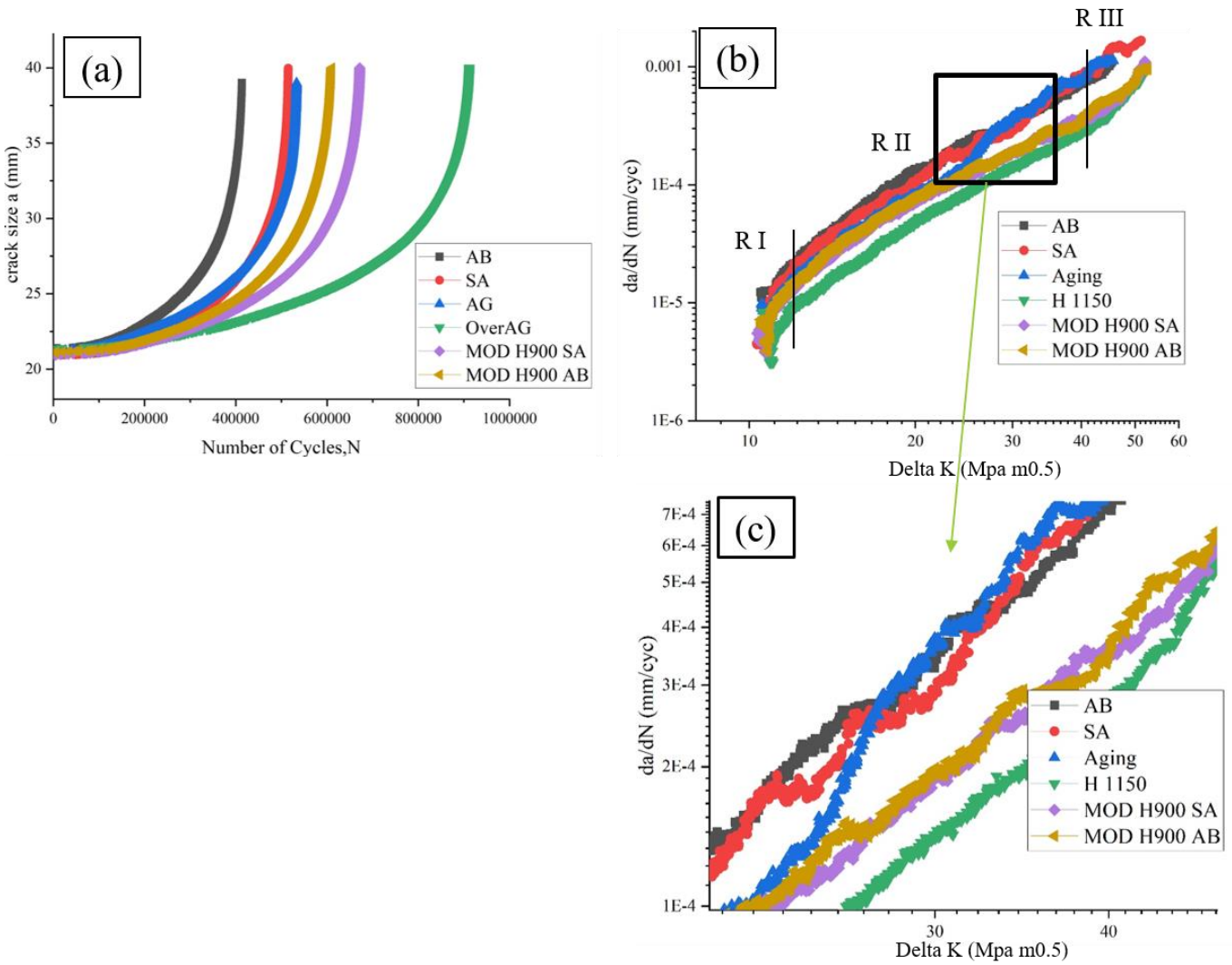

Fig. 7.4. (a) Crack size (a) vs. Number of cycles (N) curve (b) FCG rate vs. ΔK (c) region II of FCGR vs ΔK.

The fatigue crack growth rate (FCGR) was further studied by plotting the graph between fatigue crack growth rate (da/dN) and stress intensity range (ΔK), as shown in Fig. 7.4 (b). The fatigue crack growth rate of all the samples accelerated with the number of cycles. Initially the FCGR of as built, solution annealing and aging samples is more compared to other samples because of the difference in reverted austenite. The FCG rate of solution annealing and aging samples was less than FCG rate of as built samples after 2×10^{-4} due to difference in residual stresses. (Fig. 7.4 (c)). Similarly, the FCG rate of solution annealing samples was almost comparable with aging samples and it is lower than as built samples. It was evident that there are finer grains and more grain boundary area compared to as built samples which resulted in lower FCGR for solution annealing

and aging samples. The finer grain boundary area hindered crack propagation rate. It was also observed that there are lower residual stresses for solution annealing and aging samples compared to as built samples. The lower residual stresses also hindered crack propagation rate. The finer grain area and lower residual stresses in solution annealing and aging samples which resulted in better fatigue life compared to as built sample.

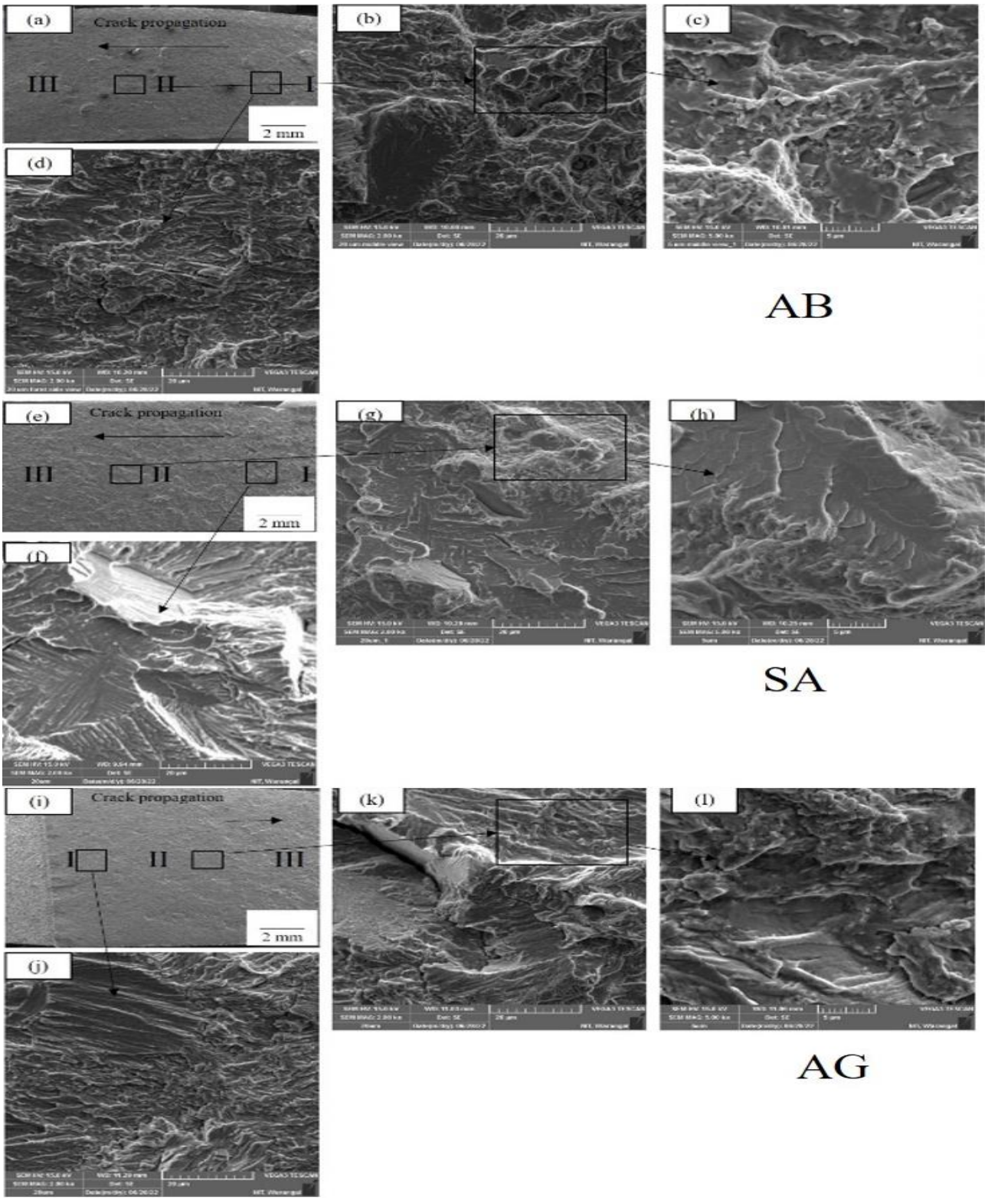

Fig. 7.5.(a,e,i) low magnification images of as built, solution annealing and aging samples, (b,f,j) R-I, (c,g,k) R-II and (d,h,l) enlarged view R-II fractured surfaces

The fractured surfaces of as built, solution annealing and aging samples were observed using SEM. Fig. 7.5 (a) shows the magnified image of region I of as built samples. The macroscopic images show three regions. The ridges and plateaus were present in region I (Fig. 7.5 (d)). There were fatigue striation marks present in Region II. The fatigue striation marks arrest the fatigue crack growth rate (Fig. 7.5 (c)). The magnified images of region II shows that fatigue striation marks were perpendicular and there were lower gaps present between these cracks. There are also secondary cracks apart from fatigue striation marks present which retards crack growth rate. The fracture surfaces of solution annealing and aging samples are shown in Fig. 7.5 (e-f), (i-l) respectively. The fractured surfaces of heat treated and as built samples were similar and the enlarged view of region II for solution annealing and aging samples were shown in Fig. 7.5 (h,l). The gap between the striation marks increases for solution annealing samples followed by aging samples compared to as built samples. These striation marks are continuous for solution annealing samples followed by aging samples. The distance between striation marks and their continuity shows the better fatigue life for solution annealing and aging samples compared to as built samples. The fractured surfaces obtained from SEM were correlating the results

7.4. Summary

The impact of different heat treatments on the damping behavior of 17-4 PH SS made by Laser Powder Bed Fusion (L-PBF) for the frequency and temperature dependent characteristics were studied through Dynamic Mechanical Analyzer and the following conclusion were reached. Lowest micro strain, lowest residual stresses and highest hardness were obtained for the solution annealing sample and it was due to less refined austenite compared to other samples, finer grain size and highest dislocation density. The frequency dependent damping capacity decreased for samples which did not undergo solution annealing process and it was more for solution annealing sample because of its microstructure which evolved with highest dislocation density. The temperature dependent damping capacity was more for solution annealing samples because of fine grain size and highest grain boundary area. Moreover, the fatigue life of the solution annealing followed by aging samples was better than as built samples because of the presence of fine-grained structure, lower residual stresses, presence of striation marks, secondary cracks, and dimples in the

HT sample resulted in better fatigue life than the AB. Continous stritation marks are not present in AB

Chapter-8

CONCLUSIONS AND FUTURE SCOPE

8.1 Conclusions

The effect of scan strategies and process parameters like energy density, laser power, and scan speed was examined on the density and micro hardness of 17-4 PH SS built by SLM. A combination of process parameters and scan strategies was selected for microstructural investigation. A range of energy density was selected for further investigation. Then, the effect of different scan strategies like hexagonal (inside out and outside in), rectangular (horizontal, vertical, alternate, and both), strip(horizontal, vertical, alternate, and both) on the microstructure, microhardness, and residual stresses of 17-4 PH SS fabricated by selective laser melting was systematically investigated and analyzed in the research work. Morever the effect of island size hexagonal scan strategy on L-PBF fabricated 17-4 PH SS was systematically studied by considering best energy density and scan strategy on microstructure, mechanical properties, and residual stress .The impact of different heat treatments on the damping behavior of 17-4 PH SS made by Laser Powder Bed Fusion (L-PBF) for the frequency and temperature dependent characteristics were studied through Dynamic Mechanical Analyzer. The fatigue crack growth behaviour of samples with different heat treatments were discussed. The main conclusions were drawn from the investigation and are as follows:

1. The process parameters identified for the samples with the highest relative density(99.2±0.3 %) and hardness(352±3 VHN) are parameters that have a medium energy density of 61.72 J/mm^3, high laser power of 100W, medium scan speed of 1200 mm/s, and employ hexagonal scan strategy

2. The microstructure of all the samples contains large fine grains at the melt pool boundary and columnar grains in the matrix along the laser beam direction**.** The columnar grain boundaries in the vicinity of molten pools were directed towards the top surface of the sample. The proportion of columnar grains decreased at medium energy density, with a corresponding increase of fine grains compared to samples with low energy density

3. Hexagonal inside-out scan strategy exhibited highest hardness (353±5 VHN) among all scan strategy samples because of low thermal gradient and complete fusion of powder particles. These values are comparable with wrought alloy because of high cooling rates and finer grain size for SLM samples.

4. The ranking of the samples with higher residual stresses were strip alternate (760 MPa) > rectangular alternate (550 MPa) >hexagonal inside out strategy (460 MPa) because of long scanning track, weak preheating effect, and high thermal gradient in strip and rectangular scan strategies compared to hexagonal inside out scan strategy.

5. The corrosion rate (6.14×10^{-6}) was less than 0.5 mpy based on weight loss tests, pitting resistance was exceptional with stable pits and free from corrosion cracks. The corrosion resistance was higher for hexagonal inside-out scan strategy samples because of lower defects and higher density.

6. All the specimens with distinctive hexagonal island sizes reached density of >95%. The hardness of the sample with the lowest island size (332±5 VHN) and largest island sizes (330±7 VHN) was lower compared to the 2.5 mm island size hardness (379.22±5 VHN). The hardness varied with island size with higher hardness exhibited due to fine grain size. The hardness variation for the samples was due to variation in the percentage of austenite and ferrite.
7. The EBSD orientation maps show ɣ-austenite phase in the finer grain size area for both hexagonal samples with 2.5 mm island size and 10 mm size. The volume fraction and area-weighted mean grain size were obtained for both samples. The volume fraction for ɣ phase increased from 0.189 % to 0.431 % while there was a decrease in the α-ferrite phase from 0.725 % to 0.569%, which increased hardness.
8. The residual stresses increased as the hexagonal island size increased because while a large island size was used, it produced a long scanning track with a vulnerable pre-heating effect, ensuing in an excessive-temperature gradient and, as a result, excessive residual stress. Furthermore, due to laser re-scanning and pre-heating effect from the previous island, the overlap regions at island borders frequently serve as stress release zones. The residual stresses (460MPa) and corrosion rate (E_{corr} Value:-0.032 V) were much lower at a hexagonal island size of 2.5mm due to fewer formations of pits.

9. The solution annealing without aging and sample with standard aging (398 VHN and 383 VHN) were given highest hardness because of the lowest reverted austenite, fine grain size , and highest dislocation density (9.205534×10^{-3} and 3.231405×10^{-3})

10. The frequency dependent damping capacity decreased for samples which did not undergo solution annealing process and it was more for solution annealing sample because of its microstructure which evolved with highest dislocation density. The temperature dependent damping capacity was more for solution annealing samples because of fine grain size and highest grain boundary area.

11. The FCG rate of solution annealing and aging samples was less than FCG rate of as built samples after 2×10^{-4} due to difference in residual stresses. The presence of fine-grained structure, lower residual stresses, presence of striation marks, secondary cracks, and dimples in the HT sample resulted in better fatigue life than the AB. Continous stritation marks were not there in AB

This study provides the path for choosing best energy density, scan strategy and importance of choosing island size for building engineering applications. Similarly the properties of L-PBF components can be tailored by post processing techniques. On the other hand, heat treatment techniques like solution annealing improved the damping capacity and inhibited fatigue crack growth rate compared to as built samples made by L-PBF.

8.2. Scope for future research work

Future research can examine the following aspects:

1. Effect of laser re melting on microstructure, mechanical and fatigue behavior of 17-4 PH SS by SLM
2. Correlation between tensile and fatigue behavior of 17-4 PH SS by SLM with the influence of post processing methods.
3. Evaluation of creep behaviour of 17-4 PH SS by SLM with the influence of post processing
4. Evaluation of thermal behaviour and melt pool simulation behavior of 17-4 PH SS by SLM method.

References

[1] M. Khorasani *et al.*, “The effect of absorption ratio on meltpool features in laser-based powder bed fusion of IN718,” *Opt. Laser Technol.*, vol. 153, no. May, p. 108263, 2022, doi: 10.1016/j.optlastec.2022.108263.

[2] J. Schiltz *et al.*, “Fatigue Performance of Direct Metal Laser Sintered Parts using Reused Metallic Feedstocks,” *Procedia Manuf.*, vol. 48, pp. 814–820, 2020, doi: 10.1016/j.promfg.2020.05.118.

[3] N. Nadammal *et al.*, “Journal Pre-proof Critical role of scan strategies on the development of microstructure, texture, and residual stresses during laser powder bed fusion additive manufacturing Critical role of scan strategies on the development of microstructure, texture, and residual stresses during laser powder bed fusion additive manufacturing,” 2020, doi: 10.1016/j.addma.2020.101792.

[4] J. P. Oliveira, A. D. LaLonde, and J. Ma, “Processing parameters in laser powder bed fusion metal additive manufacturing,” *Mater. Des.*, vol. 193, Aug. 2020, doi: 10.1016/j.matdes.2020.108762.

[5] G. Liu *et al.*, “Additive manufacturing of structural materials,” *Mater. Sci. Eng. R Reports*, no. xxxx, p. 100596, 2021, doi: 10.1016/j.mser.2020.100596.

[6] R. Molaei, A. Fatemi, and N. Phan, “Multiaxial fatigue of LB-PBF additive manufactured 17–4 PH stainless steel including the effects of surface roughness and HIP treatment and comparisons with the wrought alloy,” *Int. J. Fatigue*, vol. 137, no. April, p. 105646, 2020, doi: 10.1016/j.ijfatigue.2020.105646.

[7] H. Fayazfar *et al.*, “A critical review of powder-based additive manufacturing of ferrous alloys: Process parameters, microstructure and mechanical properties,” *Mater. Des.*, vol. 144, pp. 98–128, 2018, doi: 10.1016/j.matdes.2018.02.018.

[8] A. B. Spierings, N. Herres, and G. Levy, “Influence of the particle size distribution on surface quality and mechanical properties in AM steel parts,” *Rapid Prototyp. J.*, vol. 17, no. 3, pp. 195–202, 2011, doi: 10.1108/13552541111124770.

[9] A. Bandyopadhyay, Y. Zhang, and S. Bose, “Recent developments in metal additive manufacturing,” *Curr. Opin. Chem. Eng.*, vol. 28, pp. 96–104, 2020, doi: 10.1016/j.coche.2020.03.001.

[10] D. Bourell *et al.*, “Materials for additive manufacturing,” *CIRP Ann. - Manuf. Technol.*, vol.

66, no. 2, pp. 659–681, 2017, doi: 10.1016/j.cirp.2017.05.009.

[11] B. Rankouhi, S. Jahani, F. E. Pfefferkorn, and D. J. Thoma, “Compositional grading of a 316L-Cu multi-material part using machine learning for the determination of selective laser melting process parameters,” *Additive Manufacturing*, vol. 38. 2021. doi: 10.1016/j.addma.2021.101836.

[12] S. Cooke, K. Ahmadi, S. Willerth, and R. Herring, “Metal additive manufacturing: Technology, metallurgy and modelling,” *J. Manuf. Process.*, vol. 57, no. April, pp. 978–1003, 2020, doi: 10.1016/j.jmapro.2020.07.025.

[13] D. D. Gu, W. Meiners, K. Wissenbach, and R. Poprawe, “Laser additive manufacturing of metallic components: Materials, processes and mechanisms,” *Int. Mater. Rev.*, vol. 57, no. 3, pp. 133–164, 2012, doi: 10.1179/1743280411Y.0000000014.

[14] B. Dutta, S. Babu, and B. Jared, *Additive manufacturing technology*. 2019. doi: 10.1016/b978-0-12-816634-5.00002-9.

[15] W. E. Frazier, “Metal additive manufacturing: A review,” *J. Mater. Eng. Perform.*, vol. 23, no. 6, pp. 1917–1928, 2014, doi: 10.1007/s11665-014-0958-z.

[16] K. Moeinfar, F. Khodabakhshi, S. F. Kashani-bozorg, M. Mohammadi, and A. P. Gerlich, “A review on metallurgical aspects of laser additive manufacturing (LAM): Stainless steels, nickel superalloys, and titanium alloys,” *J. Mater. Res. Technol.*, vol. 16, pp. 1029–1068, 2021, doi: 10.1016/j.jmrt.2021.12.039.

[17] A. kumar Kartikeya Sarma, I. N.Selvaraj, “In fl uence of scanning strategies on microstructure , residual stress , and corrosion behavior of 17-4 PH stainless steel fabricated by selective laser melting,” 2022, doi: 10.1177/09544089221106263.

[18] I. Kartikeya Sarma, N. Selvraj, and A. Kumar, “A Review on Microstructure and Mechanical Properties of L-PBF 17-4PH and 15-5PH SS,” *Lect. Notes Mech. Eng.*, pp. 37–53, 2022, doi: 10.1007/978-981-16-7787-8_4.

[19] S. Sarkar, S. Mukherjee, C. S. Kumar, and A. Kumar Nath, “Effects of heat treatment on microstructure, mechanical and corrosion properties of 15-5 PH stainless steel parts built by selective laser melting process,” *J. Manuf. Process.*, vol. 50, no. September 2018, pp. 279–294, 2020, doi: 10.1016/j.jmapro.2019.12.048.

[20] A. Caballero, J. Ding, S. Ganguly, and S. Williams, “Wire + Arc Additive Manufacture of 17-4 PH stainless steel: Effect of different processing conditions on microstructure,

hardness, and tensile strength," *J. Mater. Process. Technol.*, vol. 268, no. June, pp. 54–62, 2019, doi: 10.1016/j.jmatprotec.2019.01.007.

[21] J. H. Robinson, I. R. T. Ashton, E. Jones, P. Fox, and C. Sutcliffe, "The effect of hatch angle rotation on parts manufactured using selective laser melting," *Rapid Prototyp. J.*, vol. 25, no. 2, pp. 289–298, 2019, doi: 10.1108/RPJ-06-2017-0111.

[22] W. Sun, Y. Ma, W. Huang, W. Zhang, and X. Qian, "Effects of build direction on tensile and fatigue performance of selective laser melting Ti6Al4V titanium alloy," *Int. J. Fatigue*, vol. 130, no. June 2019, 2020, doi: 10.1016/j.ijfatigue.2019.105260.

[23] R. Rashid, S. H. Masood, D. Ruan, S. Palanisamy, R. A. Rahman Rashid, and M. Brandt, "Effect of scan strategy on density and metallurgical properties of 17-4PH parts printed by Selective Laser Melting (SLM)," *J. Mater. Process. Technol.*, vol. 249, pp. 502–511, 2017, doi: 10.1016/j.jmatprotec.2017.06.023.

[24] H. R. Lashgari, Y. Xue, C. Onggowarsito, C. Kong, and S. Li, "Microstructure, Tribological Properties and Corrosion Behaviour of Additively Manufactured 17-4PH Stainless Steel: Effects of Scanning Pattern, Build Orientation, and Single vs. Double scan," *Mater. Today Commun.*, vol. 25, no. March, 2020, doi: 10.1016/j.mtcomm.2020.101535.

[25] H. Ali, H. Ghadbeigi, and K. Mumtaz, "Residual stress development in selective laser-melted Ti6Al4V: a parametric thermal modelling approach," *Int. J. Adv. Manuf. Technol.*, vol. 97, no. 5–8, pp. 2621–2633, Jul. 2018, doi: 10.1007/s00170-018-2104-9.

[26] J. Robinson, I. Ashton, P. Fox, E. Jones, and C. Sutcliffe, "Determination of the effect of scan strategy on residual stress in laser powder bed fusion additive manufacturing," *Addit. Manuf.*, vol. 23, no. June, pp. 13–24, 2018, doi: 10.1016/j.addma.2018.07.001.

[27] H. Zhang *et al.*, "Influence of scanning strategy and parameter on microstructural feature, residual stress and performance of Sc and Zr modified Al–Mg alloy produced by selective laser melting," *Mater. Sci. Eng. A*, vol. 788, no. April, p. 139593, 2020, doi: 10.1016/j.msea.2020.139593.

[28] C. Zhao, Y. Bai, Y. Zhang, X. Wang, J. Min, and H. Wang, "Materials & Design Influence of scanning strategy and building direction on microstructure and corrosion behaviour of selective laser melted 316L stainless steel," *Mater. Des.*, vol. 209, p. 109999, 2021, doi: 10.1016/j.matdes.2021.109999.

[29] M. Wu, Z. Zhao, X. Wang, C. Wang, and P. Liang, "Corrosion behavior of 17–4 PH

stainless steel in simulated marine environment," *Mater. Corros.*, vol. 70, no. 3, pp. 461–469, 2019, doi: 10.1002/maco.201810454.

[30] D. Karthik and S. Swaroop, "Electrochemical stability of laser shock peened 17-4 PH stainless steel," *Opt. Laser Technol.*, vol. 120, no. February, p. 105727, 2019, doi: 10.1016/j.optlastec.2019.105727.

[31] P. Ponnusamy, S. H. Masood, S. Palanisamy, R. A. Rahman Rashid, and D. Ruan, "Characterization of 17-4PH alloy processed by selective laser melting," *Mater. Today Proc.*, vol. 4, no. 8, pp. 8498–8506, 2017, doi: 10.1016/j.matpr.2017.07.196.

[32] M. Alnajjar *et al.*, "Influence of microstructure and manganese sulfides on corrosion resistance of selective laser melted 17-4 PH stainless steel in acidic chloride medium," *Corros. Sci.*, vol. 168, no. February, p. 108585, 2020, doi: 10.1016/j.corsci.2020.108585.

[33] A. Zhukov, B. Barakhtin, and P. Kuznetsov, "Study of Strength Characteristics of Steel Specimens after Selective Laser Melting of Powder Materials 17-4PH, 316L, 321," *Phys. Procedia*, vol. 89, pp. 179–186, 2017, doi: 10.1016/j.phpro.2017.08.012.

[34] L. E. Murr *et al.*, "Microstructures and properties of 17-4 PH stainless steel fabricated by selective laser melting," *J. Mater. Res. Technol.*, vol. 1, no. 3, pp. 167–177, 2012, doi: 10.1016/S2238-7854(12)70029-7.

[35] G. Dursun, S. Ibekwe, G. Li, P. Mensah, G. Joshi, and D. Jerro, "Influence of laser processing parameters on the surface characteristics of 316L stainless steel manufactured by selective laser melting," *Mater. Today Proc.*, vol. 26, pp. 387–393, 2019, doi: 10.1016/j.matpr.2019.12.061.

[36] S. Vunnam, A. Saboo, C. Sudbrack, and T. L. Starr, "Effect of powder chemical composition on the as-built microstructure of 17-4 PH stainless steel processed by selective laser melting," *Addit. Manuf.*, vol. 30, no. September, p. 100876, 2019, doi: 10.1016/j.addma.2019.100876.

[37] A. Kudzal *et al.*, "Effect of scan pattern on the microstructure and mechanical properties of Powder Bed Fusion additive manufactured 17-4 stainless steel," *Mater. Des.*, vol. 133, pp. 205–215, 2017, doi: 10.1016/j.matdes.2017.07.047.

[38] C. Y. Liu *et al.*, "Effect of scanning strategy on microstructure and mechanical properties of selective laser melted reduced activation ferritic/martensitic steel," *Mater. Sci. Eng. A*, vol. 766, no. May, 2019, doi: 10.1016/j.msea.2019.138364.

[39] Y. C. Wang, L. M. Lei, L. Shi, H. Y. Wan, F. Liang, and G. P. Zhang, “Scanning strategy dependent tensile properties of selective laser melted GH4169,” *Mater. Sci. Eng. A*, vol. 788, no. March, p. 139616, 2020, doi: 10.1016/j.msea.2020.139616.

[40] T. Bhardwaj and M. Shukla, “Effect of laser scanning strategies on texture, physical and mechanical properties of laser sintered maraging steel,” *Mater. Sci. Eng. A*, vol. 734, no. June, pp. 102–109, 2018, doi: 10.1016/j.msea.2018.07.089.

[41] T. Bhardwaj and M. Shukla, “Effect of scan direction on tensile properties and fractography of laser additive manufactured maraging steel,” *Mater. Today Proc.*, vol. 18, pp. 3842–3848, 2019, doi: 10.1016/j.matpr.2019.07.323.

[42] P. Bian, J. Shi, Y. Liu, and Y. Xie, “Influence of laser power and scanning strategy on residual stress distribution in additively manufactured 316L steel,” *Opt. Laser Technol.*, vol. 132, no. August 2019, p. 106477, 2020, doi: 10.1016/j.optlastec.2020.106477.

[43] M. L. Montero-Sistiaga, M. Godino-Martinez, K. Boschmans, J. P. Kruth, J. Van Humbeeck, and K. Vanmeensel, “Microstructure evolution of 316L produced by HP-SLM (high power selective laser melting),” *Addit. Manuf.*, vol. 23, no. May, pp. 402–410, 2018, doi: 10.1016/j.addma.2018.08.028.

[44] Y. Song, Q. Sun, K. Guo, X. Wang, J. Liu, and J. Sun, “Effect of scanning strategies on the microstructure and mechanical behavior of 316L stainless steel fabricated by selective laser melting,” *Mater. Sci. Eng. A*, vol. 793, no. April, p. 139879, 2020, doi: 10.1016/j.msea.2020.139879.

[45] Y. Sun, R. J. Hebert, and M. Aindow, “Effect of heat treatments on microstructural evolution of additively manufactured and wrought 17-4PH stainless steel,” *Mater. Des.*, vol. 156, pp. 429–440, 2018, doi: 10.1016/j.matdes.2018.07.015.

[46] Z. Xiao, Y. Lei, Z. Hu, C. Chen, B. Chen, and H. Zhu, “Influence of rescanning parameters on selective laser melting of Ti6Al4V,” *J. Manuf. Process.*, vol. 82, pp. 530–542, Oct. 2022, doi: 10.1016/J.JMAPRO.2022.08.034.

[47] A. Yadollahi, M. Mahmoudi, A. Elwany, H. Doude, L. Bian, and J. C. Newman, “Effects of crack orientation and heat treatment on fatigue-crack-growth behavior of AM 17-4 PH stainless steel,” *Eng. Fract. Mech.*, vol. 226, no. January, p. 106874, 2020, doi: 10.1016/j.engfracmech.2020.106874.

[48] A. Yadollahi, N. Shamsaei, S. M. Thompson, A. Elwany, and L. Bian, “Effects of building

orientation and heat treatment on fatigue behavior of selective laser melted 17-4 PH stainless steel," *Int. J. Fatigue*, vol. 94, pp. 218–235, 2017, doi: 10.1016/j.ijfatigue.2016.03.014.

[49] L. Carneiro, B. Jalalahmadi, A. Ashtekar, and Y. Jiang, "Cyclic deformation and fatigue behavior of additively manufactured 17–4 PH stainless steel," *Int. J. Fatigue*, vol. 123, no. February, pp. 22–30, 2019, doi: 10.1016/j.ijfatigue.2019.02.006.

[50] S. Cheruvathur, E. A. Lass, and C. E. Campbell, "Additive Manufacturing of 17-4 PH Stainless Steel: Post-processing Heat Treatment to Achieve Uniform Reproducible Microstructure," *Jom*, vol. 68, no. 3, pp. 930–942, 2016, doi: 10.1007/s11837-015-1754-4.

[51] M. De Wild, F. Meier, T. Bormann, C. B. C. Howald, and B. Müller, "Damping of selective-laser-melted NiTi for medical implants," *J. Mater. Eng. Perform.*, vol. 23, no. 7, pp. 2614–2619, 2014, doi: 10.1007/s11665-014-0889-8.

[52] F. Rosa, S. Manzoni, and R. Casati, "Damping behavior of 316L lattice structures produced by Selective Laser Melting," *Mater. Des.*, vol. 160, pp. 1010–1018, 2018, doi: 10.1016/j.matdes.2018.10.035.

[53] L. Parry, I. A. Ashcroft, and R. D. Wildman, "Understanding the effect of laser scan strategy on residual stress in selective laser melting through thermo-mechanical simulation," *Addit. Manuf.*, vol. 12, pp. 1–15, 2016, doi: 10.1016/j.addma.2016.05.014.

[54] A. A. Adeyemi, E. Akinlabi, R. M. Mahamood, K. O. Sanusi, S. Pityana, and M. Tlotleng, "Influence of laser power on microstructure of laser metal deposited 17-4 ph stainless steel," *IOP Conf. Ser. Mater. Sci. Eng.*, vol. 225, p. 012028, 2017, doi: 10.1088/1757-899x/225/1/012028.

[55] T. DebRoy *et al.*, "Additive manufacturing of metallic components – Process, structure and properties," *Prog. Mater. Sci.*, vol. 92, 2018, doi: 10.1016/j.pmatsci.2017.10.001.

[56] Q. Chao, S. Thomas, N. Birbilis, P. Cizek, P. D. Hodgson, and D. Fabijanic, "The effect of post-processing heat treatment on the microstructure, residual stress and mechanical properties of selective laser melted 316L stainless steel," *Mater. Sci. Eng. A*, vol. 821, no. June, p. 141611, 2021, doi: 10.1016/j.msea.2021.141611.

[57] V. Cruz, Q. Chao, N. Birbilis, D. Fabijanic, P. D. Hodgson, and S. Thomas, "Electrochemical studies on the effect of residual stress on the corrosion of 316L manufactured by selective laser melting," *Corrosion Science*, vol. 164. 2020. doi:

10.1016/j.corsci.2019.108314.

[58] T. Simson, A. Emmel, A. Dwars, and J. Böhm, “Residual stress measurements on AISI 316L samples manufactured by selective laser melting,” *Additive Manufacturing*, vol. 17. pp. 183–189, 2017. doi: 10.1016/j.addma.2017.07.007.

[59] P. Bian, J. Shi, Y. Liu, and Y. Xie, “Influence of laser power and scanning strategy on residual stress distribution in additively manufactured 316L steel,” *Opt. Laser Technol.*, vol. 132, p. 106477, Dec. 2020, doi: 10.1016/j.optlastec.2020.106477.

[60] J. P. Kruth, M. Badrossamay, E. Yasa, J. Deckers, L. Thijs, and J. Van Humbeeck, “Part and material properties in selective laser melting of metals,” *16th Int. Symp. Electromachining, ISEM 2010*, pp. 3–14, 2010.

[61] Y. Sun, A. Moroz, and K. Alrbaey, “Sliding wear characteristics and corrosion behaviour of selective laser melted 316L stainless steel,” *J. Mater. Eng. Perform.*, vol. 23, no. 2, pp. 518–526, 2014, doi: 10.1007/s11665-013-0784-8.

[62] K. Qi, R. Li, G. Wang, G. Li, B. Liu, and M. Wu, “Microstructure and Corrosion Properties of Laser-Welded SAF 2507 Super Duplex Stainless Steel Joints,” *Journal of Materials Engineering and Performance*, vol. 28, no. 1. pp. 287–295, 2019. doi: 10.1007/s11665-018-3833-5.

[63] H. Ali, H. Ghadbeigi, and K. Mumtaz, “Effect of scanning strategies on residual stress and mechanical properties of Selective Laser Melted Ti6Al4V,” *Materials Science and Engineering A*, vol. 712. pp. 175–187, 2018. doi: 10.1016/j.msea.2017.11.103.

[64] C. Chen, J. Yin, H. Zhu, Z. Xiao, L. Zhang, and X. Zeng, “Effect of overlap rate and pattern on residual stress in selective laser melting,” *International Journal of Machine Tools and Manufacture*, vol. 145. 2019. doi: 10.1016/j.ijmachtools.2019.103433.

[65] J. Fiocchi, C. A. Biffi, D. Scaccabarozzi, B. Saggin, and A. Tuissi, “Enhancement of the Damping Behavior of Ti6Al4V Alloy through the Use of Trabecular Structure Produced by Selective Laser Melting,” *Adv. Eng. Mater.*, vol. 22, no. 2, pp. 1–6, 2020, doi: 10.1002/adem.201900722.